Mechanical Properties of Collagen-Based Scaffolds for Tissue Regeneration

by

Biraja P. Kanungo

S.M., Materials Science and Engineering
The Ohio State University, 2004

B.Tech., Metallurgical and Materials Engineering
Indian Institute of Technology-Madras, 2002

SUBMITTED TO THE DEPARTMENT OF MATERIALS SCIENCE AND ENGINEERING IN PARTIAL FULFILLMENT OF THE REQUIREMENTS FOR THE DEGREE OF

DOCTOR OF PHILOSOPHY IN MATERIALS SCIENCE AND ENGINEERING

AT THE

MASSACHUSETTS INSTITUTE OF TECHNOLOGY

JUNE 2009

Signature of Author.. .....
Biraja P. Kanungo
Department of Materials Science and Engineering
May 12, 2009

Certified by.....
Prof. Lorna J. Gibson
Matoula S. Salapatas Professor of Materials Science and Engineering
Thesis Supervisor

Accepted by.....
Prof. Christine Ortiz
Chairman, Department Committee on Graduate Students
Department of Materials Science and Engineering

Mechanical Properties of Collagen-Based Scaffolds for Tissue Regeneration

by

Biraja P. Kanungo

Submitted to the Department of Materials Science and Engineering
on May 20, 2009 in Partial Fulfillment of the
Requirements for the Degree of Doctor of Philosophy in
Materials Science and Engineering

ABSTRACT

Collagen-glycosaminoglycan (CG) scaffolds for the regeneration of skin and nerve have previously been fabricated by freeze-drying a slurry containing a co-precipitate of collagen and glycosaminoglycan. Recently, mineralized collagen-glycosaminoglycan (MCG) scaffolds for bone regeneration have been developed by freeze-drying a slurry containing a co-precipitate of calcium phosphate, collagen and glycosaminoglycan. Bi-layer scaffolds with CG and MCG layers have been developed for cartilage-bone joint regeneration. The mechanical properties (Young's modulus and strength) of scaffolds are critical for handling during surgery as well as for cell differentiation. The mechanical properties of the MCG scaffolds are low in the dry state (e.g. they can be crushed under hard thumb pressure) as well as in the hydrated state (e.g. they do not have the optimal modulus for mesenchymal stem cells (MSC) to differentiate into bone cells). In addition, there is interest in extending the application of CG scaffolds to tendon and ligament, which carry significant mechanical loads. This thesis aims to improve the mechanical properties of the both CG and MCG scaffolds and to characterize their microstructure and mechanical properties.

Models for cellular solids suggest that the overall mechanical properties of the scaffold can be increased by either increasing the mechanical properties of the solid from which the scaffold is made or by increasing the relative density of the scaffold. In an attempt to increase the solid properties, the MCG scaffolds with increasing mineral content were fabricated. The mechanical properties were lower for the more highly mineralized scaffolds as a result of an increase in the number of defects such as cracked and disconnected walls. Next, we attempted to increase the mechanical properties by increasing the relative density of the MCG scaffolds. The volume fraction of solids in the slurry was increased by a vacuum-filtration technique. The slurry was then freeze-dried in the conventional manner to produce scaffolds with increased relative densities. Increasing the relative density by a factor of 3 increased the dry Young's modulus and crushing strength roughly by 9 and 7 times, respectively, allowing the dry scaffolds to withstand hard thumb pressure. The Young's modulus for the densest scaffold in the hydrated state was in the optimum range for MSC to differentiate into bone cells. Further, we attempted to improve the mechanical properties of the CG scaffold using the same technique. We were able to achieve an increase in its tensile Young's modulus in the dry state by a factor of about10 times. Finally, the fraction of MC3T3 cells attaching to the CG scaffolds was found to increase linearly with the specific surface area of the scaffold, or with the number of binding sites available for cell attachment.

Thesis Supervisor: Lorna J. Gibson
Title: Matoula S. Salapatas Professor of Materials Science and Engineering

Acknowledgments

First and foremost I would like to thank my family and friends for their motivation and continued collective mentorship in pursuing my career goals and personal development. I have truly enjoyed my time at MIT and this has been possible due to all those who I have shared the experience with. I would like to thank the faculty and staff of the Department of Materials Science and Engineering, Department of Biological Engineering, and the Sloan School of Management at MIT for providing extraordinary educational opportunities in the classroom as well as in the laboratory. Specifically, I am grateful for the opportunity to work under the supervision of Prof. Lorna J. Gibson. Her creativity, vision, and dedication to science and engineering have been truly inspirational. Furthermore, her active involvement in the project on a regular basis has made it possible to finish this research. I also want to thank the members of my thesis committee, Prof. Myron Spector and Prof. Samuel Allen, who have bestowed upon me encouragement, inspiration, and technical wisdom. Prof. Brendan Harley and Dr. Andrew Lynn have provided me with valuable advice, encouragement, insight, and intellectual perspective throughout the various stages of my Ph.D. work, and career development in general. This work would not have been possible without the contribution of many collaborators. In particular, I want to thank Prof. Ioannis Yannas for using his scaffold fabrication laboratory. I also want to thank Prof. Krystyn Van Vliet and Dr. Emilio Silva for their help in the atomic force microscopy, Prof. Simona Socrate and Dr. Kristin myers for their help in mechanical characterization, Prof. Elazer Edelman and Mr. Philip Seifert for their help in histology, Prof. David Cory and Dr. Chandrasekhar Ramanathan for their help in micro-computer-tomography, Mr. Alan Schwartzman for his help in nanoindentation, and finally Ms. Karolina Corin for her help in cell attachment study on the scaffolds. I also want to recognize the roles of Dr. Kishore Mosaliganti, who helped me automat the pore size analysis for the scaffolds and Mr. Kaustuv DeBiswas for his help in laser cutting the scaffold samples. Finally I want to acknowledge National Science Foundation (grant No. CMS-0408259) for financially supporting this research.

Table of Contents

List of Figures

List of Tables

CHAPTER 1. Introduction and Background: Collagen-Based Scaffolds

1.1 Tissue engineering and regenerative medicine

Every year, millions of patients suffer tissue loss or end-stage organ failure as a result of accidents or disease (Table 1.1). Over 8 million surgical procedures are performed to treat these patients in the U.S. each year, and the overall health care cost for these patients exceeds $400 billion per year [1-3]. Treatment options for organ injury depend on the scale of the defect. Microscopic defects can be treated using a wide variety of soluble factors (i.e., pharmaceuticals, vitamins, hormones, and antibiotics). Organ-scale defects, presenting significantly larger sites, and requiring considerably different treatment practices, are the focus of this thesis. Five approaches have been used to treat organ or tissue loss: (1) autografting (the donor and the recipient are the same individual; a fraction of the tissue or organ is harvested from an uninjured site and grafted at the nonfunctional site), (2) allografting (transplantation between different individuals of the same species), (3) xenografting (transplantation between individuals of different species), (4) implantation of a permanent prosthetic device (devices are typically fabricated from biologically inert materials such as metals, ceramics, and synthetic materials that do not provoke immune response problems), and (5) tissue engineering. Table 1.2 lists the

advantages and disadvantages of all the above approaches. Tissue engineering uses three general strategies for the creation of new tissues: (1) stem cells, (2) *in-vitro* synthesis of organs, and (3) induced *in-vivo* organ regeneration [1, 4]. Porous, three-dimensional scaffolds have been used extensively as biomaterials in the field of tissue engineering for *in-vitro* study of cell-scaffold interactions and tissue synthesis and *in-vivo* study of induced tissue and organ regeneration [4, 5].

Organ	Patients per year
Skin	4, 750, 000
Bone	1, 340, 000
Cartilage	1, 150, 000
Tendon and Ligament repair	123, 000
Blood vessels	1, 360, 000
Pancreas	728, 000
Urological	82, 000
Dental	10, 000, 000

Table 1.1. Number of cases of end stage organ or tissue failure in United States of America per year [1].

In addition to the above approaches; cell sheet engineering is a new technique for culturing cells as intact sheets *in-vitro* without the use of bio-degradable scaffolds [6]. Using temperature-responsive culture dishes, cells can be harvested as intact sheets by simple temperature changes, thereby avoiding the use of proteolytic enzymes. Cell sheet engineering allows for tissue regeneration by either direct transplantation of cell sheets to host tissues or the creation of three-dimensional structures via the layering of individual

cell sheets. By avoiding the use of any additional materials such as carrier substrate or scaffolds, the complications associated with traditional tissue engineering approaches such as host inflammatory responses to implanted polymer materials, can be avoided. However, this method is in the initial phase and extensive research needs to be done before it becomes viable.

Induced *in-vivo* organ regeneration is potentially the most advantageous approach with the fewest limitations. It is the only method to modify the mammalian wound healing response to induce regeneration (unlike the usual repair process). The host inflammatory response in *in-vivo* organ generation can be overcome by using natural polymers such as collagen, which is the focus of this thesis. Although the therapeutic promise for regenerative medicine is immensely exciting, the cost of product development, and particularly of clinical trials, for the more demanding applications will be high. However, it has been shown (by comparing the cost per quality-adjusted life year, QALY, the product of life expectancy and a measure of the quality of the remaining life years) that the regenerative industry can yield an appropriate return on investment [3].

Approach	Advantages	Disadvantages
Autografting	o No Immunorejection o No diseases transmission o Better bonding of the graft to the host tissue and long-term graft stability [7]	o Donor site morbidity o Shortage of donor sites (especially for large wounds) o Tendency towards resorption [8]
Allografting	o Avoids donor site morbidity in case of grafts taken from cadavers o Economic compared to autografts [9]	o Donor shortage o Delayed remodeling of the host tissue o Immunorejection leading to lifetime use of

	○ No size limitation on the grafts [10]	immunosuppressants ○ Concern of viral contamination [8] ○ Ethical and religious concerns
Xenografting	○ Adequate supply ○ Resist infection by human viruses or recurrence of the diseases that caused organ failure [11-13] ○ Genetic manipulation of the animal to customize the transplantation [13]	○ Immunorejection leading to lifetime use of immunosuppressants ○ Concern of viral contamination ○ Inefficient performance compared to human tissues or organs
Permanent prosthetic devices	○ No Immunorejection ○ Prevents sudden failure and death [14] ○ Acts as a bridge to transplantation [15] ○ Adequate mechanical stability for specific uses	○ Lower quality performance. For example: lack the ability to self-repair and modify the structure and properties based on the environment [8] ○ Unfavorable interaction between the implant and the surrounding biological environment. For example: formation of thick, fibrous, scar tissue capsule around the implants, accumulating wear particles, and stress-shield of surrounding tissue [4] ○ Host tissue resorption ○ Revision surgery [8]
Stem cells	○ Pluripotent behavior of stem cells to differentiate into various phenotypes ○ Through cloning, the genetic capability of the donor's nucleus is combined with functional properties of the recipient cytoplasm [16]	○ Difficulty in getting the cells to mature and contribute physiological functions [17] ○ Immunorejection, especially in use of embryonic stem cells [17] ○ Not fully understood at this point and further research is needed ○ Ethical and religious concerns [4]
In-vitro synthesis	○ Total control over the culture environment such as soluble regulator content *(i.e.,* growth factors, cytokines), insoluble regulator content *(i.e.,* ECM proteins), and a variety of cell culture medium and loading conditions [4]	○ Construct size limit (< 1 cm) due to diffusion constraints as there is no angiogenesis [17] ○ Complexity of biological systems, specifically cytokine, growth factor, and inter-cellular signaling needs throughout the volume of the developing tissue have precluded the formation of complex tissue in-vivo [4]

In-vivo synthesis	o Angiogenesis possible that relaxes the limit on construct size [17] o Availability of nutrients from the surrounding tissue	o Host inflammatory responses, especially in synthetic polymeric scaffolds [6] o Difficult to regenerate complex organs as a whole

Table 1.2. Limitations of current treatment methods to repair the organ or tissue failure.

1.2 Design parameters for scaffolds in tissue engineering

Scaffolds for tissue regeneration are three dimensional porous matrixes which mimic body's own extracellular matrix, onto which cells attach, multiply, migrate, and begin synthesizing new tissue [18]. Scaffolds can also potentially serve several additional functions, such as (1) structurally reinforcing the defect, (2) preventing ingress of surrounding tissue, and (3) acting as a delivery vehicle for cells, growth factors, or genes [19]. Although unproven, a widely believed design paradigm for scaffolds is that the scaffold should mimic the composition of the natural extracellular matrix as closely as possible in order to have better regenerating capability [20]. Biologically active scaffolds used for tissue regeneration must meet a number of biophysical and biochemical constraints. The required parameters can be explained in terms of the properties of the polymer of which the scaffold is made (i.e. biocompatibility, biodegradability, cell-polymer interaction, and release of bioactive molecules) and the properties of the overall scaffold (i.e. pore size, porosity or pore volume fraction, and mechanical properties of the scaffold).

Biocompatibility

One critical parameter for polymers for tissue engineering applications is biocompatibility. Biocompatibility relates to a material's ability to exist within the body with no inflammatory response and no toxicity to cells. The products of degradation must also be biocompatible. Naturally derived polymers often demonstrate adequate biocompatibility, while synthetic polymers may elicit significant negative responses from the body [21]. Adhesive interactions of cells with polymers may significantly affect the proliferation, migration, and differentiation of cells to be engineered. The adhesion of cells to polymer scaffolds may be cell-type specific, depending on the interaction of specific cell receptors that recognize adhesion molecules (i.e. ligands) at the surface of the material. The ligand molecules can either be inherent components of the materials (in case of natural polymers) or be artificially introduced into the materials (in case of synthetic polymers).

Biodegradability

Controlled degradation of the polymer scaffold is critical to tissue engineering. The degradation rate of the polymer has to be almost equal to the regeneration rate of the extracellular matrix by the cells. The degradation rate must allow the scaffold to remain insoluble for the duration of the critical cellular processes, a time period particular to each biological system [5, 22, 23]. Some synthetic polymers are non-degradable while others have cytotoxic degradation byproducts, limiting their use *in-vivo*.

Pore microstructure

The pore size of the scaffold must be large enough to allow cell migration into the scaffold. However, the pores have to be small enough that the specific surface area

provides a sufficiently large number of binding sites for cell attachment. And to allow for transport of cells and metabolites, the scaffold must have a large pore volume fraction (generally greater than 90%) as well as an interconnected pore network [24].

Mechanical properties

Controlling the mechanical properties of the scaffold is also an important design parameter, as the adhesion and gene expression of interacting cells may be related to the mechanical properties of the scaffold [21, 25]. Recently, Engler *et al.*. [26] showed that human mesenchymal stem cells (MSC) differentiate into specific lineages and commit to phenotypes (neurogenic, myogenic, and osteogenic) depending on the substrate elasticity. They used an inert polyacralymide gel with varying concentrations of bis-acrylamide crosslinker that controls the matrix stiffness to mimic various tissue microenvironments. Cell adhesion was provided by coating the gel with type I collagen that is known to support myogenic and osteogenic differentiation. On soft collagen coated gel that mimics brain elasticity ($E_{brain} \sim 0.1 - 1$ kPa) [27], MSCs cultured for several weeks differentiated into neurogenic cells. MSCs on 10-fold stiffer matrices that mimic muscle elasticity ($E_{muscle} \sim 8 - 17$ kPa) [28] lead to myoblast-like cells. Stiffer matrices (25 – 40 kPa) that mimic the crosslinked collagen of osteoids [29] yielded osteoblast-like cells. The mechanical properties of the scaffold depend on the inherent physical characteristics of the solid polymer (which, in turn, depend on the type and density of cross-links), as well as on the relative density of the scaffold (the density of the cellular solid, divided by that of the solid from which it is made).

Release of bioactive molecules and ease of processing

Release of bioactive molecules (e.g. growth factors) is another critical element in engineering large tissues as it helps in development of new vascular network structures, which enable the delivery of sufficient oxygen and other nutrients to the engineered tissues. Also the scaffold material should be such that it is easily processed into three-dimensional shapes of irregular geometry.

1.3 Biomaterials for scaffolds in tissue engineering

Natural polymers

Figure 1.1 is a schematic showing the different categories of biomaterials used to fabricate scaffolds for tissue engineering [30, 31]. Natural-organic polymers are isolated directly from the natural extracellular-matrix (ECM) and therefore contain a host of surface ligands appropriate for the formation of cell-scaffold complexes. Additionally, the degradation rate of natural-organic polymers can be controlled through the degree and type of crosslinking techniques and the degradation products are non-toxic. However, they typically do not exhibit the required mechanical properties for regenerating hard tissues like bone. Among all the natural-organic polymers collagen is the most versatile substrate for supporting cell proliferation and differentiation. Type I collagen is the predominant form found in the ECM of various tissues. Its low antigenicity and immunogenicity make it attractive for scaffolds [31]. Collagen has been approved by the United States Food and Drug Administration (FDA) for many types of medical applications including wound dressing and artificial skin. Glycosaminoglycans (GAG) are a significant part of proteoglycans (another class of organic polymers found in the ECM) and have been used extensively for tissue engineering scaffolds. Copolymers of

collagen and GAG (CG) have been used to regenerate skin, conjunctiva, and peripheral nerves [31]. Copolymerization of collagen and GAG has been observed to increase the stiffness and toughness and decrease the degradation rate of collagen. CG scaffolds are primarily manufactured using a freeze-drying process from a suspension consisting of co-precipitated collagen and GAG from acetic acid solution. The details of this method will be described later in this text. Alginate, a polysaccharide isolated from seaweed, is biocompatible and has been approved by the FDA for human use as a wound-dressing material. It has also been used as an injectable cell-delivery vehicle [32].

Synthetic polymers

Figure 1.1 lists the major synthetic polymers used in tissue engineering [20, 30, 31]. Due to the fact that they are chemically synthesized, it is possible to control (with varying degrees of accuracy depending on, among other factors, the type of polymerization reaction) their stiffness and degradation rate. Another benefit to using synthetic polymers is that a range of processing techniques, some involving high temperature and pressure (which is not possible in case of natural polymers), can be used to produce scaffolds with complex microstructure. Cells do not necessarily recognize synthetic polymer surfaces. Integrin or receptor binding, critical for the necessary cell-ECM communication, is lacking in synthetic polymeric scaffolds [33]. Another area of concern is scaffold degradation; some synthetic polymers are non-degradable while others have cytotoxic degradation products.

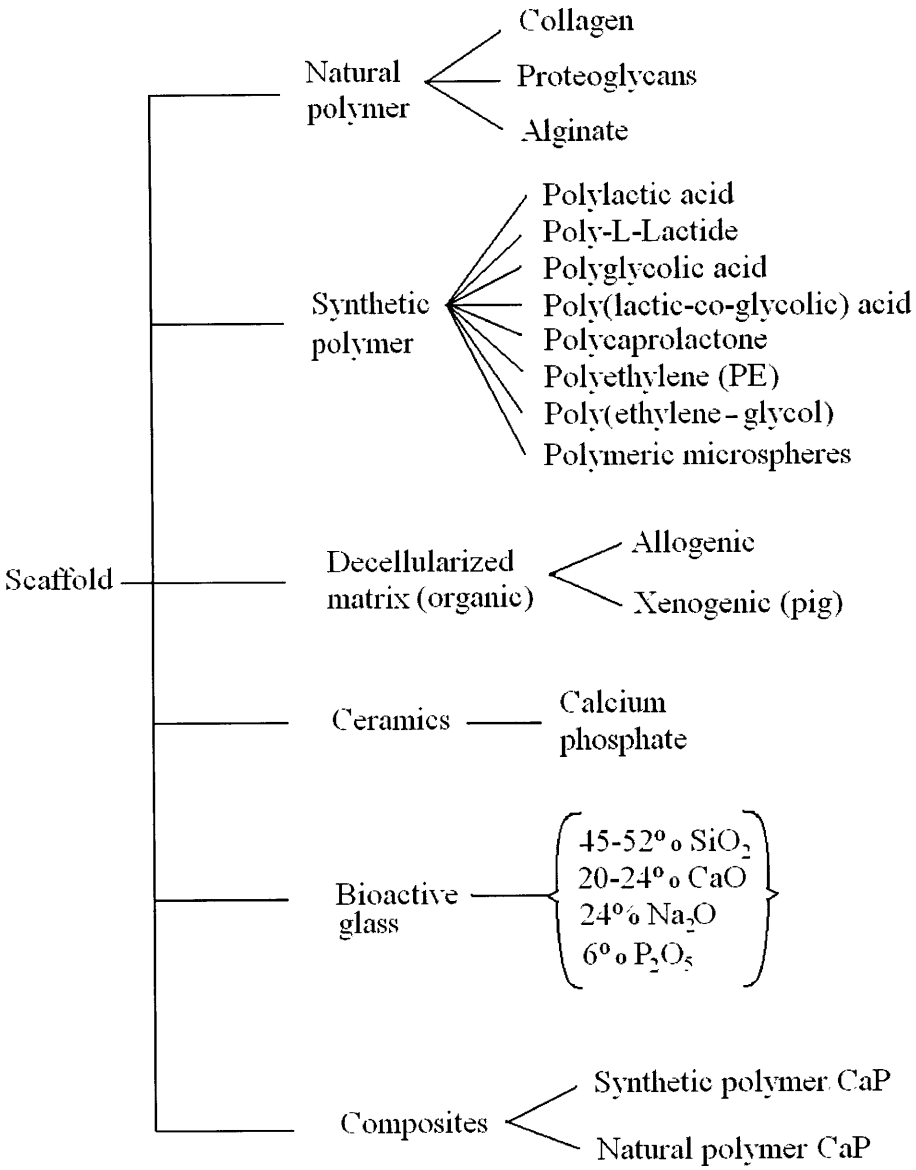

Figure 1.1. Various biomaterials used as tissue engineering scaffolds [30, 31].

Porosity can be introduced into synthetic polymeric scaffolds using a variety of techniques such as particulate-leaching, emulsion freeze-drying, phase separation, 3-D printing and gas foaming. Particulate-leaching involves dispersing water soluble particles, such as salt, sugar, or polymer spheres in a matrix consisting of the scaffold material and an organic solvent. The solvent is evaporated and a composite of scaffold

material and the water soluble particles remains. The composite is immersed in water in order to dissolve the water soluble particles resulting in a porous scaffold. Emulsion-freeze drying involves creating an emulsion by homogenizing a polymer solvent solution and water. The mixture is quenched in liquid nitrogen and later freeze-dried to obtain the porous scaffold. Phase separation involves thermodynamic demixing (either by cooling the mixture below a bi-modal solubility curve or exposing it to another immiscible solvent) of a homogeneous polymer/solvent mixture into polymer rich and solvent rich phases. 3-D printing is a solid free form technique, in which the sliced two dimensional profile of a computer model is printed on a fresh layer of powder via deposition of a suitable binder. Successive 2D profiles are then printed on freshly laid layers of powder until the whole model is completed. The printed binder joins the respective profiles of each layer together. The part is completed upon removal of the unbound powder and suitable post-processing (e.g. by sintering). 3D printing in combination with salt leaching has been used in the past for fabricating scaffolds for tissue engineering [34, 35] that involves directing a solvent onto polymer packed with salt particles to build a complex 3-D structure from a series of thin 2-D slices. The salt particles are dissolved by immersing the composite structure in water. Scaffolds with macro-pores (via 3D printing) on the order of 800 μm and micro-pores (via salt leaching) on the order of 45-150 μm were fabricated. The structure is computer controlled to obtain custom designs. Gas foaming involves exposing the polymer to high pressure carbon dioxide (~800 psi) for around 48 hours to saturate the polymer with gas [20]. When the pressure is slowly reduced to atmospheric pressure, carbon dioxide nucleates within the polymer, forming pores.

Polymeric microspheres are used in order to deliver growth factors (which stimulate and increase the production of connective tissue, promote remodeling and help supply blood vessels to nourish the site to be regenerated) to the regenerating site. Growth factors can be encapsulated in microspheres which are then subsequently introduced into the scaffolds. Growth factor delivery is regulated by the degradation of the polymer of which the microspheres are made: e.g. synthetic polymers such as PLA/PGA copolymer, or natural polymers (e.g. gelatin). Microspheres are made by techniques such as water/oil/water emulsion, oil/water emulsion, and spray-drying [20].

Decellularized matrices

Decellularized matrices are derived by decellularizing the native tissue by enzymatic or detergent methods instead of fabricating a three dimensional scaffold from synthetic or natural polymers. Decellularized matrices are either allogenic or xenogenic. Examples of decellularized allogenic matrices include the small intestinal submucosa (SIS) construct and naturally derived collagen matrix (NDCM) [31]. Xenogenic (pig) decellularized matrices are mostly used in case of heart valves. However the challenge is to decellularize without disrupting the complex structure of extracellular matrix. Therefore these matrices will not work for all applications, especially not for more complex systems such as liver or the heart [36].

Bioceramics

Bioceramics are widely used as inorganic biomaterials in bone tissue engineering, with tricalcium phosphate (TCP) ($Ca_3(PO_4)_2$), octacalcium phosphate (OCP) ($Ca_8(HPO_4)_2(PO_4)_4.5H_2O$) and hydroxyapatite (HAP) ($Ca_{10}(PO_4)_6(OH)_2$), and their

combinations, being the most frequently used. Hydroxyapatite is the major constituent of bone, constituting ~ 75% by dry weight and responsible for much of its mechanical stiffness and strength. CaP-based scaffolds are biocompatible and have the unique capacity to bond directly to bone. They are osteoconductive and bioactive despite their low degradation rate. However, their usage by themselves is limited because of their brittle nature and the difficulty in processing them into highly porous structures with controlled porosity. The simplest way to generate porous scaffolds from ceramics such as HAP is to sinter particles, preferably spheres of equal size [37]. Briefly, ceramic particles in a wetting solution such as poly (vinyl alcohol) are compacted through cold isostatic pressing followed by sintering. A more advanced way of making ceramic scaffolds with higher porosities is by adding porogens such as polymer foams and polymer gels followed by sintering. During sintering the porogen is burnt out leaving a highly porous ceramic scaffold [37]. Another process for making porous ceramic scaffolds is gel-casting where the polymer foam is formed in situ by a catalyst. The polymer is burnt out during sintering of the ceramic-polymer construct [37].

Bioactive glasses

Bioactive glasses composed of 45 to 52% SiO_2, 20 to 24% CaO, 20 to 24% Na_2O, and 6% P_2O_5 have been successfully used to regenerate both bone as well as soft connective tissues [30]. However, like CaP-based biomaterials, these bioactive glasses are relatively stiff and brittle and difficult to form into complex shapes, particularly as porous scaffolds, making their application limited in vivo [31]. The basic way to make porous bioactive glasses is by sol-gel foaming. Briefly, hydrolysis of alcoxide precursors, such as tetraethyle orthosilicate, forms a colloidal solution (sol). Polycondensation of –Si–OH

groups continues after hydrolysis is complete, beginning the formation of the silicate (–Si– O–Si–) network. As the network connectivity increases, viscosity increases and eventually a gel forms. The gel is then subjected to controlled thermal treatment of ageing to strengthen the gel followed by sintering to eliminate the organic species [37]. Rapid prototyping techniques, such as 3D printing, stereo lithography, laser sintering, are also used to fabricate bioactive glass scaffolds.

Composites of polymers and ceramics

Composite scaffolds with synthetic or natural polymers and calcium phosphate have been developed for high strength applications, mainly for bone. Most of the fabrication techniques for synthetic polymer based composite scaffolds use particulate-leaching in combination with other techniques. Laurencin and his co-workers have developed composite PLGA/HA scaffolds via a combination of emulsion freeze drying and salt-leaching techniques [38]. Solvent casting followed by salt-leaching is a common technique wherein the polymer/ceramic/porogen/slovent mixer is cast into a mold and the solvent is evaporated at room temperature followed by dissolving the composite in a suitable solvent to remove the porogen [39-41]. Pal *et al.* have used hot isostatic pressing along with salt leaching to fabricate high strength composite scaffolds [42]. Jung *et al.* have used a sintering technique along with salt leaching in order to overcome the problem of residual solvent in the scaffold [43]. Gas foaming followed by salt leaching is another technique to fabricate composite scaffolds. Freeze drying is also used to produce composite scaffolds wherein the polymer/ceramic/solvent mixture is frozen to obtain interconnected ice crystals of the required size and shape. Sublimation of the frozen slurry leaves behind the foam-like network of struts with interconnected pores [44, 45].

3-D printing followed by freeze drying is also used to make composite scaffolds [46, 47]. In brief, the polymer/ceramic/solvent is 3-D printed onto a liquid nitrogen cooled base plate followed by sublimating the frozen composite template. This technique produces a bimodal pore distribution with macro- and micro pores (macro-pores resulting from the 3-D printing template and micro-pores resulting from the freeze drying of the struts of the 3-D template).

Composite scaffolds of collagen with a calcium phosphate mineral (eg HA and TCP) have also been developed to regenerate bone. Freeze drying is widely used to make collagen based composite scaffolds. Collagen/ceramic composite scaffolds have been developed by mechanical mixing of the collagen fibers and ceramic powders in a solvent followed by freeze drying [48, 49]. Rucker *et al.* have developed collagen/HA/chitosan scaffolds via 3-D printing wherein the composite slurry (formed by mechanical mixing) is 3-D printed onto a liquid nitrogen cooled base plate followed by solvent removal using ethanol [50]. Gelatin/chitosan/ceramic (HA or TCP) scaffolds have been developed by freeze drying the slurry [51, 52]. Most of these processes include mechanical mixing of the desired amount of the ceramic particles with the natural polymer. The major problem with these methods is that the mineral phase does not form *in situ* and simply adheres to the outside of the collagen or gelatin fibers forming agglomerates [53]. A more advanced method is the biomimetic approach, the precipitation of mineral phase within the polymer solution (which is known as direct mineralization) [49, 54-57]. Using this method, the collagen-HA composites have been synthesized to maintain the nanoscale HA precipitates along the collagen fiber. In brief, precursors of calcium and phosphorous (eg.

$Ca(OH)_2$ and H_3PO_4 for Ca and P respectively) are added to the collagen solution where the mineral phase directly precipitates on the collagen fibers. Researchers have also added osteonectin to the collagen-HA composite (accounts for ~ 20-25% of non-collagenous proteins in demineralized bone) in order to facilitate the formation of a hierarchal matrix with c-axis of the nano-HA oriented parallel to the longitudinal axis of the collagen fibril [58]. The mineralized collagen solution is freeze dried to obtain the porous scaffold. Inspired by the collagen-HA composites, Chang *et al.* and Kim *et al.* have synthesized gelatin-HA composites by the direct mineralization method [53, 59]. Composite scaffolds of collagen/HA/PLA have been developed by direct mineralization processes [60]. However, most of these processes use a titrant to control the *pH* of the solution (in order to control the mineral phase precipitated). Therefore, they have the inherent problem of residual contaminant titrant phase. In these processes the *pH* of the solution is usually maintained in the range of 7-10. However, collagen fibers only become highly swollen and disaggregated and lose their banding (keeping the triple helical structure intact) below a *pH* of 4.25±0.30 [5]. For direct mineralization, it is desirable to precipitate calcium phosphate particles within and between the collagen fibrils in order to mimic the nanoscale structure of bone. This is achieved when the collagen fibrils are disaggregated without losing their triple helical structure. Therefore, the above processes do not mimic the nanoscale structure of bone even though they increase the mechanical properties (Young's modulus and strength) of the scaffold by many fold.

This thesis focuses on porous, mineralized as well as unmineralized, type I collagen-glycosaminoglycan (CG) scaffolds for soft and hard tissue regeneration. Collagen is a significant constituent of natural extracellular matrices (ECM) and possesses the right biochemical properties such as low level of antigenicity and optimal biodegradation rate without release of toxic products [61]. Collagen is amenable to very high degree of purification and, in the form of reconstituted crosslinked fiber, tape, or membrane, is sufficiently tough to be useful in many surgical applications. The physical properties of solid collagen are also relatively well understood. Even though the biodegradation rate of collagen can be adjusted over a wide range by controlling the crosslink density, heavily crosslinked collagen is a stiff, brittle material [61]. Coprecipitation of collagen with glycosaminoglycan (GAG) yields membranes which are significantly more resistant to degradation than is pure collagen and can be used as an alternative to crosslinking for control of biodegradation. In addition, CG copolymer possesses significantly higher modulus of elasticity and higher energy to fracture than pure collagen. Another reason for using GAG is that CG scaffolds exhibit a significantly more open pore structure than the GAG-free collagen scaffolds [61]. CG scaffolds made from collagen have been used in a variety of applications [24].

1.4 Collagen-GAG (CG) scaffolds for soft tissue regeneration

Dermal and nerve regeneration templates

CG scaffolds were originally developed by the research group of Prof. I. V. Yannas at the Massachusetts Institute of Technology and were first used for the dermal-regeneration-template (DRT) in 1975. This was followed by DRT's early clinical use (1979), as a cell-

seeded scaffold to regenerate skin (1981), and its eventual approval by the US Food and Drug Administration (FDA) for the treatment of massively burned patients and patients undergoing plastic and reconstructive surgery of the skin. This was the first tissue-engineered device approved by the FDA (1996) [62]. Recently, the cell-free DRT scaffold (Integra LifeSciences) was found to be a very effective treatment, by induction of skin regeneration, for deep skin ulcers in patients [63]. Another scaffold developed by Yannas' group, the nerve regeneration template (NRT), has induced regeneration of peripheral nerves across unprecedented distances (> 25 mm); an early version has been approved by the FDA for treatment of patients suffering from paralysis resulting from severe injury in the peripheral nerves of the arms, legs or the face [24, 62]. Figure 1.2 shows scanning electron micrographs of the DRT scaffold and the nerve regeneration template developed by Prof. Yannas at MIT. CG scaffolds have also been used for a wide variety of *in vitro* studies of cell migration, contraction, and tissue growth [4, 24, 64-66].

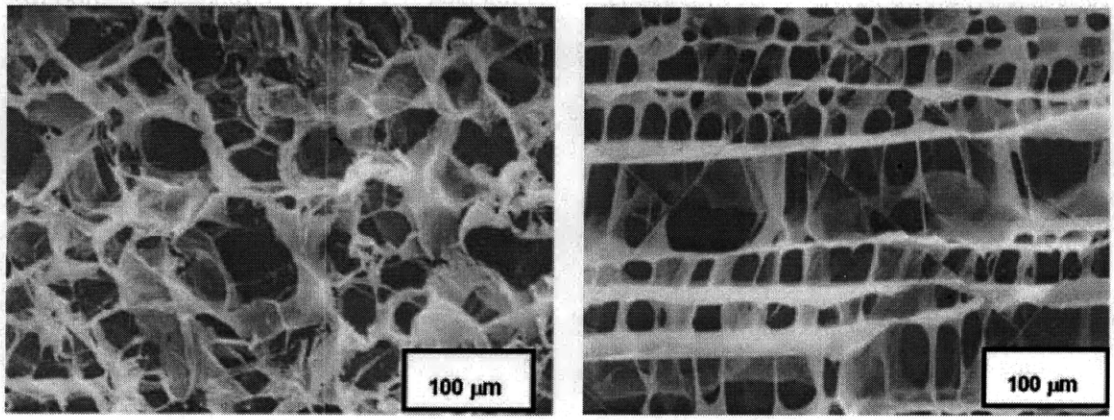

(a) (b)

Figure 1.2. (a) The dermal regeneration template (DRT) and (b) the nerve regeneration template (NRT) developed by Yannas *et al.* at the Massachussetts Institute of Technology [67].

Fabrication of the CG suspension

To fabricate CG scaffolds, a collagen-glycosaminoglycan suspension is first produced. Microfibrillar type I collagen is mixed with acetic acid (0.05M, $pH \sim 3.2$). The low *pH* acetic acid solution acts to swell the collagen fibers, destroying the native banding structure of collagen but keeping the triple-helical structure intact [61]. These structural modifications reduce host immunological response and significantly prolong the whole-blood clotting time of the scaffold that is critical for bonding of the scaffold to the defect site [61]. A glycosaminoglycan (GAG), typically chondroitin 6-sulfate, is then added to the collagen-acetic acid mixture. Spontaneous crosslinks are formed between the collagen fibrils and the GAG, resulting in the formation of a collagen-GAG suspension in the aqueous acetic acid phase.

Freeze drying of the CG scaffolds

The CG scaffold is manufactured by freeze-drying the CG suspension. Freeze drying is a two step process in which a temporary space holding network is infiltrated with the material to be shaped and then removed during the sublimation step. The temporary network is formed *in situ* by freezing the solvent in the CG suspension (i.e., acetic acid solution) below its melting point. In the second step the network is then removed by sublimation of ice crystals formed during freezing, avoiding any liquid contact of the biomaterial which might otherwise dissolve. Freeze drying is best described using an illustration (Figure 1.3) of the phase diagram of the CG suspension during the process. At first the CG suspension is frozen from the initial room temperature and pressure to a freezing temperature at a constant cooling rate (A to B in Figure 1.3). Previously, quenching was used to freeze the CG suspension; however, due to variable heat transfer

through suspension, the pore microstructure was heterogeneous. A constant cooling rate during freezing ensures a more controlled heat transfer and hence a homogeneous pore microstructure. The suspension is then kept at T_f and P_{atm} for time, t_f, where t_f is long enough (usually ~ 1 hr) to completely solidify all the solvent. During this step the CG co-precipitate is localized between the growing ice crystals, forming a continuous, interpenetrating network of ice and the CG co-precipitate. Finally upon application of vacuum (P_{sub}) and heating (T_{atm}) for time t_{sub}, direct sublimation removes the ice crystals (B to C in Figure 1.3), leaving a highly porous scaffold structure where the scaffold microstructure is defined by the ice crystals formed during solidification. Ultimately the scaffold is brought back to room temperature and pressure (C to A in Figure 1.3).

Pore size can be controlled by controlling the size of the ice crystals that nucleate during freezing of the CG suspension [68]. Final pore size depends on both the nucleation rate and the growth rate of the ice crystals. The number density of the pores will depend mostly on nucleation (highest at largest undercooling). Nucleation of ice crystals can be increased by increasing the chemical free energy (and so the under-cooling ~ T_m - T_f), where T_m is the melting temperature of the solvent (~ 0.01°C). Hence by decreasing T_f much below T_m the final pore size can be decreased [68]. Slower cooling rate during freeze drying has the effect of decreasing the nucleation rate and increasing the growth rate of the ice crystals that do form, making them larger than the ones formed at higher cooling rates (where nucleation is delayed to lower temperatures where more ice crystals nucleate but they can not grow as much).

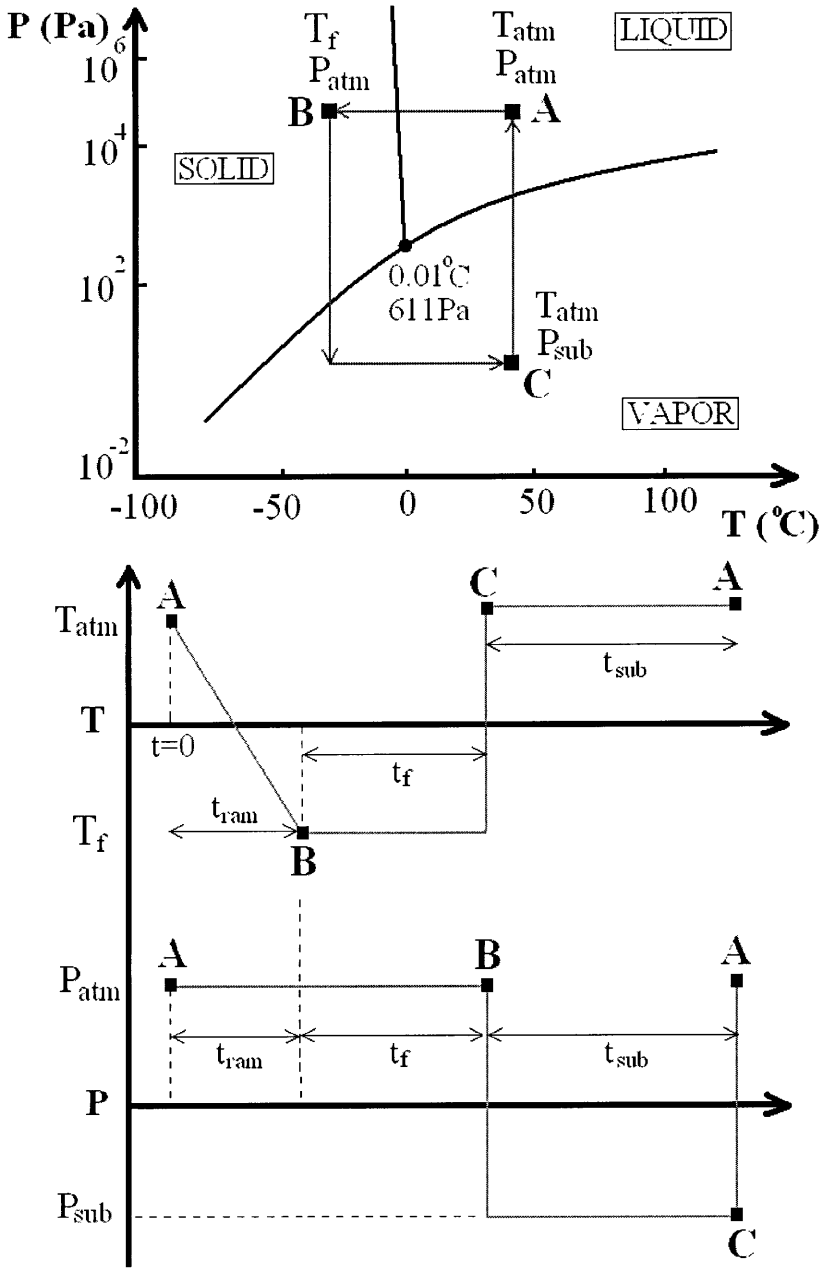

Figure 1.3. Phase diagram of the CG suspension during freeze drying [4].

Crosslinking of the CG scaffolds

Crosslinking is carried out after freeze drying. The extent of crosslinking depends on the required mechanical properties and degradation rate of the scaffold. Highly crosslinked scaffolds impart high strength and stiffness but they take longer to degrade. Therefore we have to optimize the degree of cross-linking for the required mechanical properties and degradation rate. Crosslinking can be chemical (e.g., glutaraldehyde or carbodimide) or physical (e.g., dehydrothermal treatment or ultraviolet irradiation) [4, 31, 68]. However, in case of the chemical crosslinking, there is a risk of post-implantation toxicity due to residual crosslinking agent. Here we will describe only two methods that are important for collagen-GAG scaffolds: dehydrothermal treatment (DHT) and carbodimide crosslinking. DHT involves exposure of collagenous biomaterial to heating at 105^0C under vacuum (~30 mTorr) for 24 hours. This results in crosslinking between the polypeptide chains of the collagen fibers. 1-ethyle-3-(3-dimethylaminopropyl) carbodimide (EDAC) is used to create chemical crosslinking between the carboxyl group ($COOH^-$) of GAG and the amino group of collagen. The degree of cross-linking is varied by the addition of N-hydroxysuccinimide (NHS). Optimization of the ratio of EDAC to NHS to $COOH^-$ groups can also further affect the extent of cross-linking [69]. EDAC crosslinking is carried out in the hydrated state where the scaffolds are hydrated in deionized water for ~15 min followed by mixing the required amount of EDAC/NHS solution into the deionized water and maintaining the scaffold in this solution for ~1 hr. The scaffolds are subsequently freeze dried to obtain dry scaffolds.

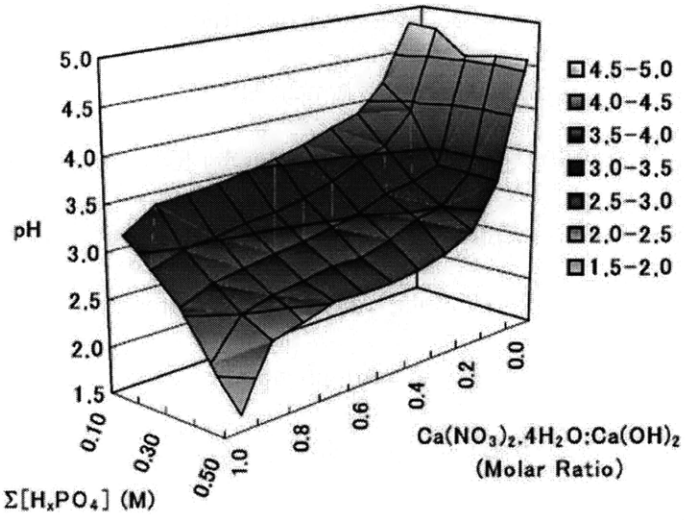

(a)

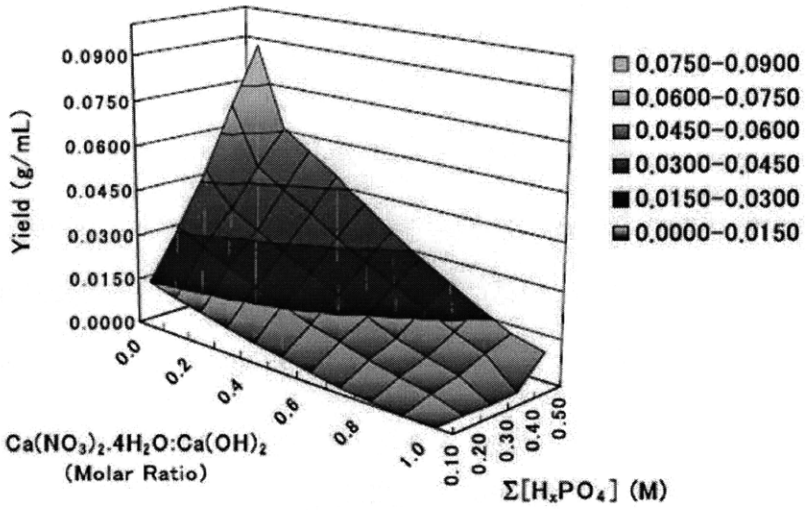

(b)

Figure 1.4. (a) Contours of *pH* and (b) mass yield of the mineral for the titrant free triple co-precipitation method [69, 70].

1.5 Mineralized collagen-GAG (MCG) scaffolds: titrant free triple co-precipitation method

As described above (section 1.3), current methods used to fabricate mineralized composite scaffolds do not mimic the nanoscale structure of bone even though they increase the mechanical properties by many times. The most recent fabrication technique, developed by Lynn *et al.* [70-73], improves upon this by forming a triple co-precipitate of mineral, collagen and glycosaminoglycan, without using a titrant, by controlling the molarity of the reactant acid and molar ratios of the different calcium sources. Three reactants in this case are used: (1) solvent–phosphoric acid (H_3PO_4) solution, (2) dry calcium nitrate ($Ca(NO_3)_2.4H_2O$) powder, and (3) dry calcium hydroxide ($Ca(OH)_2$) powder; Ca:P ratio is always kept at 1:1.

Control of pH and mineral content

Different concentrations of H_3PO_4 and ratios of calcium-nitrite:calcium-hydroxide are responsible for different *pH* and different mass yield of the mineral. Contours of *pH* and mass yield are drawn versus concentrations of H_3PO_4 and ratios of calcium-nitrite:calcium-hydroxide (Figure 1.4). Therefore for a particular *pH* there will be a locus of points on the H_3PO_4 concentration and nitrite:hydroxide ratio. For the same locus of points, there will be different mass yields and hence we can obtain a particular combination of "H_3PO_4 concentration and nitrite:hydroxide ratio" for which the mass yield will be maximum. Hence this is useful in fabricating scaffolds with control over the amount of mineral content. In addition, the *pH* is maintained below 4.25 ± 0.30, assisting in the *in situ* co-precipitation of the mineral phase within the collagen fibers, increasing the mechanical properties of the scaffold while mimicking the natural bone structure. The *pH* of the triple co-precipitate slurry for mineralized CG scaffolds with different mineral

contents is shown in Figure 1.5. As described above, co-precipitation of CG copolymer takes place at an acidic *pH* of 3.2 [61]. At this low *pH* the stable calcium phosphate phase obtained in the triple-co-precipitation method is brushite ($CaHPO_4.2H_2O$). Freeze drying is then used to fabricate porous dry scaffolds from the triple co-precipitated slurry [74]. Mineralized collagen-GAG scaffolds are cross-linked through any of the two methods described above (section 1.4), preferably EDAC.

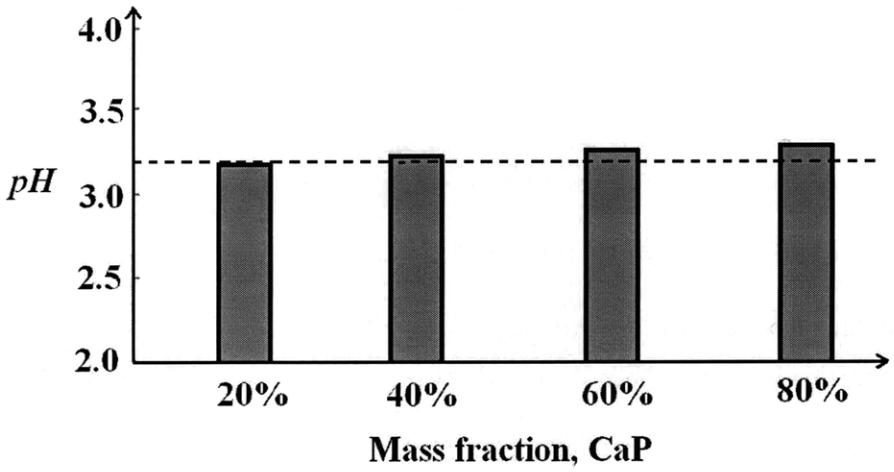

Figure 1.5. *pH* of the triple co-precipitate for different mineral content mineralzied CG suspension [69, 70].

Control of biodegradability via hydrolysis

In addition to the extent of crosslinking, the other factor that affects bio-degradability is the ratio of different mineral phases in the scaffold [69]. Bone has collagen microfibrils which are surrounded by very small crystals of hydroxyapatite, whose unit cell contains $Ca_{10}(PO_4)_6(OH)_2$. However the bone mineral is impure and has many structural substitutes (e.g., carbonate, fluoride, citrate). As described above, the stable mineral phase obtained under an acidic *pH* is brushite. However, brushite can be converted to

octacalcium phosphate ($Ca_8(HPO_4)_2(PO_4)_4.5H_2O$) and octacalcium phosphate in return can be converted to hydroxyapatite through hydrolytic conversions. Therefore different compositions of these three forms can be maintained in the final scaffold by carrying out partial hydrolytic conversions. However, brushite is very soluble where as hydroxyapatite is less soluble with octacalcium phosphate some where intermediate between them. Hence by varying the relative composition of these three mineral phases, we can vary the bio-degradability of the scaffold. Mineralized CG scaffolds with 50% by weight mineral has been developed via titrant free triple co-precipitation method by Lynn *et al.* [69, 70, 75]; the relative density of which is 0.15.

1.6 Chondral and osteochondral defects

Current repair strategies and limitations

Bi-layer scaffolds have also been designed for regenerative repair of chondral (defective cartilage) and osteochondral (defective cartilage as well as subchondral bone) defects of articular cartilage [76]. The current strategies for clinical treatment of these defects include microfracturing (Figure 1.6a), mosaicplasty (Figure 1.6b), and autologous chondrocyte implantation (ACI) (Figure 1.6c) [19]. Microfracturing involves removing the defective cartilage followed with making perforations, or "microfractures", in the subchondral bone plate, introducing blood and marrow into the cartilage defect. This in turn stimulates formation of fibrin clot that acts as a provisional scaffold into which cells can migrate and begin synthesizing reparative tissue [77]. It has been reported that the reparative tissue formed post microfracture in human is primarily fibrocartilage that is not as efficient as healthy cartilage for long term load-bearing situations [78]. Mosaicplasty

involves transplanting single or multiple cylindrical healthy osteochondral grafts taken from low load-bearing regions of the joint into holes created at the defect site. Several inherent difficulties with this procedure include: donor site morbidity [79], chondrocyte death due to the harvest procedure [80] and impact loading during the placement of the graft [81], mismatch of stiffness between transplanted and recipient tissue [82], increase in subchondral bone density at the recipient tissue [82], and incomplete integration with the host cartilage [83]. Autologous chondrocyte implantation involves implanting autologous chondrocytes which have been proliferated *in vitro*. Cartilage biopsies from low load-bearing regions of the same or other joints are enzymatically digested to isolate the chondrocytes. The cells are expanded *in vitro* to obtain a sufficient number to populate the defect site when re-implanted. The defect site along with the condrocytes is then sealed using a periosteal flap that is sutured in place and glued via fibrin glue. However, it has been shown that the reparative tissue formed post ACI is primarily fibrocartilage that is not as efficient as healthy cartilage for long term load-bearing situations [8].

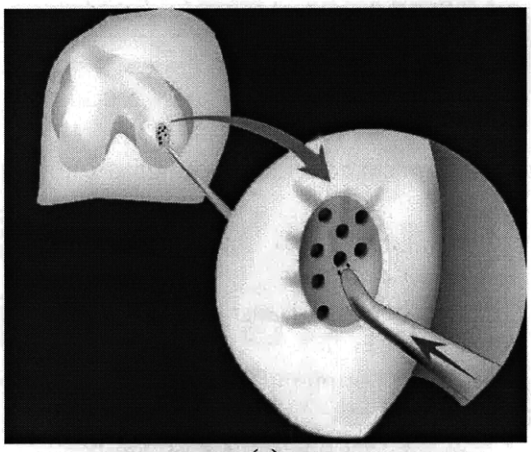

(a)

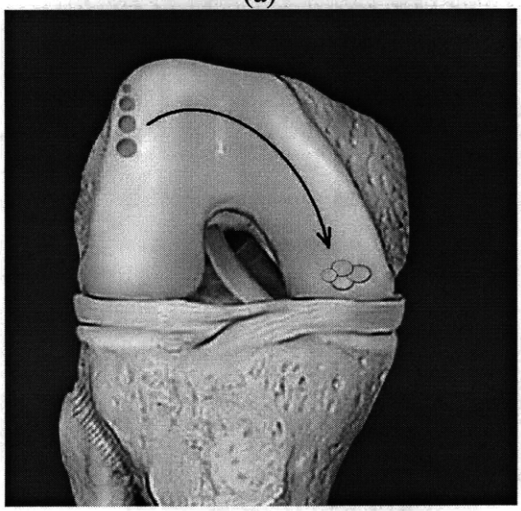

(b)

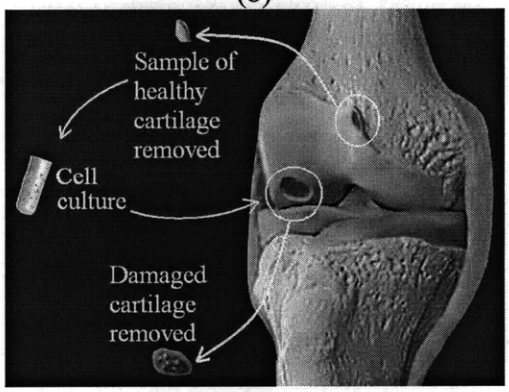

(c)

Figure 1.6. Current repair strategies for cartilage chondral and osteochondral defects: (a) microfractures, (b) mosaicplasty, and (c) autologous chondrocyte implantation.

Proposed method using a bi-layer scaffold

The proposed new procedure involves removing the defective cartilage as well as the subchondral bone below the defective cartilage and replacing it with two layers of scaffold, one for the cartilage and the other for the bone. The top layer is unmineralized collagen-GAG scaffold for cartilage repair while the bottom layer is mineralized collagen-GAG scaffold for bone regeneration (Figure 1.7). This procedure using a bi-layer scaffold has been shown to regenerate cartilage and bone in an osteochondral defect in a goat knee joint by Vickers *et al.* [19]. As said earlier, the closer the scaffold composition and structure are to the real tissues, the better the regeneration. In an articular joint, the interface between the bone and cartilage is diffused that decreases any sharp gradients in mechanical properties (mostly shear properties) at the interface. Therefore it is desirable to have a diffuse interface between the two layers of scaffold. This is accomplished by pouring one slurry on top of the other: collagen-GAG slurry is kept on the bottom and mineralized collagen-GAG slurry is kept on top of it. They are allowed to inter-diffuse at the interface for ~5 min. The combined layers of slurries then undergo normal freeze drying. The advantage of this procedure is to obtain an inter-diffused bi-layer without any sharp gradients in mechanical properties. As described earlier EDAC crosslinking is compatible for both the layers (collagen-GAG and mineralized collagen-GAG) and therefore the bi-layer scaffold is crosslinked via EDAC after freeze drying.

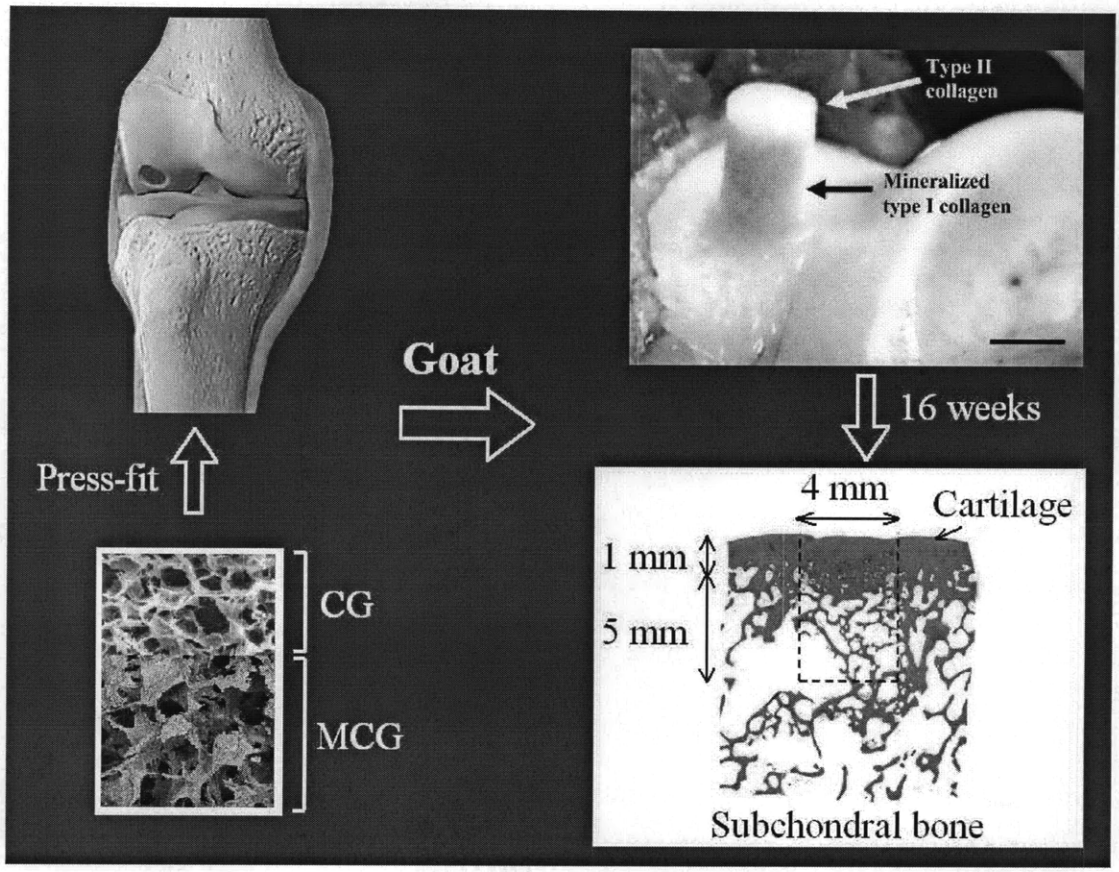

Figure 1.7. Proposed method to repair chondral and osteochondral defects using a bi-layer CG scaffold.

1.7 Mechanical properties of the collagen-based scaffolds

CG scaffolds

Quantitative mechanical analysis of CG scaffolds, previously found to have equiaxed pores and a uniform pore microstructure (ρ^*/ρ_s: 0.0058; mean pore size: 96–121 μm) [66, 68], has been performed by Harley *et al.* [17]. The effect of mean pore size, crosslink density, and relative density on scaffold mechanical properties (Young's modulus, E^*, and collapse strength, σ^*) for the unmineralized CG scaffold has been listed in Table 1.3 [17]. Mechanical properties were found to be independent of the pore size (or mean pore

diameter). Hydration decreased the mechanical properties further by a factor of 150 for the Young's modulus and 250 for the collapse strength. Post-fabrication crosslinking increased the mechanical properties by a factor of 7 for Young's modulus, and by a factor of 3.6 for the collapse strength. With an increase in relative density by a factor of 3, the mechanical properties roughly increased by 3 times. However, the elastic strain, ε^*, remained independent of pore size, crosslink density, and relative density. The Young's modulus (E_s) of the individual scaffold struts (dry and DHT crosslinked) that define the scaffold microstructure was measured via AFM to be 762 MPa [17].

Test	Scaffold Variant	E^*	σ_{el}^*	ε_{el}^*	$\Delta\sigma/\Delta\varepsilon$
Effect of mean pore size (dry)		**E^*, kPa**	**σ_{el}^*, Pa**	**ε_{el}^***	**$\Delta\sigma/\Delta\varepsilon$, kPa**
	96 μm	31.7 ± 3.9	5350 ± 630	0.184 ± 0.017	7.0 ± 0.9
	110 μm	28.5 ± 3.4	4810 ± 520	0.196 ± 0.024	9.2 ± 1.5
	121 μm	29.8 ± 3.9	5290 ± 280	0.202 ± 0.021	10.6 ± 1.9 *
	151 μm	39.4 ± 4.5 *	6250 ± 280 *	0.182 ± 0.027	13.9 ± 3.8 **
Effect of mean pore size (hydrated)		**E^*, Pa**	**σ_{el}^*, Pa**	**ε_{el}^***	**$\Delta\sigma/\Delta\varepsilon$, Pa**
	96 μm	206 ± 36	18 ± 4	0.079 ± 0.017	98 ± 15
	110 μm	176 ± 41	14 ± 8	0.076 ± 0.031	83 ± 11
	121 μm	221 ± 47	31 ± 5 *	0.151 ± 0.055 *	93 ± 11
	151 μm	229 ± 22	22 ± 4	0.107 ± 0.022	94 ± 18
Effect of crosslink density (hydrated)		**E^*, normalized**	**σ_{el}^*, normalized**	**ε_{el}^*, normalized**	**$\Delta\sigma/\Delta\varepsilon$, normalized**
	Standard	***208 ± 41 Pa***	***21 ± 8 Pa***	***0.10 ± 0.04***	***92 ± 14 Pa***
	NX	0.74 ± 0.13	0.73 ± 0.096	0.94 ± 0.073	0.85 ± 0.23 *
	DHT105/24	***1.00 ± 0.051*** *	***1.00 ± 0.057***	***1.00 ± 0.093***	***1.00 ± 0.087***
	DHT120/48	1.08 ± 0.063 *	1.03 ± 0.076	1.02 ± 0.091	1.03 ± 0.11
	EDAC1:1:5	2.0 ± 0.11 **	1.06 ± 0.65	0.72 ± 0.42	1.25 ± 0.14 **
	EDAC5:2:1	7.20 ± 0.14 ***	3.59 ± 0.87 *	0.83 ± 0.35	3.06 ± 0.18 ***
Scaffold isotropy (dry)		**E^*, normalized**	**σ_{el}^*, normalized**	**ε_{el}^*, normalized**	**$\Delta\sigma/\Delta\varepsilon$, normalized**
	Standard	***30.0 ± 3.9 kPa***	***5.2 ± 0.53 kPa***	***0.20 ± 0.02***	***10.2 ± 3.3 kPa***
	x-axis	0.81 ± 0.27	0.64 ± 0.21 *	1.00 ± 0.18	0.58 ± 0.071
	y-axis	1.01 ± 0.15	0.94 ± 0.11	1.00 ± 0.11	0.66 ± 0.25
	z-axis	***1.00 ± 0.13***	***1.00 ± 0.17***	***1.00 ± 0.095***	***1.00 ± 0.23*** *
Effect of relative density (dry)		**E^*, normalized**	**σ_{el}^*, normalized**	**ε_{el}^*, normalized**	**$\Delta\sigma/\Delta\varepsilon$, normalized**
	Standard	***30.0 ± 3.9 kPa***	***5.2 ± 0.53 kPa***	***0.20 ± 0.02***	***10.2 ± 3.3 kPa***
	0.006 (1.0x)	***1.00 ± 0.11***	***1.00 ± 0.10***	***1.00 ± 0.019***	***1.0 ± 0.082***
	0.009 (1.5x)	1.28 ± 0.11 *	1.21 ± 0.063 *	1.05 ± 0.042	2.16 ± 0.065 *
	0.012 (2.0x)	2.24 ± 0.058 **	2.06 ± 0.025 **	1.00 ± 0.065	3.32 ± 0.049 **
	0.018 (3.0x)	2.76 ± 0.10 ***	2.77 ± 0.62 ***	1.25 ± 0.064 *	8.66 ± 0.062 ***

Table 1.3. Effect of mean pore size, crosslink density, and relative density on the mechanical properties (measured through unconfined comrepssion tests) of the unmineralized CG scaffold. *, **, and *** denote distinct, statistically signficant results [17].

	Scaffold	E^* (kPa)	σ^* (kPa)	Porosity (%)	Reference
Synthetic polymer + ceramic	PCL/TCP (80:20 by wt.)	9,300-15,600	3,100-4,400	43	[47]
	PLGA/HA (50:50 by wt.)	4,500	-	91	[84, 85]
	PLA/CaP glass (60:40 by wt.)	120	20	97	[40]
	PLLA/TCP (50:50 by wt.)	60,110	4,710	89	[46]
	PLLA/HA	10,000	400	90-95	[45]
	PLLA/HA (50:50 by wt.)	10,870	390	90	[44]
	PLGA/HA fibers	40,000-75,000	1,000-3,000	50-60	[39]
	PLA/HA	5,000-11,000	300-400	86-92	[86]
	Polyethylene/HA (33:77 by wt)	5,000	5	70	[42]
	Polyethylene/HA (50:50 by wt)	30,000	9	60	[42]
	Polyurethane/CaP glass		1,500		[87]
Natural polymer + ceramic	Collagen/HA (varying mineral content)	37-82	-	87-95	[88]
	Collagen/HA (20:80 by wt.)	50-300	30-60	95	[55]
	MCG (50 wt% mineral)	762	85	85	[69]
	Collagen/alginate/HA	50,000-350,000	5,000-25,000	65-80	[54]
	Gelatin/HA (10-30% HA)	2,280-4,010		85	[89]
	Chitosan/Gelatin/TCP	830-10,880	90-880	-	[51]
	Chitosan/TCP	1,000-3,000	100-300	90	[90]
Unmineralized	Collagen/PGA fibers (80/20 by wt)	18	-	85	[91]
	PLGA	30,000	750	75	[39]
	PLA	75	18	93	[40]
	Unmineralized CG	30	5	99	[17]
Pure Ceramic	CaP cement	150,000	500	80	[92]
	Macro-porous HA	1,240,000	34,400	40	[93]

	Micro- & Macro-porous HA	1,110,000	27,400	70	[93]
Bones	Cancellous bone	10,000-1,000,000	1,000-30,000	75-95	[94-96]
	Cortical bone	10,000,000-20,000,000	110,000-180,000	5-10	[94-96]

Table 1.4. Elastic moduli and collapse strrengths of various bone regeneration scaffolds in the dry state.

MCG scaffolds

The mechanical properties of the dry mineralized scaffolds fabricated by Lynn *et al.* are compared to other synthetic and natural polymer based scaffolds for bone regeneration in Table 1.4 [69, 74, 75]. Among the mineralized natural polymer/ceramic scaffolds, scaffolds with higher mechanical properties than the mineralized CG (50% mineral by weight) scaffolds have either gelatin or a third component (chitosan or alginate) in them. Their chemical compositions vary from natural bone, and hence, are not biomimetic in a true sense. The effect of mineralization of CG scaffolds is apparent by comparing the properties of the mineralized scaffolds to the unmineralized CG scaffolds.

Tissue	E^* (MPa)	σ^* (MPa)	Reference
Tendon	870	72	[97]
Ligament	515	54	[98]
Cancellous bone	90-1000	1-30	[94-96]
Cortical bone	10,000-20,000	110-254	[94-96]

Table 1.5. Young's modulus, E^*, and strength, σ^*, of tissues facing relatively higher mechanical loads.

1.8 Goal of this thesis: increasing the mechanical properties of collagen-based scaffolds

The mechanical properties of the mineralized and unmineralized CG scaffolds are much lower than some of the tissues facing higher mechanical stresses *in-vivo* such as tendon, ligament, and bone (Table 1.5). However, the mechanical properties for the tissues listed in Table 1.5 are the properties of fully developed tissues. As described above, the scaffold should mimic the natural extracellular matrix of the tissue to have better regenerative capability [5, 20, 22, 61, 63, 99]. The mechanical properties of the natural extracellular matrix are lower than the fully developed tissues; e.g., osteoid (ground collagenous precursor which later mineralizes to form bone along with the bone cells) has lower Young's modulus (~25-40 kPa) than that of cencellous and cortical bones (Table 1.5) [26]. The properties of the CG scaffolds (both mineralized and unmineralized) are lower than the natural extracellular matrix; e.g., hydrated mineralized CG scaffold has Young's modulus of about 4 kPa [74] that is lower than the 25-40 kPa for the osteoid [26]. The goal of this thesis is to improve the mechanical properties of the collagen-based scaffolds to match upto the mechanical properties of the natural extracellular matrix.

Apart from mimicking the natural extracellular matrix, mechanical properties of the scaffolds are critical for many other reasons. First, as described above, mesenchymal stem cells differentiate into specific lineage and commit to phenotypes (neurogenic, myogenic, and osteogenic) depending on the matrix elasticity [26]. Second, it is critical that the scaffold should have sufficient stiffness and strength to maintain its shape and size during surgical procedures such as implantation and to enhance tissue in-growth while preventing encroachment of competing cell types after implantation [100].

Therefore, the mechanical properties of the mineralized and unmineralized CG scaffolds have to be improved significantly for tissues such as ligament, tendon, and bone. For the mineralized CG scaffold, we set our target Young's modulus in the hydrated state to be the modulus at which MSC stem cells differentiate into osteoblast-like cells: 25-40 kPa [26]. For the unmineralized CG scaffolds our target was to increase the Young's modulus as much as possible. In addition, another target for both mineralized and unmineralized CG scaffolds was that the strength of the dry scaffolds should be enough to withstand hard thumb pressure (~ 100-200 kPa) that the scaffold frequently faces during implantation at the defect site. In order to improve the mechanical properties, we need to understand the deformation mechanism in porous solids (or foams). The following section explains the deformation mechanism of porous foams and shows similarity between the mechanical behaviors of CG scaffolds and porous foams.

1.9 Cellular solids model

The compressive stress–strain curves for unmineralized and mineralized CG scaffolds with elastomeric and elastic-plastic foams are shown in Figure 1.8. The mineralized and unmineralized CG scaffolds exhibited stress–strain behavior characteristic of low-density, open-cell foams with distinct linear elastic, collapse plateau and densification regimes. Therefore mineralized and unmineralized CG scaffolds with an interconnected network of pores defined by struts can be mechanically as well as microstructurally modeled as a low-density foam structure. The characteristics of open cell foams are discussed in detail in section below. Modeling them as cellular solids provides a powerful tool to investigate and describe the salient features of a scaffold. In nature, materials with

a cellular (porous) structure are widespread, and extensive study and modeling of the microstructural and mechanical properties of these materials has been performed [95]. The microstructural features of cellular solids affect their mechanical performance.

Foams, with their polyhedral cells, are three dimensional cellular solids and can be either open cell (with solid only at the edges of the polyhedra exhibiting pore interconnectivity) or closed cell (with solid membranes over the faces of the polyhedra without exhibiting pore interconnectivity). Pore interconnectivity is critical for scaffold bioactivity because cells need to be able to migrate through the construct and to interact with other cells in a manner similar to that observed *in vivo*. An active ECM analog must possess an open-cell pore structure with a relative density below a critical value that is characteristic of each application, but is typically significantly < 10% (or porosity typically > 90%) [24]. These structural criteria, determined from the results of a number of experiments studying cell-scaffold interactions, suggest that a critical number of cells are required within a bioactive scaffold [24]. The relative density, also termed the solid volume fraction *(SVF),* is the most important parameter that determines the mechanical properties of the foam. The relative density is the density of the cellular solid divided by that of the solid it is made from. Porosity, also termed the pore volume fraction *(PVF)* of a scaffold, is another variable often used interchangeably in the tissue engineering literature to describe scaffold microstructure; $PVF = 1 - SVF$.

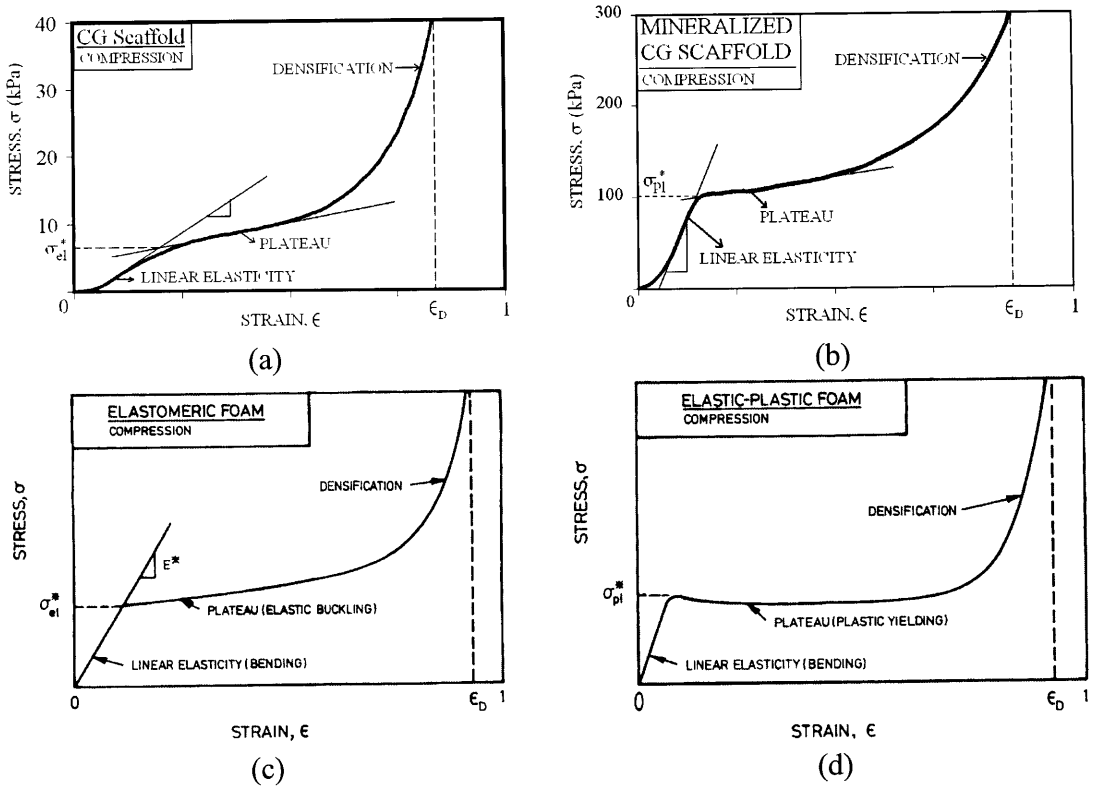

Figure 1.8. Compressive stress-strain curves for (a) unmineralized-, (b) mineralzied-CG scaffolds, (c) elastomeric foam, and (d) elastic-plastic foam [17, 95, 101, 102].

The stress–strain curve for a foam in compression is characterized by three distinct regimes (Figure 1.8): (1) a linear elastic regime (controlled by strut bending), (2) a collapse plateau regime (controlled by struts elastically buckling, or plastically yielding , or brittle crushing, depending on the nature of solid from which the foam is made) and (3) a densification regime (complete pore collapse throughout the material). The mechanical response of cellular solids has been modeled by using dimensional analysis of the deformation and the failure mechanisms of the foam depending on the nature of the solid it is made from [95]. Dimensional analysis assumes that the polyhedral cells in foams of different relative densities are geometrically similar. This method gives the

dependence of mechanical properties on the relative density and the mechanical properties of the solid it is made from. However, the constants associated with the pore geometry are determined empirically. The specific equations with the respective constants used to model mineralized and unmineralized CG scaffolds are described in the respective chapters.

1.10 Thesis organization

As described above: the mechanical properties of the foam (or scaffolds) depend on the relative density of the foam and the mechanical properties of the solid the foam is made from. Therefore, the two obvious ways to increase the mechanical properties of the scaffold are to: (1) increase the relative density of the scaffold, and (2) increase the mechanical property of the solid the scaffold is made from. In this work, we have explored these two methods in the case of mineralized and unmineralized CG scaffolds. The thesis is organized in the following manner:

- Chapter 2: We attempted to increase the mechanical properties of the mineralized CG scaffold by increasing the solid mechanical properties using a higher mineral content scaffold. The microstructure and mechanical properties of mineralized CG scaffolds with different mineral content is described in chapter 2 (which is based on my published work in Acta Biomaterialia [103]). The measured mechanical properties of the mineralized CG scaffolds were compared with models for cellular solids. It was found, somewhat unexpectedly, that increasing the mineral content introduced defects such as cracked and disconnected pore walls into the scaffold, which resulted in a net decrease in the scaffold mechanical properties.

- Chapter 3: Next, we attempted to increase the relative density of the mineralized CG scaffold by using slurries of higher solids content. The higher viscosity of the slurry made it difficult to mix and obtain a homogeneous scaffold. We found we could produce a higher density mineralized scaffold by starting out with the low density slurry and suctioning off solvent using a vacuum pump. The process that was developed and the microstructure and mechanical properties of the resulting scaffolds are described in chapter 3 (which is based on my published work in Acta Biomaterialia [103]). The resulting scaffolds were up to 4 times as dense as the initial ones, with mechanical properties about 10 times that of the original scaffold. The measured mechanical properties of the mineralized CG scaffolds were also compared with models for cellular solids.

- Chapter 4: We next applied the same modified vacuum process to unmineralized CG scaffolds to increase the relative density. The measured mechanical properties of the unmineralized CG scaffolds were compared with models for cellular solids. Models for cellular solids also suggest that the surface area per unit volume (and hence the number of binding sites per unit volume) increase with square root of the relative density. Therefore we completed our study by measuring the cell attachment on CG scaffolds of increasing relative density in chapter 4 (which is based on my submitted work in Acta Biomaterialia [104])

- Chapter 5: The conclusion of the study and recommendations for future research are described in chapter 5.

CHAPTER 2. Microstructure and Mechanical Properties of Mineralized Collagen-Glycosaminoglycan Scaffolds with Increased Mineral Contents

2.1 Introduction

Scaffolds for tissue regeneration are structural mimics of the extracellular matrix of the tissue and can be made of bio-degradable synthetic polymers (e.g., polylactic and polyglycolic acid) or natural polymers (e.g., collagen, collagen-glycosaminoglycan copolymer). It has been demonstrated that scaffold pore size and shape, porosity, specific surface area, biodegradability and stiffness significantly influence cell functions [4]. A variety of fabrication techniques have been developed for different biomaterials. For instance, synthetic polymer scaffolds can be made by negative mold infiltration, ceramic scaffolds can be made by a casting and sintering operation, and collagen scaffolds are formed by freeze-drying (described in more detail below). Recently, attempts have been made to regenerate bone using synthetic [41, 46, 95, 105-107] as well as natural polymer scaffolds [69-72, 74-76, 108-110].

Bone is comprised principally of the fibrous protein collagen (type I), impregnated with a mineral closely resembling hydroxyapatite, $Ca_{10}(PO_4)_6(OH)_2$; it also contains non-collagenous proteins and water [94, 96]. The bone mineral is impure and has many

structural substitutes (e.g., carbonate, fluoride and citrate); crystals are initially precipitated between and within the layers of collagen molecules [94, 96]. Living cells (osteocytes, osteoblasts and osteoclasts) populate the vascularized extracellular matrix. The Young's modulus of wet cancellous bone ranges from 0.09-1.0 GPa, while that of wet cortical bone ranges from 10-20 GPa, depending on the direction of loading. The relative density (the density of the porous solid, ρ^*, divided by that of the solid from which it is made, ρ_s) of cancellous bone ranges from 0.05-0.6 [94, 96].

To optimize the regenerative capability of a scaffold, it is generally believed that the composition and physical/mechanical properties of the scaffold should be similar to that of the physiological extracellular matrix [5, 20, 22, 61, 63, 99]. To this end, collagen-glycosaminoglycan (CG) scaffolds have been developed and used clinically for skin regeneration and experimentally for nerve regeneration over the past decade [5, 17, 22, 61, 63, 66, 68, 99, 101, 102, 111]. CG scaffolds are primarily manufactured through a freeze-drying process. Briefly, an aqueous CG slurry suspension is frozen to obtain interconnected ice crystals of the required size and shape. Sublimation of the frozen slurry leaves behind the foam-like network of struts with interconnected pores. Subsequently, the scaffolds are cross-linked to obtain the required mechanical properties and biodegradability. Extensive mechanical characterization of CG scaffolds has been reported by Harley *et al.*. [17]. To mimic natural bone tissue, a mineral phase similar to hydroxyapatite must be added to the CG scaffold. A major area of recent progress has been the fabrication of mineralized bio-organic composites [60, 89, 112-115]. Most of these processes include mechanical mixing of the desired amount of monolithic calcium

phosphate with the bio-organics. The major problem with these methods is that the mineral phase does not form *in situ* and simply adheres to the outside of the collagen fibers. Other techniques yield *in situ* formation of calcium phosphate on the bio-organic component by adjusting the *pH* via a titrant phase. However, these techniques have difficulty in controlling the mass yield of mineral phase as well as in removing the residual titrant phase. The most recent fabrication technique, developed by Lynn *et al.*. [69, 70, 72, 74-76, 110], improves upon this mineralization process by forming a triple co-precipitate of mineral, collagen and glycosaminoglycan, without using a titrant, by controlling the molarity of the reactant acid and molar ratios of the different calcium sources. Due to the *in situ* co-precipitation of the mineral phase, calcium phosphate crystals form within the collagen fibers, resulting in a more uniformly mineralized scaffold. Freeze drying is then used to fabricate porous scaffolds from the triple co-precipitated slurry.

Scaffolds with well-characterized and controllable chemical, mechanical and micro-structural properties are also suitable for basic *in vitro* studies of cell interactions. The mineralized CG scaffold developed by Lynn *et al.* [74-76] had 50% mineral content by weight. However, extensive mechanical characterization of these newly developed mineralized collagen-glycosaminoglycan (MCG) scaffolds has not yet been done. The Young's modulus and collapse strength of the scaffolds in the hydrated state were ~4 kPa and ~0.3 kPa, respectively. These properties are much lower than that of mature cortical and trabecular bone (Table 1.5). As described in chapter 1, our proposed new procedure for chondral and osteochondral defects involves a bi-layer scaffold with a mineralized

CG scaffold as the bottom layer that would support the mesenchymal stem cells from the bone marrow space. It has been shown that mesenchymal stem cells differentiate to osteoblast-like cells on substrates with a matrix stiffness of 25-40 kPa. In addition, the current mineralized CG scaffold can be compressed between the thumb and forefinger (in specimens of about 6-8 mm diameters, typical of that used surgically). Therefore it would be beneficial to improve the mechanical properties of the current mineralized CG scaffold.

As described by cellular solids models, the mechanical properties of the foam (or scaffolds) depend on the relative density of the foam and the mechanical properties of the solid the foam is made from. In this study we attempt to increase the mechanical properties of the mineralized CG scaffold by increasing the solid mechanical properties using a higher mineral content scaffold. We fabricate mineralized CG scaffolds with varying mineral contents via the triple co-precipitation method and characterize the microstructure as well as the mechanical properties. The mechanical properties of these mineralized scaffolds are discussed in light of the cellular solids model for porous open cell foams. The mechanical properties were found to be less than those of scaffolds made by previous techniques, as well as those predicted by theoretical models, suggesting that their properties could be improved. In the future, we plan to modify further the process used to make our scaffolds in order to improve their mechanical properties [95].

2.2 Materials and methods

Fabrication of the MCG scaffolds

MCG scaffolds were fabricated using microfibrillar, type I collagen isolated from bovine tendon (Integra LifeSciences, Plainsboro, NJ), chondroitin-6-sulfate isolated from shark cartilage (Sigma-Aldrich Chemical Co., St. Louis, MO), phosphoric acid (H_3PO_4) (EMD Chemicals Inc., Gibbstown, NJ), calcium nitrate ($Ca(NO_3)_2.4H_2O$) and calcium hydroxide ($Ca(OH)_2$) (Sigma-Aldrich Chemical Co., St. Louis, MO). MCG slurries with varying mineral content (50% and 75% by weight) and same overall density (0.042 g mL^{-1}) were prepared using the triple co-precipitation method described elsewhere [69, 70, 72, 74-76, 110]. Briefly, the collagen was mixed with H_3PO_4 solution at 15,000 rpm at room temperature in an overhead blender (IKA works Inc., Wilmington, NC) for 60 minutes. Glycosaminoglycan was added to the collagen-H_3PO_4 mix using a peristaltic pump (Manostat, New York, NY) and mixed for another 60 minutes at 15,000 rpm. Dry-mixed $Ca(NO_3)_2.4H_2O$ and $Ca(OH)_2$ were added to the collagen-glycosaminoglycan-H_3PO_4 solution and mixed for additional 15 minutes at 15,000 rpm. The slurry was poured into polysulfone molds (McMaster Carr Supplies, Dayton NJ) with dimensions of 12cm x 3cm x 1cm (x, y and z-axis respectively), placed in a freeze-drier at room temperature, and then freeze-dried as described elsewhere [23, 66, 68, 102, 111]. Briefly, the slurry was cooled down to -20°C at a cooling rate of 0.33°C min^{-1} and kept at that temperature for 4 hr for the slurry to completely freeze. Heat transfer was primarily in the through-thickness or z direction. The frozen slurry was then sublimated at 25°C under vacuum for 36 hr to obtain the dry scaffold. A schematic of the scaffold fabrication process is shown in Figure 2.1.

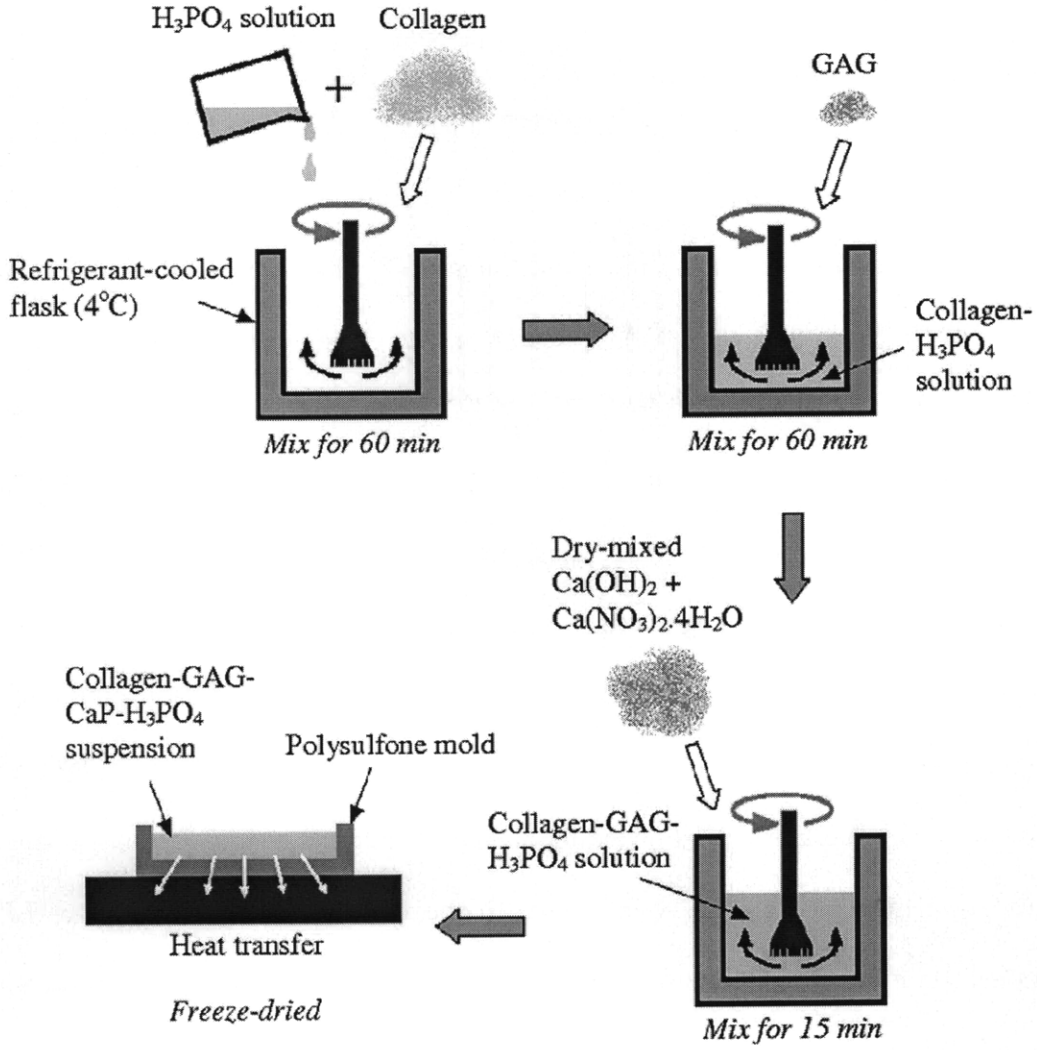

Figure 2.1. Schematic of scaffold fabrication via triple co-precipitation method followed by freeze drying [103].

Crosslinking of the MCG scaffold

Two techniques were used to cross-link the scaffolds: (1) dehydrothermal treatment (DHT) and (2) 1-ethyl-3-(3-dimethylaminopropyl) carbodimide treatment (EDAC). The parameters for the DHT treatment were guided by previous work on CG scaffolds [17, 22, 69, 76, 110]. Briefly, the freeze-dried scaffold was placed under vacuum (50 mTorr)

at a temperature of 105°C for 24 hr. The EDAC process was carried out on the scaffolds according to previously described methods [69, 74, 76, 110]. A 5:2:1 ratio of EDAC:NHS:COOH was used for the current study. Briefly, the scaffolds were hydrated in deionized water for ~15 min followed by mixing the required amount of EDAC/NHS solution into the deionized water and maintaining the scaffold in this solution for ~1 hr. Samples were prepared and tested in the dry state as well as hydrated state (soaked in 10% PBS solution for at least 12 hr before testing). Six types of samples were prepared: (1) NX-DRY: Non-cross-linked, dry scaffold, (2) DHT-DRY: Dehydrothermal treatment, dry scaffold, (3) EDAC-DRY: EDAC cross-linked followed by drying via freeze-drying, (4) NX-HYD: Non-cross-linked, hydrated, (5) DHT-HYD: Dehydrothermal, hydrated, and (6) EDAC-HYD: EDAC cross-linked, hydrated.

Microstructural characterization of the MCG scaffolds

Relative density was calculated from the dry densities of collagen, brushite ($CaHPO_4.2H_2O$) and monetite ($CaHPO_4$) according to equation (2.1):

$$Relative\ density = \rho^* \left(\frac{x_{coll}}{\rho_{coll}} + \frac{x_{brushite}}{\rho_{brushite}} + \frac{x_{monetite}}{\rho_{monetite}} \right) \tag{2.1}$$

where x_{coll}, $x_{brushite}$ and $x_{monetite}$ are the weight fractions of collagen, brushite and monetite in the scaffold material (note that $x_{coll} + x_{brushite} + x_{monetite} = 1$), ρ_{coll} (~1.3 g cm^{-3}) [22, 116], $\rho_{brushite}$ (~2.33 g cm^{-3}) [117] and $\rho_{monetite}$ (~2.93 g cm^{-3}) [118] are the densities of dry collagen, dry brushite and dry monetite and ρ^* is the density of the dry scaffolds. The weight fractions of brushite, monetite and collagen were determined using X-ray diffraction as described below. The contribution of glycosaminoglycan was not

considered, as the amount of glycosaminoglycan was much less than that of the other constituents.

The mean pore diameter, *D*, on different planes (yz, xz and xy) was measured using the mean intercept method (*D* for a particular plane is the average of the major and minor axes of the best-fit ellipse on that plane) [66]; the ratio of the minor to the major axes of the best-fit ellipse gives the pore anisotropy ratio, *R*, on that plane [66]. Briefly, rectangular specimens taken from five different locations were cut perpendicular to the three axes (corresponding to the three different planes as described above) and were embedded in glycolmythacrylate (Polysciences Inc., Warrington, PA). The embedded specimens were cut into 5 μm-thick sections at various depths using a Leica RM2165 microtome (Mannheim, Germany). The sectioned films were stained with Aniline-Blue (Polysciences Inc., Warrington, PA) and observed under an inverted optical microscope (Nikon Optiphot, Japan) at 40x magnification. Images were obtained using a CCD color video camera (Optronics Engineering, Inc., Goleta, GA), and image analysis was conducted using Scion Image analysis software (Scion Corporation, Frederick, MD).

Semi-quantitative and qualitative analyses of the constituent mineral phases in the slurry as well as the dry scaffolds were done using X-ray diffraction (XRD). Semi-quantitative analysis of the weight fractions of brushite and monetite was conducted using the reference-intensity-ratio method (with ~10% accuracy). Direct comparison between the highest peak intensity of the mix phase and the highest peak intensity produced by the pure phases was used to predict the weight fraction of different phases [119, 120]. The slurries were mounted inside a silicate glass tube of 0.5 mm diameter and 0.001 mm

thickness and the dry scaffolds were mounted on an aluminum holder by manually compressing the scaffold materials. For the slurry analysis, a D8 Discover XRD machine (Bruker AXS, Madison, WI) was used. The X-ray intersected the slurry-filled tube in the horizontal plane and the tube was oscillated in the vertical direction in order to scan a large amount of the slurry. The dry scaffold specimens were analyzed using the X'Pert PRO MPD XRD machine (PANalytical, Natick, MA). An incidence angle range of 5^{o}-75^{o} was used, with a step size of 0.0167^{0} and a dwell time of 36.83 s/step. For all scans, Cu Kα radiation was used, and XRD peak analysis was conducted using MDI Jade 7 software (Materials Data, Inc, Livermore, CA).

Scanning electron microscopy (Leo VP438 SEM Leo Electron Microscopy Inc., Thornwood, NY) was used to study the pore structure of the scaffolds. Cylindrical specimens of 5 mm diameter were cut at random locations in the scaffolds using biopsy punches (Miltex Inc., York, PA). Specimens were mounted on an aluminum holder; the specimens were not gold coated. To study the mineral distribution through the wall thickness, specimens were embedded in resin (similar to the specimen preparation for the pore size measurement as described above) and 5 μm-thick sections were sliced out. The backscattered electron detector was used under variable pressure mode to obtain the images. Elemental analysis was done using energy dispersive X-ray analysis (EDAX) in order to identify the calcium and phosphorous distributions.

Microtomography (Scanco USA, Inc., Southeastern, PA) was used to analyze the three-dimensional calcium phase distribution in the scaffolds. Rectangular specimens of 1 cm x 1 cm x 1 cm were cut from the scaffolds perpendicular to the three axes and placed inside

a glass tube. Cross-sectional images (with resolution 1024 x 1024 pixel) were acquired at different depths (seven images at an interval of 125 μm along the axis) for each of the specimens.

Mechanical characterization of the MCG scaffolds

Compressive stress-strain curves for the scaffolds were measured using a Zwick/Roell Z2.5 static materials tester (Zwick GmbH & Co., Ulm, Germany). Cylindrical specimens, 5 mm in diameter and 3-6 mm thick, were cut at random locations in the scaffold along the three axes using biopsy punches (Miltex Inc., York, PA). All of the specimens were compressed at a uniform strain rate of 0.001 sec^{-1} up to a maximum strain of 0.75. Poisson's ratio, v, of the dry scaffolds was measured by capturing images of the compressed specimen within the linear elastic regime of the stress-strain response. Images were acquired at a time interval of 0.2 s using a high-speed CCD camera (Retiga 1300, QImaging corp., Canada) with a 200 mm lens (Nikon, Japan). Poisson's ratio (the negative ratio of lateral/applied strain) was measured from the images using the software analysis package-Vic 2D (Correlated solutions, West Columbia, SC).

The Young's modulus of the solid comprising the scaffold, E_S, was measured via bending of individual scaffold struts using an atomic force microscope (3DMFP, Asylum Research, Santa Barbara, CA). This is an established method to measure the Young's modulus of microscale and nanoscale fibers [121-123]. E_s was measured for both the 50% and 75% by weight NX MCG scaffolds. Rectangular beams were cut from the pore walls of the scaffold using microsurgical forceps and a scalpel under an inverted optical microscope. The length of the beams, L_{max}, varied from 40-120 μm, the width, b, varied

from 25-90 μm and depth, h, varied from 3-12μm as measured via optical microscopy (Nikon Optiphot, Japan). One end of each beam was bonded to a rigid support with cyanoacrylate, with creating a cantilevered beam of length L from the support point (Figure 2.2). The bending test was carried out using an AC160TS cantilever (Olympus, Tokyo, Japan) of stiffness = 48.42 N m^{-1}, as measured via thermal power spectral density [121]. The force-deflection relation (F-Δ) of the beam is given by:

$$\frac{F}{\Delta} = \frac{3E_s I}{L^3} \tag{2.2}$$

where $I = bh^3/12$.

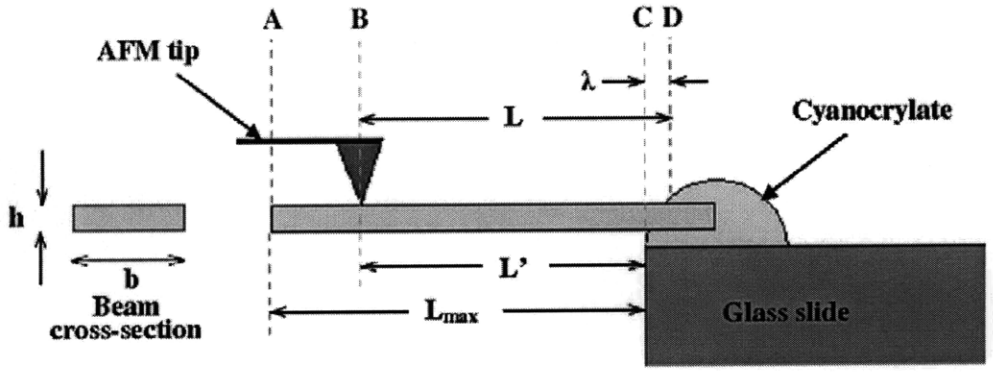

Figure 2.2. Schematic of the experimental set up for the AFM bending test to determine modulus of the pore walls, E_S. Point A is the free end of the beam, point B is the loading point on the beam, point C is the reference point on the glass slide, and point D is the support point of the beam [103].

L could not be measured accurately from optical images of the beam setup because the support point was not well-defined (Figure 2.3), but it was estimated by loading the cantilever at various points along the length of each strut (five to seven points) and measuring F vs. Δ for each loading point. The length between the loading point and the support point, L, was represented as $(L'+\lambda)$ where L' is the measured distance between the

loading point and a reference point on the support (the edge of the glass slide as shown in Figure 2.2) and λ is the distance between the support point and the reference point (note that λ is an unknown quantity). A typical F-Δ response is shown in Figure 2.4a. A schematic diagram of the bending experiment is shown in the top-right of the figure. For each plot, F/Δ was measured from the slope of the initial retraction curve (as shown in Figure 2.4a) to isolate the elastic response [121, 122]. A graph of L' versus $(\Delta/F)^{1/3}$ for the tests with the loading point at different points along the length of the beam was constructed (Figure 2.4b). A straight line was fit to these points with $R^2 > 0.95$ indicated that the beams were of uniform moment of inertia I (= $bh^3/12$). The slope of this line is $(3E_sI)^{1/3}$ and the intercept is $-\lambda$ (see Eq. (2.2)). As I is known, E_s can thus be calculated. Five strut sections from each of the 50% and 75% by weight MCG scaffolds were tested in this manner.

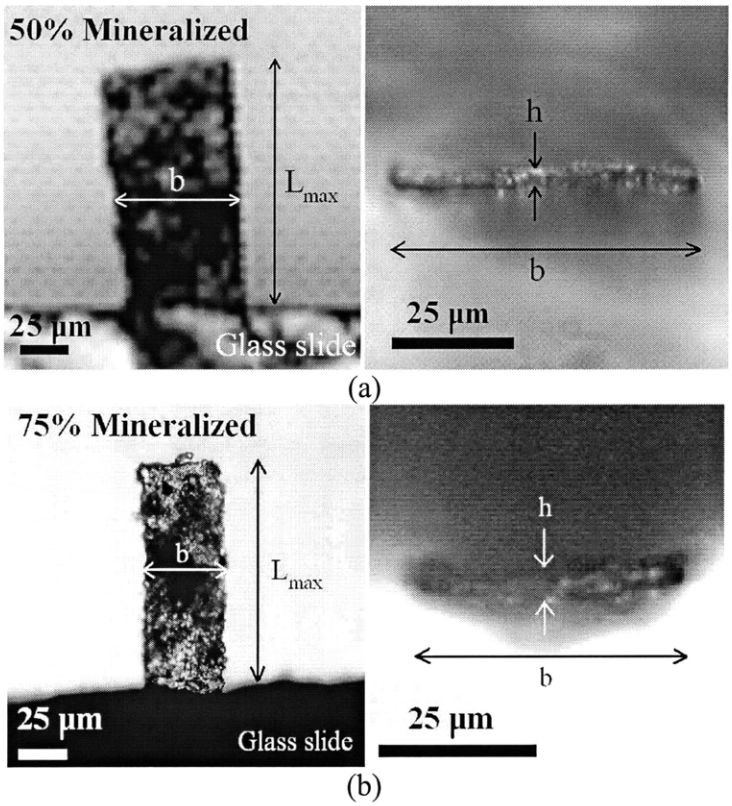

Figure 2.3. Longitudinal and cross sectional views of individual beams cut out of the MCG scaffolds, used in measuring Es. (a) 50% by weight MCG scaffold (b) 75% by weight MCG scaffold [103].

The rupture strength of the solid, σ_{fs}, was estimated via nanoindentation using a Hysitron triboindenter (Hysitron, Inc., Minneapolis, MN) [124-126]. Samples were cut from the walls of the scaffold using microsurgical forceps and a scalpel under a bottoms-up optical microscope. The samples were bonded to a glass slide using cyanoacrylate and indented using a Berkovich indenter (Hysitron, Inc., Minneapolis, MN).

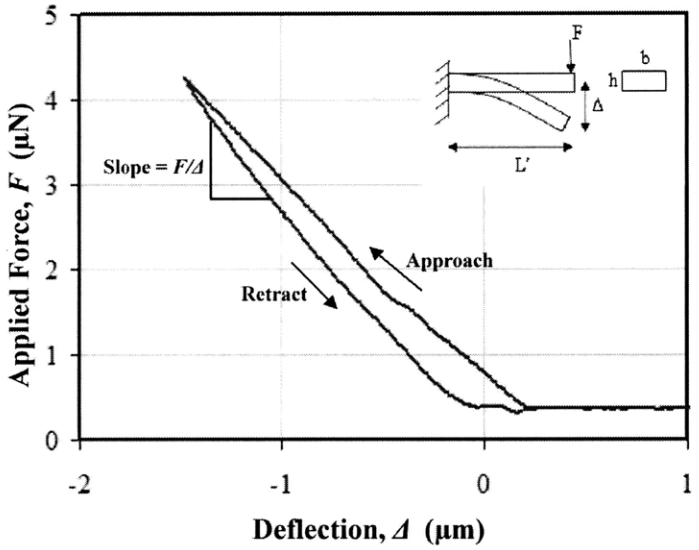

(a)

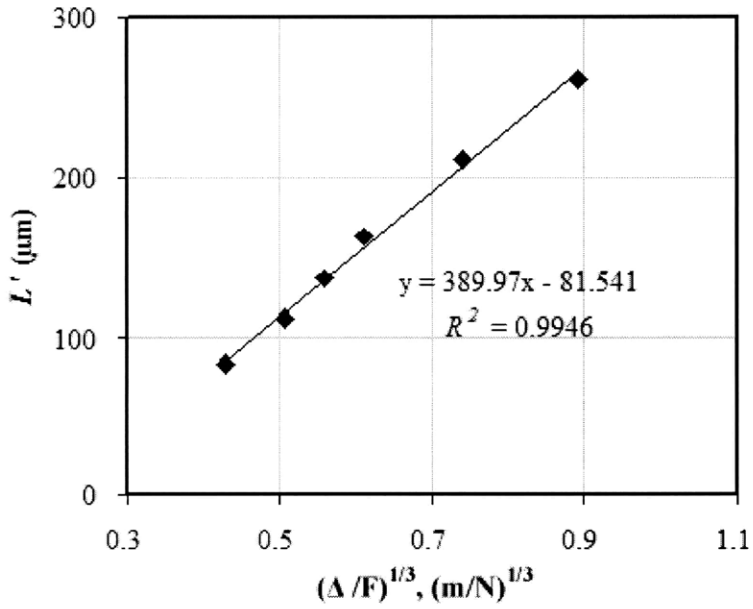

(b)

Figure 2.4. (a) A sample bending force-deflection plot for a single beam of the 50 wt.% MCG is scaffold is shown. Similar plots were obtained for loading at different points along the length of the strut, L_{max}. From the L' vs $(\Delta/F)^{1/3}$ plot, the modulus of the strut, E_s, was calculated (Eq (2.2)). (b) Plot of L' vs $(\Delta/F)^{1/3}$ for 50 wt.% MCG beam is shown. Slope of this line it is equal to $(3E_sI)^{1/3}$. Knowing the dimensions of the beam, ($I = bh^3/12$), E_s can be calculated [103].

The load function consisted of three steps: (1) loading up to 75 μN at a rate of 7.5 μN/s, (2) saturating at 75 μN for 5 s and (3) unloading to zero load at a rate of 7.5 μN/s. Twenty-five indents were conducted per sample and at least four samples were tested for each of the 50% and 75% by weight NX MCG scaffolds. A typical load-displacement curve for a 50% by weight MCG scffold in the NX-DRY state is shown in Figure 2.5 (those for the 75% by weight MCG scaffold were similar).

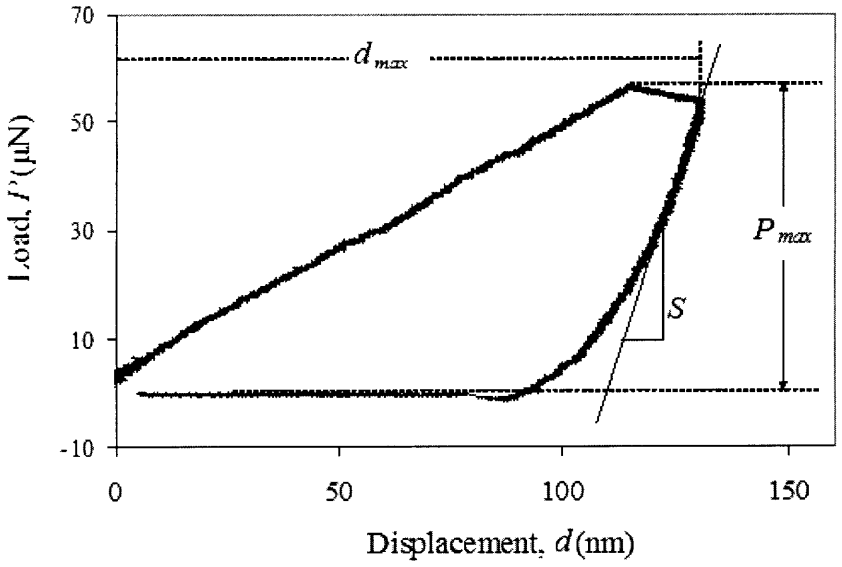

Figure 2.5. A sample load–displacement plot for the 50% wt.% MCG scaffold wall is shown. Similar plots were obtained for the 75% wt.% MCG scaffold. Note that these nanoindentation experiments were conducted in open-loop load control, resulting in partial dissipation of the requested applied load via the transducer of this indenter. Thus, the maximum load exerted on the scaffold pore wall solid material was less than the requested magnitude of 75 μN. The dwell period at maximum load exhibits a slight decrease in load due to this open-loop feedback, as well as creep, but is not indicative of rupture or fracture of the mineralized pore wall. For this indenter geometry, indentation depths of 100 nm sample a contact area exceeding 0.2 μm^2 and a subsurface volume exceeding 0.04 μm^3, sufficient for at least some indentations to sample both the mineral and the polymer phases of the pore wall [103].

Rupture strength, σ_{fs}, was approximated from the calculated hardness, H, or mean pressure at maximum load as:

$$\sigma_{fs} \sim \sigma_{ys} = \frac{H}{3} = \frac{P_{\max}}{3A_c} \tag{2.3}$$

where σ_{ys} is yield strength, P_{max} is the maximum indentation load and A_c is the projected area of contact. Note that this assumption of equivalence between the compressive yield strength and rupture strength of the mineralized pore wall material will tend to underestimate the actual rupture strength of the material, as the rupture strength will exceed the yield strength if the mineralized pore wall material effectively strain hardens upon yielding. Thus, the approximation in Eq. (2.3) should be considered a lower limit of the solid material rupture strength. Fused silica was used to calculate the machine compliance and the projected area of contact as a function of the contact depth. From the same load-displacement response, the elastic modulus of the sample, $E_s^{NX\text{-}DRY}$ was estimated from A_c and the slope of the initial portion of the unloading curve, S (Figure 2.5), according to the method of Oliver and Pharr [124].

Cellular solids model of the MCG scaffold

The mechanical properties of cellular solids depend on relative density and the properties of the solid of which the cellular solid is made (such as density, ρ_S, Young's modulus, E_s, rupture strength, σ_{fs}) and the cell geometry (e.g., open- or closed-cells) [17, 95, 101]. Simple relationships between overall foam properties (such as Young's modulus, E^*, and strength, σ^*), and the relative density and solid cell wall properties can be derived using

dimensional analysis [95, 101]. Key relationships for open-cell foams that are relevant for mechanical characterization of the scaffolds are given below:

$$\frac{E^*}{E_s} = \left(\frac{\rho^*}{\rho_s}\right)^2 \tag{2.4}$$

$$\frac{\sigma^*}{\sigma_{fs}} = 0.2\left(\frac{\rho^*}{\rho_s}\right)^{\frac{3}{2}} \tag{2.5}$$

Statistical analysis

One-way analysis of variance (ANOVA) and Fisher's protected least significant difference (Fisher's PLSD) methods were used to determine statistical significance between different sets of data and pair wise data sets, respectively. A probability value of 95% (p <0.05) was used to determine the significance. All the measurements are reported as mean ± standard deviation. The symbols *, **, and *** indicates statistically significantly different results.

2.3 Results

Microstructural characterization

The experimentally measured overall scaffold densities (ρ^*) for the 50% and 75% by weight MCG scaffolds were 0.063 ± 0.0015 g cm^{-3} and 0.06±0.0034 g cm^{-3}, respectively. The densities are statistically significantly different (p = 0.039) even though the target slurry densities were the same (0.042 g mL^{-1}). The difference arises from the fact that some of the calcium phosphate phase adhered to the surface of the beaker while mixing. The relative densities can be calculated using Eq (2.1). For the 50% scaffold, x_{coll} = 0.5,

$x_{brushite} = 0.485$ and $x_{monetite} = 0.015$ while for the 75% scaffold, $x_{coll} = 0.25$, $x_{brushite} = 0.503$ and $x_{monetite} = 0.248$, these results are described in further detail below. Relative densities for 50% and 75% by weight MCG scaffolds are calculated to be 0.038±0.001 and 0.030±0.002, respectively. The 75% scaffold was observed via SEM to have a bilayer structure with small pores in the top layer, closer to the air side during freeze-drying, and larger pores in the bottom layer, closer to the cooling plate on the base. The densities of these layers were measured separately by sectioning the scaffold at the interface and punching out specimens from both the layers. The relative densities were 0.032±0.003 and 0.024±0.002 for the top and bottom layers respectively. The characteristics of the bilayer are described in more detail below.

Optical images of an embedded specimen perpendicular and parallel to the *z*-axis, through the thickness of the scaffold sheet, are shown in Figure 2.6. The 50% by weight MCG scaffold exhibited a uniform microstructure throughout the scaffold, with a roughly uniform pore size and interconnected walls throughout. The 75% by weight MCG scaffold exhibited a bimodal pore size distribution, with smaller pores and interconnected walls in the top zone and larger pores and disconnected walls in the bottom zone. The mean pore diameter, D, and anisotropy ratios, R, on the three different planes are listed in Table 2.1; for the 75% scaffold, measurements for the top and bottom layers are reported separately. R on different planes were greater than 0.92 and D on different planes were similar; the pores are roughly equiaxed for both scaffolds. The average pore diameter was calculated by averaging all the values (on different planes). The average pore diameter for the 50% scaffold was 202±25 μm. The average pore diameters of the 75% scaffold

for the top and bottom parts of the scaffold were 227±31 μm and 343±38 μm, respectively. These values were statistically significantly different ($p < 0.05$).

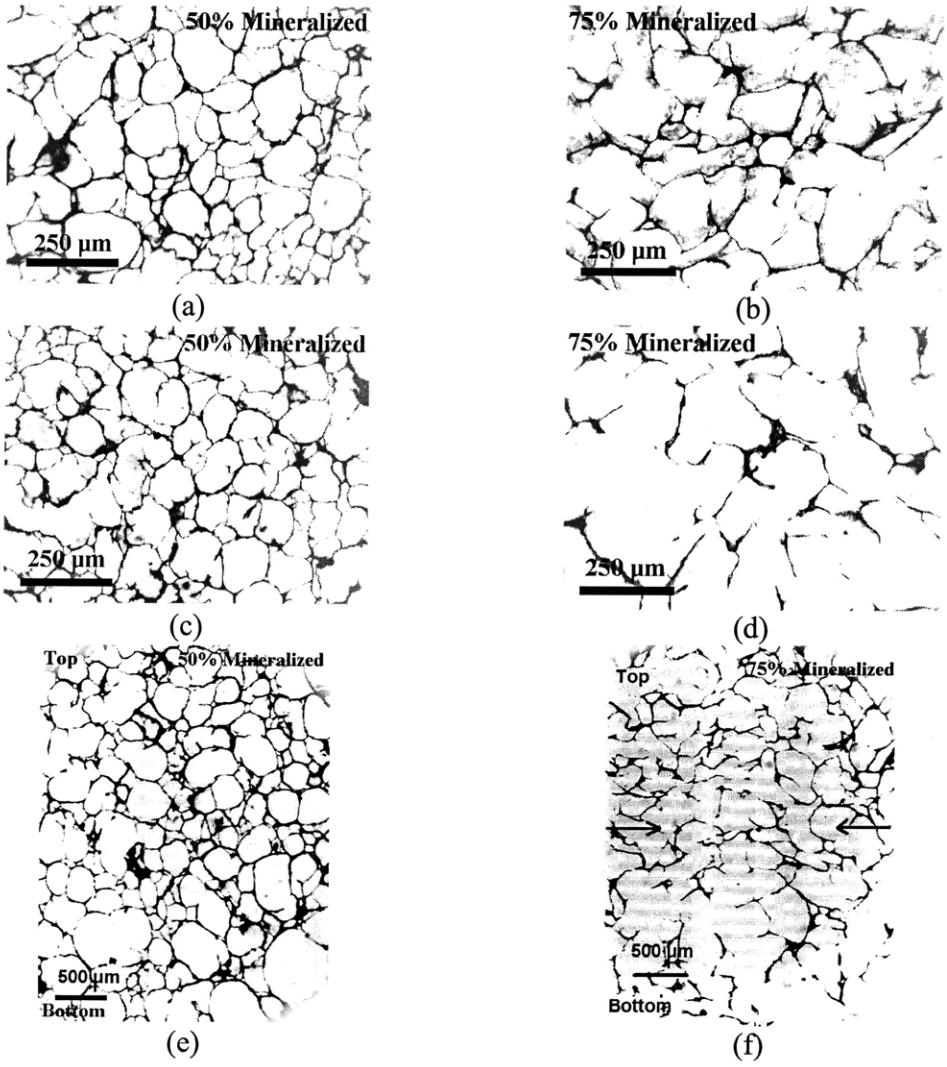

Figure 2.6. Optical micrographs of embedded MCG scaffolds with planes perpendicular to the z-axis. (a) and (c) 50% by weight scaffold and (b) and (d) 75% by weight scaffold, taken at different depths along the z-axis. (e) and (f) entire cross-section of plane parallel to the z-axis for the 50% and 75% by weight MCG scaffolds respectively, showing uniform pore size distribution for the 50% scaffold and bimodal pore size distribution for the 75% scaffold [103].

Figure 2.7a shows the XRD plots for the 50% and 75% by weight MCG slurries. The straight lines represent brushite peaks. It is apparent that both slurries exhibited 100% brushite as the only mineral phase. Figure 2.7b shows the XRD plots for the NX-DRY MCG scaffolds. Based on the reference intensity ratio method as described above, the 50% scaffold comprised 97 wt% brushite and 3 wt% monetite as the crystalline phases, while the 75% scaffold comprised 67 wt% brushite and 33 wt% monetite as the crystalline phases.

Scaffold	*Plane*	*D (μm)*	*R*
	yz	216 ± 26.0*	0.972 ± 0.023
50%-NX	xz	194 ± 21.0	0.966 ± 0.039
	xy	196 ± 23.1	0.957 ± 0.035
75%-NX	yz-top	214 ± 26.8	0.955 ± 0.040
	xz-top	242 ± 17.6	0.939 ± 0.049
	xy-top	224 ± 42.6	0.922 ± 0.075
	yz-bottom	344 ± 42.0	0.929 ± 0.053
	xz-bottom	342 ± 42.2	0.959 ± 0.049
	xy-bottom	343 ± 31.9	0.963 ± 0.042

* Indicates statistically different value

Table 2.1. Pore size measurements for the 50% and 75% by weight NX-DRY MCG scaffolds [103].

SEM micrographs of the 50% and 75% by weight MCG scaffolds (images taken of the plane perpendicular to the z-axis) are shown in Figure 2.8. The scaffolds exhibit a homogeneous distribution of mixed open and closed cell microstructure with interconnected pores (Figure 2.8a and b). Unlike unmineralized CG scaffolds [17, 66, 68], MCG scaffolds exhibited pore walls as well as thin struts.

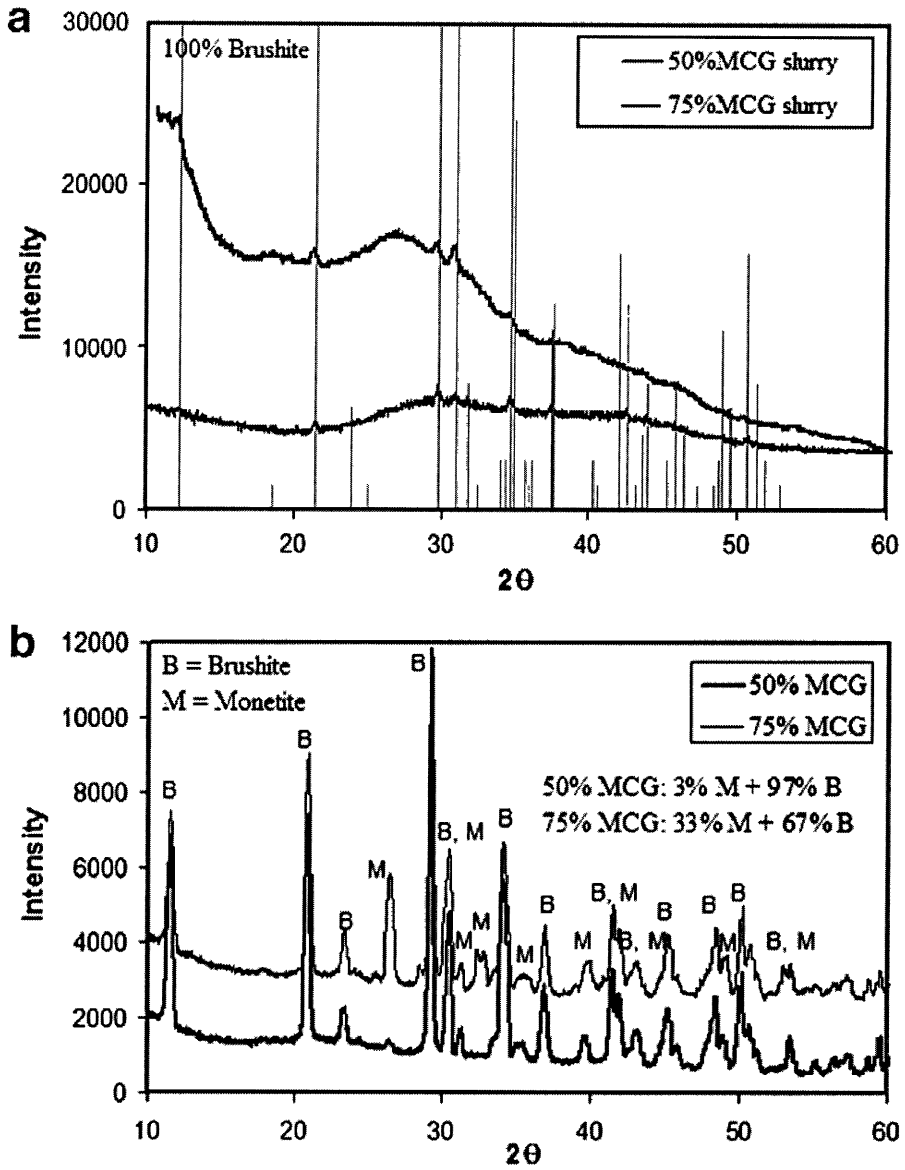

Figure 2.7. (a) X-ray diffraction plots for for the 50% and 75% by weight MCG slurries are compared in this figure. The vertical lines represent brushite peaks. (b) X-ray diffraction plots for the dry 50% and 75% by weight MCG scaffolds are compared in this figure. The 50% scaffold has mostly brushite while the 75% scaffold has a significant amount of monetite along with brushite [103].

EDAX analysis showed that the white particles through the thickness of these walls (Figure 2.8c and d) are calcium- and phosphorous- rich particles. As described above, XRD results confirmed these particles to be either brushite or monetite. The more highly

mineralized scaffold had a denser packing of calcium phosphate. The denser calcium phosphate packing in the 75% by weight MCG scaffold causes a large variation in the wall thickness (Figure 2.8c and d). Mineral phase particle size ranged from 100s nm to μm with a mode cross-sectional area of ~1.3 μm^2 (calculated from Figure 2.8c and d).

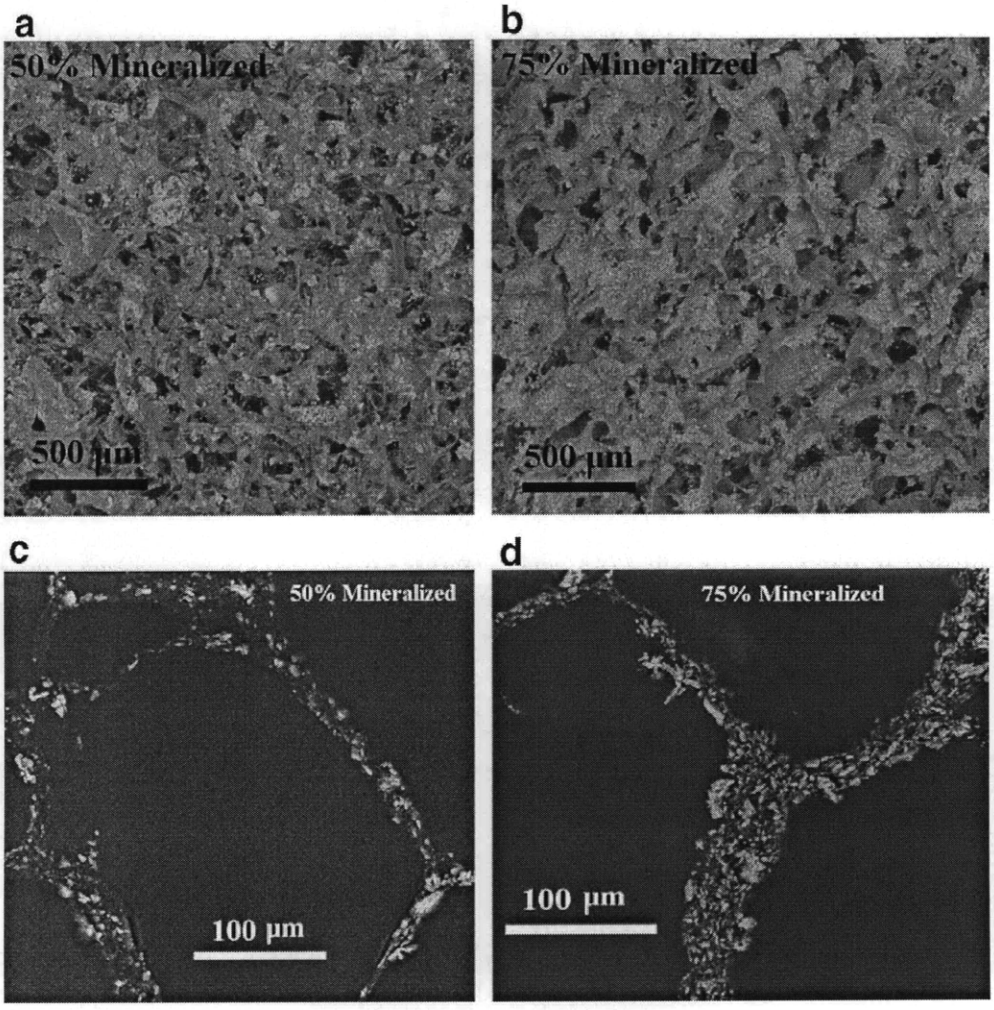

Figure 2.8. (a, b) SEM images for the 50% and 75% by weight MCG scaffolds measured on the 5 mm dia punched out of the scaffolds. (c, d) Mineral distribution through the thickness of the pore walls measured on the 5 μm thick resin embedded samples [103].

Microtomographic images for the 50% and the 75% by weight MCG scaffolds are shown in Figure 2.9, indicating planes perpendicular to the z-axis at two specific depths. Due to the higher density of the calcium-phosphate phases compared to collagen, microtomographic images had different contrast than the SEM micrographs: calcium-phosphate phases correspond to dark regions and collagen corresponds to lighter regions. Because of the non-uniform contrast and beam hardening, these images are unsuitable for quantitative analysis (such as pore diameter calculations) [127]. However, by thresholding the images, we can qualitatively determine the calcium-phosphate distribution in the scaffolds. Microtomographic images confirmed that the mineral phases were distributed homogeneously throughout the walls and struts of the scaffolds. These results also confirm that the 50% scaffold has a uniform pore size throughout the entire scaffold while the 75% scaffold has a bilayer structure with two distinct pore sizes. Also, it is clear that the mineral phases are distributed homogeneously throughout the walls and struts of the scaffolds.

The 50% scaffold has a uniform pore size throughout the entire scaffold. However, both SEM and microtomographic images of the 75% scaffold indicated a distinct boundary between the top portion of the scaffold, which had smaller pores, and the bottom portion of the scaffold, which had larger pores (Figure 2.10). The boundary between the two zones varied from near the edge of the sample to the center of the sample. SEM and optical micrographs indicated defects such as voids and cracks in the walls and struts of the MCG scaffolds (Figure 2.11a and b), as well as disconnected pore walls and struts

(Figure 2.11c and d). The 75% by weight MCG scaffold exhibited more defect sites than the 50% scaffold.

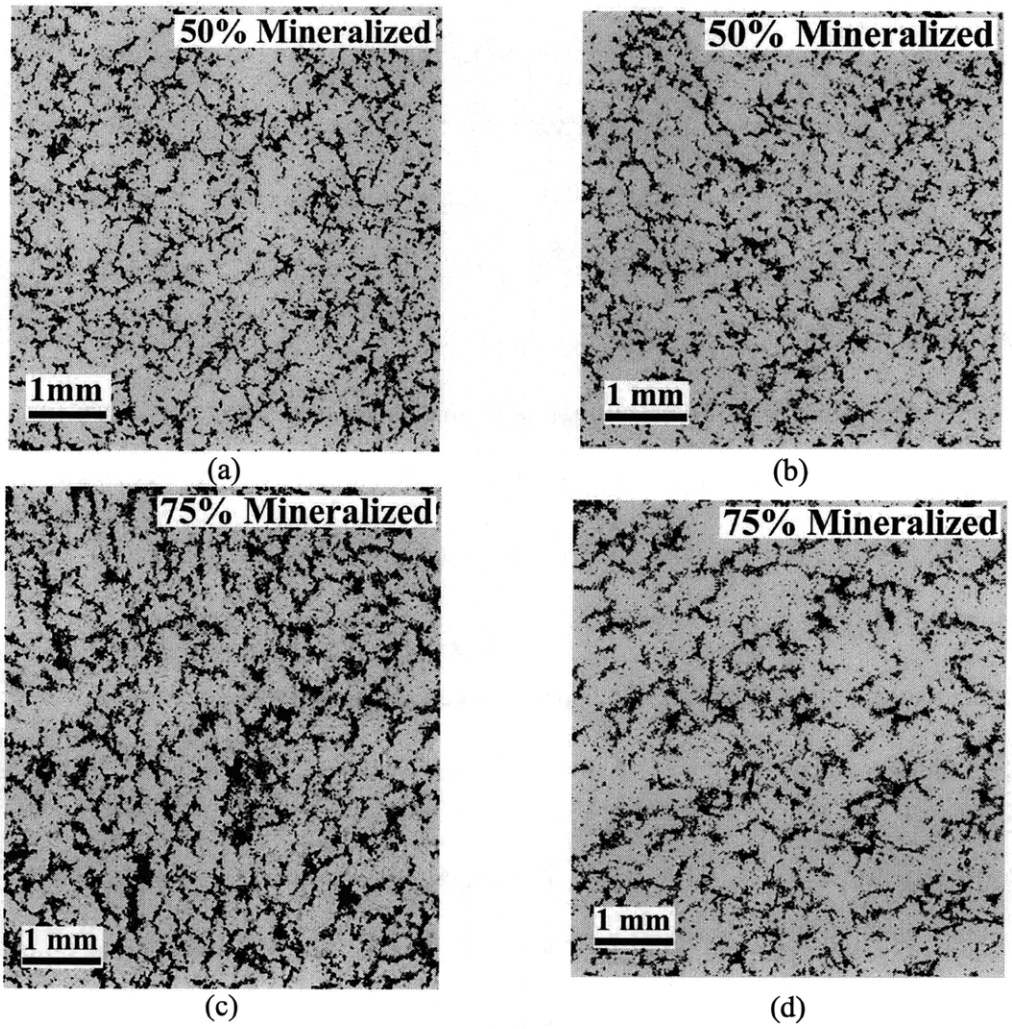

Figure 2.9. (a, b) Micro-CT images for the 50% by weight MCG scaffold taken at two different depths along the z-axis. (c, d) Micro-CT images for the 75% by weight MCG scaffold taken at two different depths along the z-axis [103].

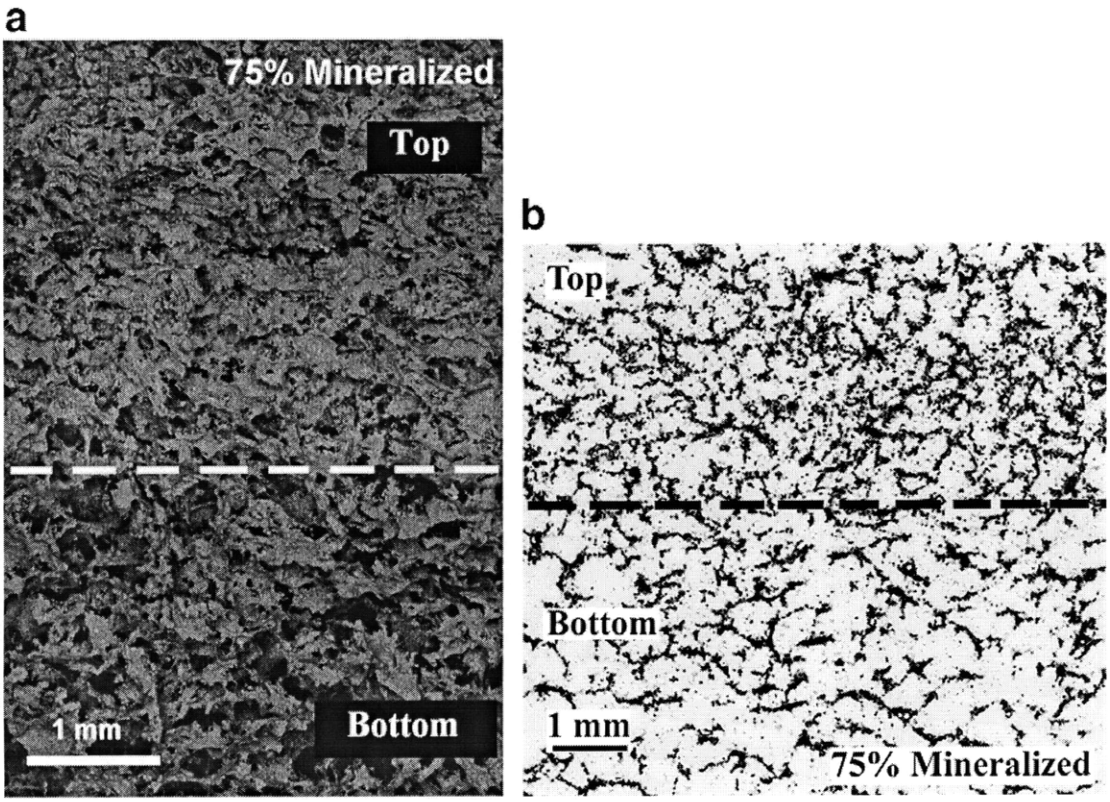

Figure 2.10. Bimodal pore size distribution in the 75% by weight MCG scaffold is demonstrated in (a) the SEM and (b) the micro CT images. The arrows separate the section with smaller pores (top) from that with larger pores (bottom) [103].

Mechanical characterization

A typical compressive stress-strain curve for a 50% by weight MCG scaffold in the dry state is shown in Figure 2.12 (those for the 75% by weight MCG scaffold were similar). Distinct linear elastic, collapse plateau and densification regimes were observed. Elastic modulus (E^*), collapse strength and strain (σ^* and ε^* respectively) and collapse modulus ($\Delta\sigma/\Delta\varepsilon$) are measured from the stress-strain curve. E^* is the slope of the linear elastic regime, $\Delta\sigma/\Delta\varepsilon$ is the slope of the collapse regime, σ^* and ε^* are the point of transition from linear to the collapse regime (determined from the intersection of the E^* and $\Delta\sigma/\Delta\varepsilon$

regression lines). Curves of similar shape, but lower modulus and strength were obtained for the hydrated states of the scaffolds.

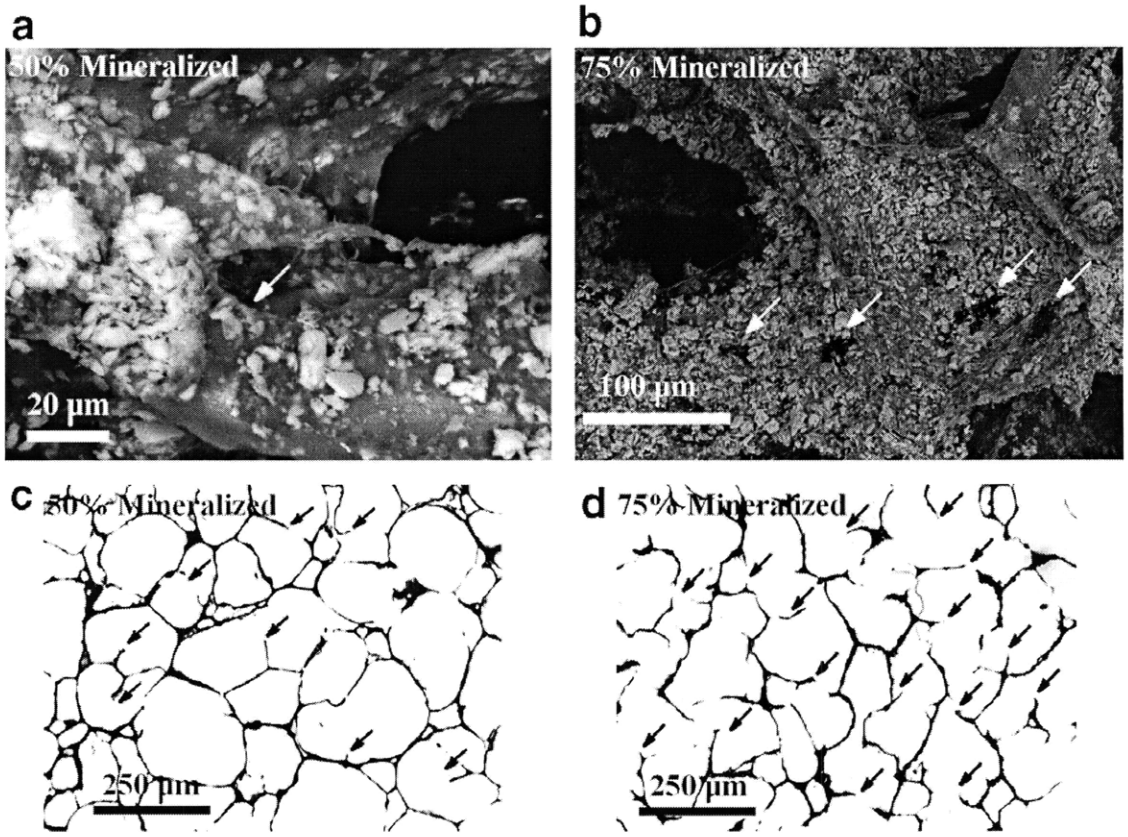

Figure 2.11. (a, b) SEM images of the 50% and 75% by weight MCG scaffolds showing voids on the pore walls. (c, d) Optical images of the 50% and 75% by weight MCG scaffolds showing disconnected walls and struts [103].

The values of E^*, σ^*, ε^* and $\Delta\sigma/\Delta\varepsilon$ for loading along the three axes for the 50% and 75% by weight MCG scaffolds in the NX-DRY state are listed in Table 2.2. The Young's moduli of the 50% scaffold are typically about twice those of the 75% scaffold and the strength of the 50% scaffold is typically about thrice those of the 75% scaffold. The 75% scaffold has a lower E^* and σ^* in the z direction due in part to the two layers of different

densities through the height of the scaffold. For both scaffolds ε^* is on the order of 10-15%. Collapse moduli of the 50% scaffold are higher than those of the 75% scaffold.

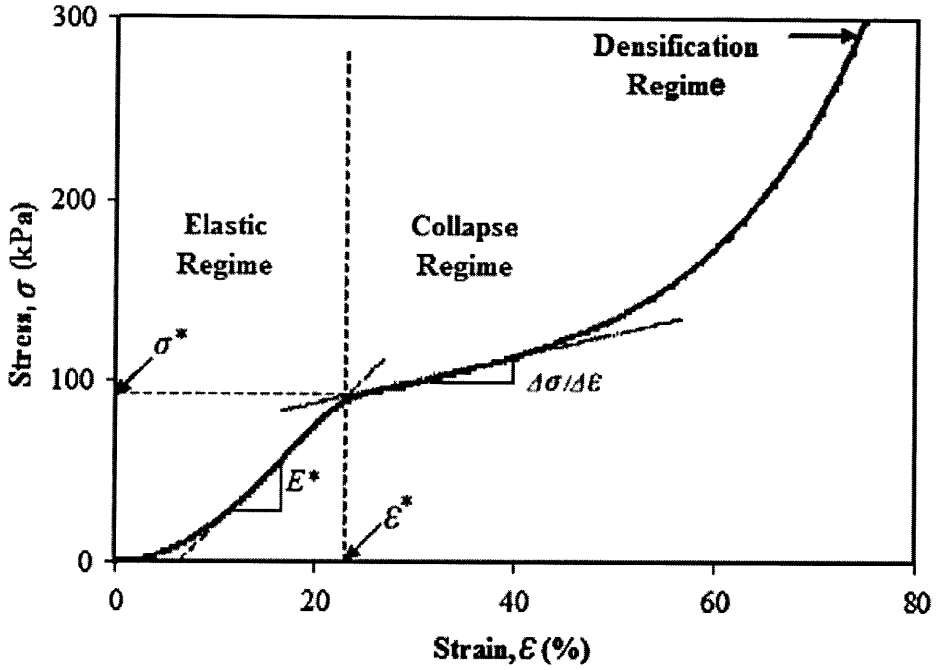

Figure 2.12. A typical compressive stress-strain curve for a 50% by weight NX-DRY MCG scaffold. The slope in the linear elastic regime is the modulus of the scaffold (E*), the slope in the collapse regime is the collapse modulus ($\Delta\sigma/\Delta\varepsilon$) and the point of intersection of the regression lines for modulus and collapse modulus are characterized by collapse strength (σ^*) and collapse strain (ε^*). The 75% by weight MCG scaffold had a similar stress-strain curve [103].

The values of E^*, σ^*, ε^* and $\Delta\sigma/\Delta\varepsilon$ in the z-direction for scaffolds with the different cross-linking treatments are listed in Table 2.2. The properties for the hydrated 75% by weight MCG scaffold could not be determined, as the slope difference between the linear elastic regime and the collapse plateau regime was negligible. The specific cross-linking treatments had no statistically significant effect on any of the properties (p>0.05) for both scaffolds in the dry state, with the exception of the DHT treatment on the 75% mineralized scaffold. As expected, the hydrated state exhibits a much lower E^*, σ^* and

$\Delta\sigma/\Delta\varepsilon$ than that of the dry state for the 50% scaffolds. In the hydrated state, DHT and EDAC crosslinking increase the E^*, σ^*, and $\Delta\sigma/\Delta\varepsilon$ over that of the non crosslinked scaffold by 1.5 and 5 times, respectively. There was no statistically significant effect on the collapse strain, ε^*, with the exception of the EDAC crosslinking.

Scaffold	Axis	E^* (kPa)	σ^* (kPa)	ε^* (%)	$\Delta\sigma/\Delta\varepsilon$ (kPa)
Effect of loading direction (dry)					
50% NX-DRY	x	1000 ± 267*	102 ± 9.03*	10.4 ± 2.29	103 ± 41.6
	y	615 ± 146	88 ± 8.69	13.9 ± 3.38	111 ± 35.9
	z	720 ± 215	83 ± 11.2	12.4 ± 3.82	123 ± 37.4
75% NX-DRY	x	403 ± 152	33.8 ± 5.79	9.01 ± 2.78	77.2 ± 20.3
	y	495 ± 119	43.1 ± 9.99*	8.87 ± 1.41	67.4 ± 19.3
	z	204 ± 36.8*	28.4 ± 4.81	13.4 ± 1.06*	112 ± 15.4*
Scaffold	Cross-link	E^* (kPa)	σ^* (kPa)	ε^* (%)	$\Delta\sigma/\Delta\varepsilon$ (kPa)
Effect of cross-linking (dry): tested in the z-direction					
50%	NX-DRY	720 ± 215	83 ± 11.2	12.4 ± 3.82	123 ± 37.4
	DHT-DRY	853 ± 99.0	97.5 ± 11.6	11.4 ± 0.72	158 ± 34.8
	EDAC-DRY	759 ± 230	88.0 ± 14.6	12.5 ± 3.99	139 ± 45.7
75%	NX-DRY	204 ± 36.8	28.4 ± 4.81	13.4 ± 1.06	112 ± 15.4
	DHT-DRY	274 ± 51.6	48.3 ± 18.0*	17.1 ± 3.81*	160 ± 48.6
	EDAC-DRY	230 ± 110	29.8 ± 12.0	13.6 ± 2.84	87.5 ± 73.5
Scaffold	Cross-link	E^* (kPa)	σ^* (kPa)	ε^* (%)	$\Delta\sigma/\Delta\varepsilon$ (kPa)
Effect of cross-linking (hydrated): tested in the z-direction					
50%	NX-HYD	3.86 ± 0.738*	0.341 ± 0.060	9.78 ± 1.90	1.95 ± 0.187*
	DHT-HYD	6.20 ± 1.51**	0.547 ± 0.089	9.60 ± 3.02	3.05 ± 0.392**
	EDAC-HYD	15.20 ± 1.68***	2.080 ± 0.337*	13.30 ± 3.26*	8.54 ± 1.25***
75%	The properties of the scaffolds could not be determined as the slope difference between the linear elastic regime and the collapse plateau regime was negligible. The behavior could not be idealized as that of open-cell foams.				

Note: results are reported as mean ± standard deviation; *, **, and *** denote distinct, statistically significant results via ANOVA.

Table 2.2. Mechanical properties of the 50% and 75% by weight MCG scaffolds determined from the compression tests [103].

For the 75% by weight NX-DRY MCG scaffold, the Young's modulus and collapse strength in the z direction of the top and bottom zones, which are of different pore sizes and densities, were measured separately. The scaffold was cross-sectioned perpendicular to the z-axis at the boundary between the zones (determined by visual inspection) to obtain two separate pieces with the two different pore sizes. Figure 2.13 shows E^* and σ^* for the top and the bottom zones of the 75% NX MCG scaffold along with the overall E^* and σ^*. As expected from a simple lower bound composites model, the overall E^* lies between that of the top and bottom layers.

The Poisson's ratio for the 50% and 75% by weight NX-DRY MCG scaffolds were measured to be 0.02 ± 0.005 and 0.02 ± 0.007 respectively (samples were loaded in the z direction). These are negligible compared to the expected value of ν for open cell foam (i.e., 0.3) [95].

Young's moduli of the solid, $E_s^{NX\text{-}DRY}$, for the 50% and 75% by weight NX-DRY MCG scaffolds were measured to be 9.15±0.983 GPa and 6.31±1.43 GPa, respectively (based on the AFM bending test). $E_s^{NX\text{-}DRY}$ varied from ~7.8 – 10.5 GPa and 4.5 - 7.7 GPa for the 50% and 75% by weight scaffolds, respectively. These results can be linearly extrapolated to the crosslinked and hydrated states, based on the relative difference in E^* for different states (for example, $E_s^{DHT\text{-}DRY} = E_s^{NX\text{-}DRY} \times [E_{DHT\text{-}DRY}^*/E_{NX\text{-}DRY}^*]$ and $E_s^{DHT\text{-}HYD} = E_s^{DHT\text{-}DRY} \times [E_{DHT\text{-}HYD}^*/E_{DHT\text{-}DRY}^*]$) [17].

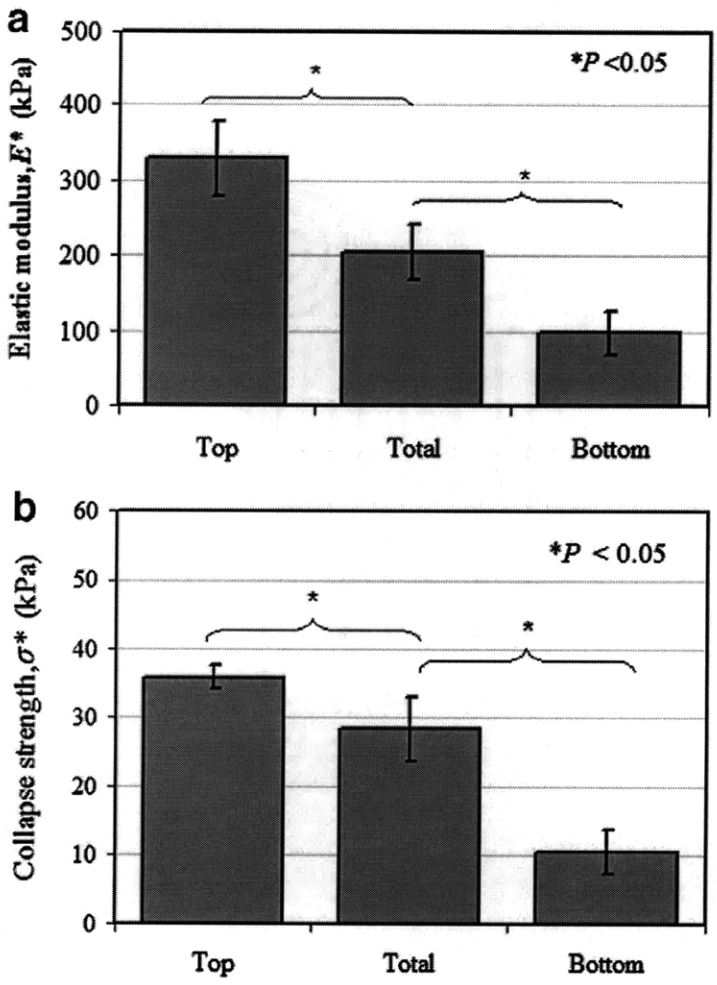

Figure 2.13. Young's modulus (E^*) and cocllapse strength (σ^*) of each of the layers of the 75% by weight NX-DRY MCG scaffolds of differing density and pore size, is compared with the over all modulus and strength of the scaffold. All the modulus and strength values are measured along z-direction (E^*_{Top} = 329 ± 48.9 kPa, E^*_{Bottom} = 98.2 ± 28.5 kPa and E^*_{Total} = 204 ± 36.8 kPa, σ^*_{Top} = 36 ±1.73 kPa, σ^*_{Bottom} = 10.7 ± 3.21 kPa, σ^*_{Total} = 28.4 ± 4.81 kPa) [103].

Measurement of rupture strength of the solid, σ_{fs}, based on nanoindentation, is an approximation to the actual strength of the composite, as the variation in σ_{fs} was much larger depending on the local composition of the point of indentation. As seen in Figure 2.8c and d, the pore walls consisted of CG matrix reinforced with mineral phases. Since the area indented was nanoscale in volume (see Figure 2.5), the extreme values plausibly

corresponded to the mechanical response of the CG matrix phase and the mineral phases. σ_{fs} varied from ~0.5 to 300 MPa and from 30 to 350 MPa for the 50% and 75% by weight NX-DRY MCG scaffolds, respectively. However, for calculations of scaffold mechanical properties based on the cellular solids model, the values of σ_{fs} within this range were chosen from the subset of nanoindentation experiments that predicted the same E_S as that obtained from AFM beam-bending tests. Both the beam-bending experiments and pore-wall-indentation experiment probed the Young's modulus of the solid, E_S; the former approach captures the modulus over a larger volume than is represented by the nanoindented volumes. Thus, we assume that the mineralized composite (volume-averaged) mechanical response is best represented by nanoindented regions of the mineralized pore wall that exhibited the same modulus as that measured via beam-bending. This assumption is supported by the fact that the mode mineral phase cross-sectional area of 1.3 μm^2 exceeds the projected area of contact of these indentations computed from probe geometry and maximum depth (0.24 μm^2). Given the wide mineral phase particle size distribution (Figure 2.8), an array of indentations of this size could sample the stiff particles, the compliant CG pore wall and a composite mixture of these two phases. The solid wall modulus, E_S, measured from the nanoindentation tests, varied from ~13.4 GPa to 19 GPa and from 2 to 25 GPa for the 50% and 75% by weight NX-DRY MCG scaffolds, respectively. As noted above, the range of E_S obtained from the AFM bending test was similar to that obtained from the nanoindentation tests. The resulting strengths of the solid materials making up the scaffold struts, σ_{fs}, were 201 ± 52 MPa and 149 ± 66 MPa for the 50% and 75% by weight MCG NX-DRY scaffolds, respectively. These results can be linearly extrapolated to the cross-linked and hydrated

states, based on the relative difference in σ^* for different states (similar to Young's modulus predictions for different states, as described above).

2.4 Discussion

The pore sizes for both scaffolds were in the range of 200–350 μm, which is optimal for bone growth [20, 37, 128, 129]. For both scaffolds, the mineral phase was distributed throughout the walls, which is an improvement over existing mineralized scaffolds in which the mineral simply coats the outside of the collagen struts [48, 90, 130-132].

There were substantial differences in the microstructure and mechanical properties of the 50% and 75% by weight MCG scaffolds. The 50% scaffold had a higher relative density, as well as a more uniform density and pore size than the 75% scaffold. The walls of the 75% scaffold were more variable in thickness along their length and were less well connected, with ruptures and cracked walls visible in the SEM images, compared with the 50% scaffold.

Bone mineral closely resembles hydroxyapatite, a calcium phosphate. Scaffolds for bone regeneration usually involve some form of calcium phosphate, typically hydroxyapatite [54, 89] or tricalcium phosphate [51, 90]. In our scaffolds, most of the calcium phosphate exists as brushite, which can be converted to octacalcium phosphate and then to apatite by hydrolysis. Monetite, on the other hand, does not convert to octacalcium phosphate [69, 74, 133, 134]. The 50% scaffold was comprised chiefly of brushite (97 wt.%), while the 75% scaffold was comprised of 66 wt.% brushite and 33 wt.% monetite. In the 75% MCG scaffold, some of the brushite in the slurry phase transformed to monetite during

freeze-drying (note that monetite is a dehydrated form of brushite). During this phase change, the by-product (i.e. water) was liberated to the immediate vicinity of the scaffold walls and struts, making this scaffold partially hydrated even after extended sublimation. This was evident from the adhesive nature of the scaffold upon handling. The phase concentration is believed to be due to the higher concentration of H_3PO_4 used in the synthesis of the 75% by weight scaffold. During sublimation, with a decrease in pressure, water vaporizes faster than H_3PO_4 (the vapor pressure of H_3PO_4 is much lower than that of water at 25°C), increasing the *pH* of the residual solvent. Monetite is a more stable phase than brushite at lower *pH* and therefore it is possible that the phase change is driven by the high residual concentrations of H_3PO_4 during sublimation. The 75% scaffold had a denser packing of mineral, as expected from the increased weight fraction of mineral.

The compressive stress–strain curves for the scaffolds exhibited shapes characteristic of cellular solids, with the three regimes corresponding to linear elasticity, cell collapse and, at high strains, densification [95]. The Young's modulus and compressive strength of the 50% scaffold were higher than those of the 75% scaffold. This was expected from the lower stiffness and strength of the 75% scaffold struts and the lower relative density of the 75% scaffold. The inferior strut properties of the highly mineralized scaffold are attributed to the water retention of the scaffold, as described above. The Young's modulus and strength of these scaffolds are in the lower range, relative to mineralized scaffolds made by other techniques (Table 2.3).

Scaffold	E^* (kPa)	σ^* (kPa)	Porosity (%)	Reference
Dry				
MCG (50 wt.% mineral)	762	85	85	[69]
MCG (50 wt.% mineral)	720-1000	83-102	96	Current scaffold
MCG (75 wt.% mineral)	204-495	28-43	97	Current scaffold
Chitosan/TCP	1000-3000	100-300	90	[90]
Gelatin/HA (10-30 wt.% mineral)	2280-4010	-	85	[89]
Chitosan/Gelatin/TCP	830-10,880	90-880	-	[51]
Collagen/alginate/HA	50,000-350,000	5000-25,000	65-80	[54]
Hydrated				
MCG (50 wt.% mineral)	4-15	0.34-2	96	Current scaffold
Collagen/HA (70 wt.% mineral)	37-75	-	87-95	[88]
Collagen/HA (80 wt.% mineral)	50-300	30-60	95	[55]

Table 2.3. Mechanical properties Elastic moduli, E^*, collapse strengths, σ^*, and porosities of various bone regenerating composite scaffolds based on natural polymers and calcium phosphate ceramics [103]. Note: TCP = Tri-calcium phosphate, and HA = Hydroxyapatite.

We can compare the measured properties of the scaffolds with values predicted from engineering models. We first estimate the modulus of the solid strut material, using a simple Voigt–Reuss composite model, and then estimate the modulus of the scaffold, using a cellular solids model [95]. The upper and lower bounds on the Young's modulus of the solid for the 50% by weight MCG scaffolds are estimated from the composites model, based on the Young's modulus of collagen and brushite. The Young's modulus of collagen struts in a DHT-DRY CG scaffold has been measured to be 762 ± 35.4 MPa,

from AFM-enabled strut bending tests [17]. The Young's modulus of brushite is assumed to be similar to that of hydroxyapatite (~ 110 GPa) [94, 135]. The volume fractions of collagen and brushite in the 50% by weight MCG scaffold are 0.642 and 0.358, respectively (based on the mass fractions obtained from the XRD results, as described above). The composite Young's modulus of the solid for the 50% DHT-DRY scaffold is predicted to range between 1 and 40 GPa. Our measured value of the solid strut modulus $E_s^{NX\text{-}DRY}$ for the 50% scaffold is 9.15 GPa, while that estimated for the DHT-DRY scaffold, $E_s^{DHT\text{-}DRY}$, is 10.84 GPa; both values are closer to the lower bound of this composite model, as might be expected from the unaligned distribution of brushite within the struts. The Young's modulus of the dry MCG scaffold strut material is comparable to wet cortical bone (~ 10–20 GPa).

Cellular solids models for open-cell foams predict values of Young's modulus, E_S, and compressive strength, σ_{fS}, of the 50% DHT-DRY scaffold of 15.7 and 0.35 MPa (Eq. (2.4) and (2.5)), respectively, compared with our experimentally observed values of $E^* \sim$ 0.8 MPa and $\sigma_{fs} \sim 0.100$ MPa. For the 75% scaffold, the model predicts $E^* = 5$ MPa and $\sigma_{fs} = 0.14$ MPa, compared with our experimentally observed $E^* \sim 0.4$ MPa and $\sigma_{fs} \sim 0.04$ MPa. The modulus and strength data are factors of ~ 10–15 and 3 times lower than the values given by the cellular solids model, respectively. Possible reasons for the discrepancy include the observed presence of defects, such as voids and cracks in the walls and struts of the scaffold, as well as disconnected walls and struts [136-139]. This was apparent from the SEM and optical images of the scaffolds (Figure 2.11). The above reduction in properties correspond to 25–40% defects by volume in the scaffold [137]. In

addition, our approximation of the scaffold pore wall rupture strength (as measured via nanoindentation) tends to underestimate the actual strength of the scaffold solid, such that one would reasonably expect the cellular solids model prediction to underestimate the experimentally measured scaffold strength.

The mechanical properties of scaffolds in this study are lower than those of scaffolds described in the literature (Table 2.3). They are also substantially lower than theoretically predicted by engineering models, suggesting that they can be improved with appropriate control of the microstructure. In our future work, we seek to improve the mechanical properties of the scaffolds.

2.5 Conclusions

MCG scaffolds with 50% and 75% by weight mineral content were fabricated via a titrant-free triple co-precipitation method followed by freeze-drying. The pore sizes for both scaffolds were in the range of 200–350 μm, which is optimal for bone growth [20, 37, 128, 129]. For both scaffolds, the mineral phase was distributed throughout the walls, which mimics bone and is an improvement over existing mineralized scaffolds in which the mineral simply coats the outside of the collagen struts [48, 90, 130-132]. The 50% NX-DRY scaffold had brushite as the major mineral phase with a negligible amount of monetite (~ 3 wt.%), while the 75% NX-DRY scaffold was comprised of ~67 wt.% of brushite and 33 wt.% of monetite. The elastic moduli and strength of the 50% scaffold were typically about twice and three times those of the 75% scaffold, respectively. This unexpected decrease in Young's modulus and strength with increasing mineral content was attributed to lower solid properties, lower relative density and more defect sites in

the highly mineralized scaffold. The mechanical properties of the scaffolds in this study are lower than those of mineralized scaffolds made by other techniques, as well as cortical and cancellous bone. The mechanical properties of the scaffolds in this study are also less than the values predicted by engineering models, suggesting that there is potential for improved performance with appropriate control of the microstructure, to eliminate voids and unsupported walls and struts. Future research is directed towards modifying the current fabrication techniques to obtain mechanically stiffer and stronger scaffolds.

CHAPTER 3. Microstructure and Mechanical Properties of Mineralized Collagen-Glycosaminoglycan Scaffolds with Increased Relative Density

3.1 Introduction

Scaffolds for tissue regeneration are three-dimensional porous matrices which mimic body's own extracellular matrix, onto which cells attach, multiply, migrate, and begin synthesizing new tissue [18]. Scaffolds also serve several other functions, such as (1) structurally reinforcing the defect, (2) preventing ingress of surrounding tissue, and (3) acting as a delivery vehicle for cells, growth factors, or genes [19]. Although unproven, a widely believed design paradigm for scaffolds is that mimicking the composition of the natural tissue as closely as possible improves the capacity for regeneration [20]. The ability of a scaffold to regenerate tissue depends on its pore size, pore shape, porosity, biodegradability and mechanical properties. The average pore diameter must be large enough for cells to migrate through the pores yet small enough to retain an appropriate specific surface area for sufficient cell binding. For example, pore sizes in excess of 100 μm are optimal for bone growth [20, 37, 128]. Equiaxed pore shape and homogeneity are optimum for uniform cell adhesion and distribution of extracellular matrix proteins. Scaffolds must have large enough porosity (generally greater than 90%) and

interconnectivity for effective transfer of cells and metabolites [4]. The degradation rate of the scaffold has to be roughly equal to the regeneration rate of the tissue. And cells have been observed to be sensitive to the mechanical properties of the scaffold which in turn affects the overall construct bioactivity [25].

Ideally, scaffolds should be similar to their natural counterparts in terms of chemical composition and physical structure. For this reason, natural polymers such as collagen are of major interest. To this end, collagen-glycosaminoglycan (CG) scaffolds have been developed and used clinically for skin regeneration and experimentally for nerve regeneration over the past three decades [5, 22, 61, 63, 67, 140-147]. Composite scaffolds of collagen or gelatin with ceramics (e.g. hydroxyapatite and tri-calcium-phosphate); *i.e.*, mineralized CG (MCG) scaffolds have been developed to regenerate hard tissues such as bone [48, 49, 51, 52]. The most recent fabrication technique improves upon this mineralization process by forming a triple co-precipitate of mineral, collagen and glycosaminoglycan, without using a titrant, by controlling the molarity of the reactant acid and molar ratios of the different calcium sources [69-73, 103, 110]. Due to the *in situ* co-precipitation of the mineral phase, calcium phosphate crystals form within the collagen fibers, resulting in a more uniformly mineralized scaffold. Freeze drying is then used to fabricate porous scaffolds from the triple co-precipitated slurry. These MCG scaffolds have regenerated subchondral bone at 16 weeks in a 4 mm diameter and 6 mm depth defect site at the knee joint in a goat model [19].

Extensive microstructural and mechanical characterization of CG and of MCG scaffolds of varying mineral content has been reported by Harley *et al.* [17] and by Kanungo *et al.*

[103], respectively. Critical mechanical properties of scaffolds include elastic modulus, E^*, compressive crushing strength, σ^*, and compressive crushing strain, ε^*. Mechanical properties of different MCG scaffolds (along with the triple co-precipitated scaffolds) are compared in literature [103]. The triple co-precipitated mineralized scaffolds have relative densities (the density of the cellular solid, ρ^*, divided by that of the solid from which it is made, ρ_s) of roughly 0.03-0.04; that of trabecular bone varies from 0.05 – 0.60 [94, 96]. The mechanical properties of human compact and trabecular bone, along with 50 wt.% MCG scaffold (with a relative density, ρ^*/ρ_s, of 0.04), are listed in Table 3.1.

	Condition	E^* (MPa)	σ^* (MPa)
Compact bone	Wet	10,000 – 20,000	110 - 254
	Dry	16,500 – 33,000	170 - 390
Trabecular bone	Wet	90 – 1,000	1 - 30
	Dry	150 – 1,650	1.5 - 45
50 wt.% MCG scaffold	Wet	0.004 – 0.015	0.0003 – 0.002
	Dry	0.2 - 1	0.03 – 0.1

Table 3.1. Mechanical properties of human compact bone, trabecular bone, and 50 wt.% MCG scaffold with $\rho^*/\rho_s = 0.04$ [103, 148-150].

As described in chapter 1, stem cells differentiate to osteoblast-like cells on substrates with a matrix stiffness of 25-40 kPa. Therefore, ideally, the mechanical properties of the hydrated mineralized CG scaffold should be in a similar range for regenerating bone. In addition, it is also critical that the scaffold should have sufficient stiffness and strength to maintain its shape and size during surgical procedures such as implantation and to enhance bone in-growth while preventing encroachment of non-osseous tissue and competing cell types after implantation [100]. The optimal requirements for the above

properties vary depending on the defect site and there are no established optimal magnitudes of the mechanical properties from an implementation point of view [151]. The current triple co-precipitated MCG scaffold (with a ρ^*/ρ_s of 0.04) can be crushed by hard thumb pressure. Hence, it is critical to improve the mechanical properties of the MCG scaffold such that they can be functionally suitable for bone regeneration. The mechanical properties (E^* and σ^*) of the scaffold depend on those of the solid (E_s and σ_{fs}) they are made from as well as the relative density of the scaffold, (ρ^*/ρ_s) [4, 17, 95, 103]. The overall properties of the scaffolds can be improved by either improving the properties of the solid it is made from or by increasing the relative density of the scaffold. Previous attempts to increase the mechanical properties of the scaffold by increasing the mineral content led to scaffolds with lower mechanical properties due to the introduction of defects [103]. Our previous attempts to increase the mechanical properties by increasing the volume fraction of the components of the slurry have not been successful due to the difficulty in mixing the viscous slurry at higher volume fractions of the mineral, collagen and GAG [17]. In this chapter we describe a new technique to improve the mechanical properties by increasing the relative density of the scaffold by a vacuum filtration technique.

3.2 Materials and methods

Fabrication of the MCG scaffolds

A mineralized collagen-glycosaminoglycan suspension (50 wt.% mineral) was fabricated using microfibrillar, type I collagen isolated from bovine achilles tendon (Sigma-Aldrich Chemical Co, St. Louis, MO), chondroitin-6-sulfate (GAG) isolated from shark cartilage

(Sigma-Aldrich Chemical Co., St. Louis, MO), phosphoric acid (H_3PO_4) (EMD Chemicals Inc., Gibbstown, NJ), calcium nitrate ($Ca(NO_3)_2.4H_2O$) and calcium hydroxide ($Ca(OH)_2$) (Sigma-Aldrich Chemical Co., St. Louis, MO). The suspension was prepared by combining collagen (0.019 wt.%), GAG (0.002 wt.%), calcium nitrate (0.004 wt.%), and calcium hydroxide (0.009 wt.%) in a solution of 0.14M phosphoric acid (*pH* 1.47) through a triple co-precipitation method described elsewhere [4, 69-73, 103, 110]. The collagen was mixed with phosphoric acid solution at 15,000 rpm and 4°C in an overhead blender (IKA works Inc., Wilmington, NC) for 60 minutes. Glycosaminoglycan was added to the collagen-phosphoric acid mix using a peristaltic pump (Manostat, New York, NY) and mixed for another 60 minutes at 15,000 rpm. Dry-mixed calcium nitrate and calcium hydroxide were added to the collagen-GAG-phosphoric acid solution and mixed for additional 15 minutes at 15,000 rpm. The suspension was mixed for an additional 24 hours on a magnetic stirrer at room temperature and was stored at 4°C. The co-precipitate within the slurry had a mass of 0.042 g per 1 ml of slurry; we refer to the density of the co-precipitate within the slurry as 0.042 g ml^{-1}.

The above slurry (denoted as 1×, where 1× ≡ 0.042 g ml^{-1}) was densified using the set-up shown in Figure 3.1. A cylindrical polysulfone mold (McMaster Carr Supplies, Dayton NJ), with an inside diameter of 5.7 cm, was perforated at the base with holes of 1 mm diameter for filtering the solvent to the aluminum base. Two filter papers with 5 μm pore diameter (VWR, West Chester, PA) were placed at the base of the mold in order to filter out desired amount of the solvent. The 1× slurry was poured into the mold and subjected to vacuum as shown in the schematic. The extracted solvent was collected in the bottom

container; the slurry remaining in the top compartment became denser as the time the suspension was subjected to vacuum increased.

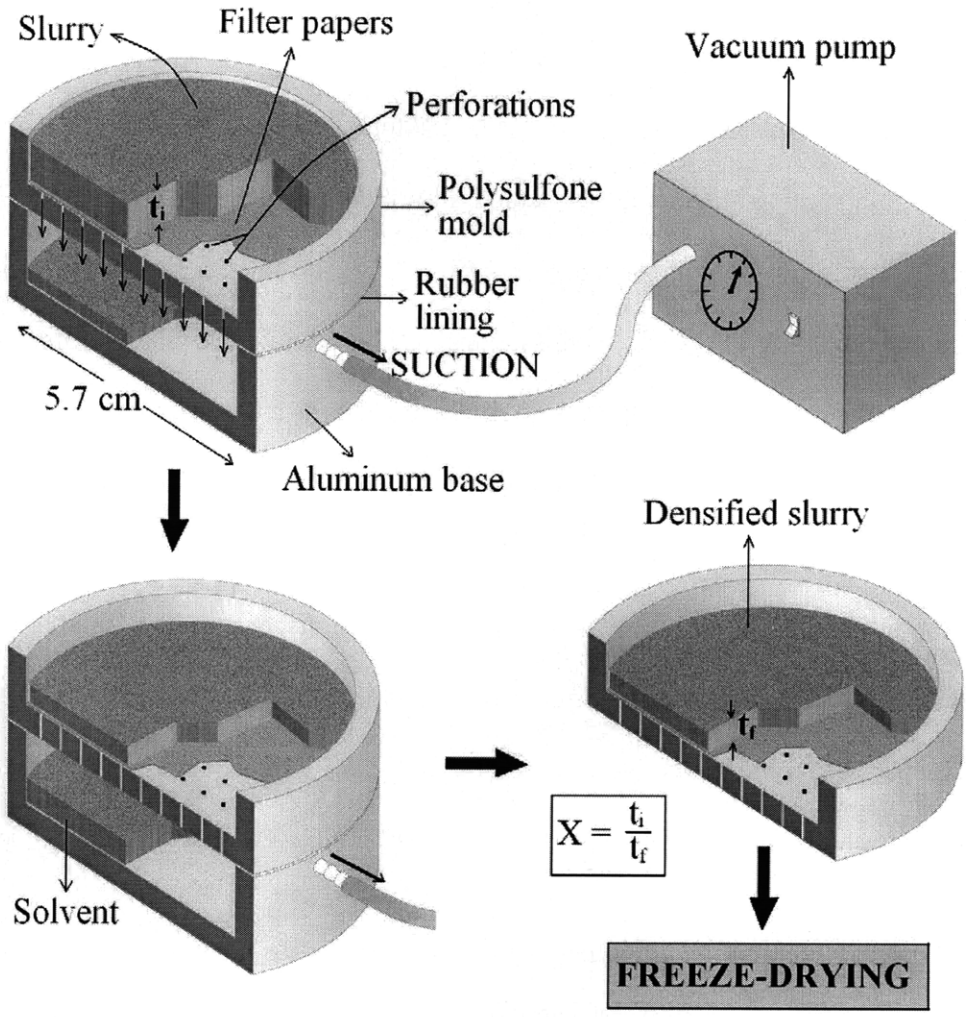

Figure 3.1. Schematic of the vacuum filtering process. The initial low density slurry is densified via vacuum suctioning the solvent to the bottom container. The final density of the slurry is controlled by the time the slurry is subjected to vacuum [152].

The density of the co-precipitate in the remaining slurry in the top compartment was calculated by dividing the initial solid weight by the remaining volume of the slurry (or in other words $\times = t_i/t_f$ where t_i and t_f were the initial thickness of the 1× slurry and the final

thickness of the densified slurry, respectively). The density was plotted against the time it was subjected to vacuum, as shown in Figure 3.2. The densification saturates at a density of 4.5× which is equivalent to 0.189 g of the co-precipitate per 1 ml of slurry. To achieve a particular density, the initial slurry can be filtered under vacuum for a specific time according to this plot. For this study the MCG slurry was densified to three higher densities of the co-precipitate within the slurry: 2× (0.084 g ml^{-1}), 3× (0.126 g ml^{-1}), and 4× (0.168 g ml^{-1}).

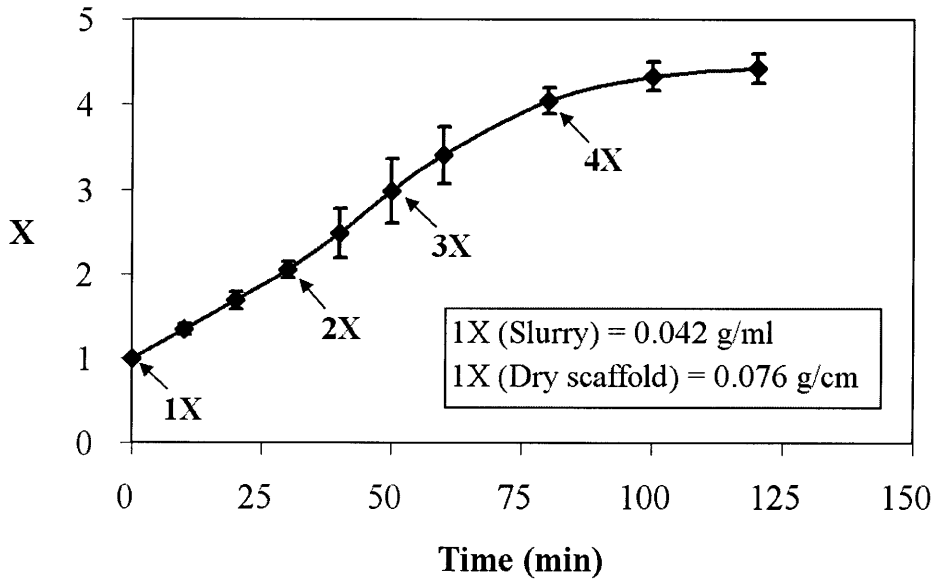

Figure 3.2. Densification vs. time for an input of 80 ml MCG slurry is shown. The starting density was 0.042 g of co-precipitate per 1 ml of slurry which corresponds to a dry scaffold density of 0.076 ± 0.003 g/cm^3 [152].

Scaffolds with four nominal densities (1×, 2×, 3×, and 4×) were fabricated through freeze-drying. The 1× suspension was freeze-dried in a rectangular polysulfone mold with dimensions of 12 × 3 × 1cm (x-, y-, z-axis respectively) (Figure 3.3). The denser suspensions, 2×, 3×, and 4×, were freeze-dried in the cylindrical polysulfone molds (r-

and z-axis are in the radial and through-thickness directions respectively) in which they were subjected to vacuum because it was difficult to transfer the densified slurry to another mold without disturbing the homogeneity of the slurry (Figure 3.3). The molds were placed in a freeze-drier at room temperature, and then freeze-dried as described elsewhere [17, 66, 68, 74, 111]. The MCG suspension was cooled to -10°C at a cooling rate of 0.1°C min^{-1} and kept at that temperature for 6 hours to allow the suspension to freeze completely. Heat transfer was primarily in the through-thickness or z-direction. The frozen suspension was then sublimated at 25°C under vacuum for 48 hours to obtain the dry scaffold.

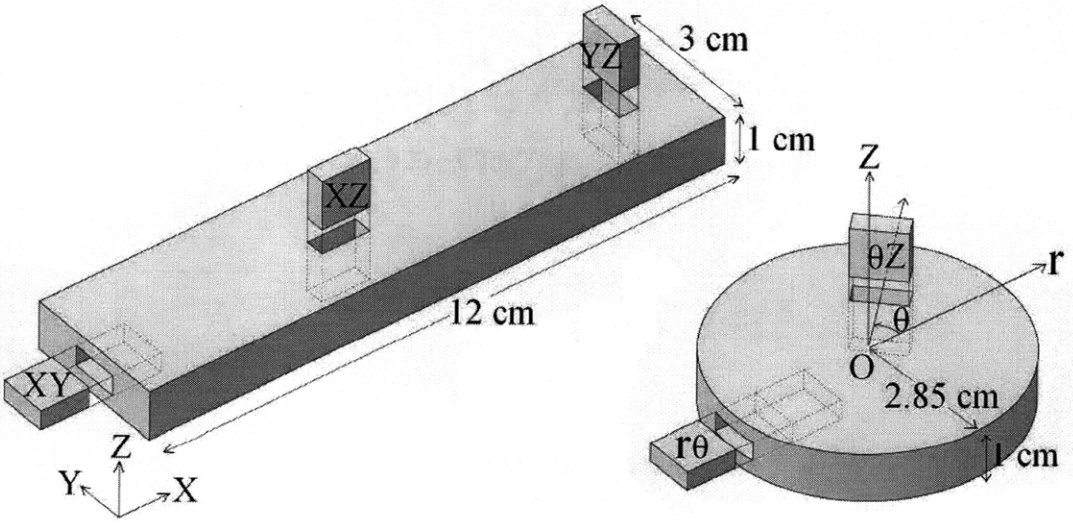

Figure 3.3. Scaffold geometries for the 1× (rectangular) and the 2×, 3×, 4× (cylindrical) scaffolds. Rectangular specimens were cut out of these scaffolds from different planes (as shown above) for pore size analysis. Plane of the scaffold sheet is normal to the z-axis [152].

Crosslinking of the 3× MCG scaffold

Two techniques were used to cross-link the 3× scaffold: (1) dehydrothermal treatment (DHT) and (2) 1-ethyl-3-(3-dimethylaminopropyl) carbodimide treatment (EDAC). The parameters for the DHT treatment were guided by previous work on CG scaffolds [17, 22, 69, 76, 110]. The freeze-dried scaffold was placed under vacuum (30 mTorr) at a temperature of 105°C for 24 hr. The EDAC process was carried out on the scaffold according to previously described methods [69, 74, 76, 110]. A 5:2:1 molar ratio of EDAC:NHS:COOH (based on the mass of the MCG scaffold samples) was used for the current study (where the COOH groups are on the MCG scaffolds). Briefly, the scaffolds were first hydrated in deionized water for ~15 min. The required amount of EDAC/NHS solution was then mixed into the deionized water and the scaffolds were maintained in this solution for ~1 hr. Samples were prepared and tested in the dry state as well as hydrated state (soaked in 10% phosphate buffered saline (PBS) solution for at least 12 hr before testing).

Microstructural characterization of the MCG Scaffolds

Relative density was calculated from the dry densities of collagen, brushite ($CaHPO_4.2H_2O$) and monetite ($CaHPO_4$) according to Eq (2.1); where x_{coll}, $x_{brushite}$ and $x_{monetite}$ are the weight fractions of collagen, brushite and monetite in the scaffold material (note that $x_{coll} + x_{brushite} + x_{monetite} = 1$), ρ_{coll}, $\rho_{brushite}$ and $\rho_{monetite}$ are the densities of dry collagen, dry brushite and dry monetite and ρ^* is the measured density of the dry scaffolds. The weight fractions of brushite, monetite and collagen for a 50 wt.% MCG scaffold were determined using X-ray diffraction in our previous work; $x_{coll} = 0.5$, $x_{brushite} = 0.485$ and $x_{monetite} = 0.015$ [103]. The dry densities of collagen, brushite and monetite

are 1.3 g cm^{-3}, 2.33 g cm^{-3} and 2.93 g cm^{-3}, respectively [22, 103, 116]. The contribution of GAG was not considered, as the amount of GAG was much less than that of the other constituents. The density of the solid wall material of the 50 wt.% MCG scaffold, ρ_s, is 1.67 g cm^{-3} according to Eq (2.1).

The pore microstructure was measured using optical images of the scaffold at various cross sections through the thickness of the scaffold. Six rectangular specimens with dimensions 5 × 5 mm taken from different locations (for each plane: *xy*, *yz*, *xz*, θz, $r\theta$; and for each of the 4 densities) were cut using a laser cutter, model X660 (Universal Laser System, Scottsdale, AZ) and were embedded in glycolmythacrylate (Polysciences Inc., Warrington, PA). The specimens were cut at high speed and low power setting (3 cm s^{-1}, 10 Watt) such that the cell structure of the specimens was not damaged by the cutting technique (except a very thin layer at the periphery). The embedded specimens were cut into 5 μm-thick sections (5 to 6 sections from each rectangular specimen) at various depths along the plane of analysis using a Leica RM2165 microtome (Mannheim, Germany). The sectioned films were stained with Aniline-Blue (Polysciences Inc., Warrington, PA) and observed under an inverted optical microscope (Nikon Optiphot, Japan) at 40× magnification. Images were obtained using a CCD color video camera (Optronics Engineering, Inc., Goleta, GA), and image analysis was conducted using Scion Image analysis software (Scion Corporation, Frederick, MD).

The mean pore diameter of the scaffold, *D*, on different planes (yz, xz and xy for the 1× scaffold; $r\theta$ and θz for the 2×, 3×, and 4× scaffolds as shown in Figure 3.3) was measured using the mean intercept method. *D* for a particular plane is the average of the major and

minor axes of the best-fit ellipse on that plane [66, 103]. The ratio of the minor to the major axes of the best-fit ellipse gives the pore anisotropy ratio, R, on that plane [66, 103]. The average wall thickness in two-dimension, $\bar{t}_{2d}$, was calculated using Euclidean distance mapping from the 2D images of the scaffolds on different planes [153]. The average wall thickness in three-dimension, t, was calculated from $\bar{t}_{2d}$ by assuming spherical pores with mean pore diameter, D, as shown in Figure 3.4.

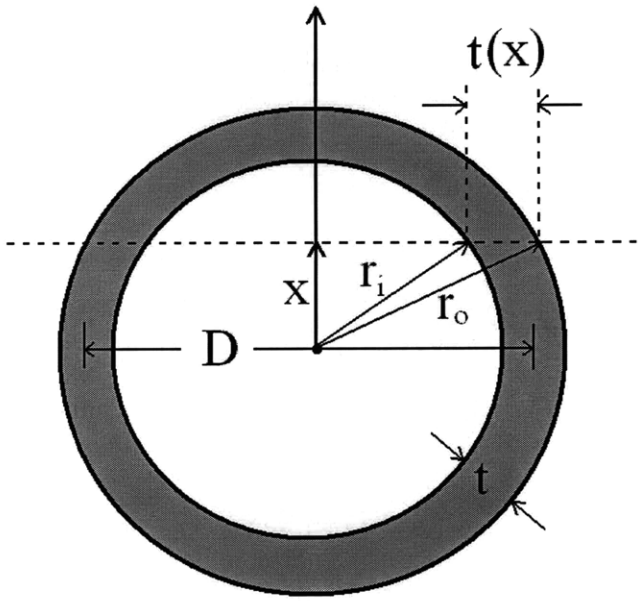

Figure 3.4. Schematic of the pore assuming a speherical shape with average diameter, D, and average pore wall thickness t.

The optical images were taken from the 2D cross sections of the scaffold at different heights. Assuming the pores were cross sectioned equally through the diameter, the 2D thickness observed at a height x from the center of the pore, $t_{2d}(x)$, (Figure 3.4) is given by:

$$t_{2d}(x) = \begin{pmatrix} \sqrt{r_o^2 - x^2} - \sqrt{r_i^2 - x^2} & x \le r_i \\ \sqrt{r_o^2 - x^2} & r_i \le x \le r_o \end{pmatrix} \tag{3.1}$$

where r_0 and r_i are the outer and inner radii of the pore (Figure 3.4). r_0 and r_i can be given in terms of D and t as:

$$r_i = \frac{D-t}{2}, r_o = \frac{D+t}{2} \tag{3.2}$$

The average pore wall thickness in two-dimension, $\bar{t}_{2d}$, that we observe from the optical images can be calculated by averaging $t_{2d}(x)$ over the diameter of the spherical pore as:

$$\bar{t}_{2d} = \frac{\int_0^{r_o} t_{2d}(x)dx}{\int_0^{r_o} dx} = \frac{1}{r_o}\left[\int_0^{r_i} t_{2d}(x)dx + \int_{r_i}^{r_o} t_{2d}(x)dx\right] \tag{3.3}$$

Using Eq (3.1), (3.2), and (3.3), $\bar{t}_{2d}$ can be represented in terms of D and t as:

$$\bar{t}_{2d} = \frac{\pi Dt}{2(D+t)} \tag{3.4}$$

Therefore, from Eq (3.4), the average three-dimensional pore wall thickness, t, can be calculated from the average two-dimensional pore wall thickness, $\bar{t}_{2d}$, and average pore diameter, D, diameter as:

$$t = \frac{2D\bar{t}_{2d}}{\pi D - 2\bar{t}_{2d}} \tag{3.5}$$

Scanning electron microscopy (Leo VP438 SEM Leo Electron Microscopy Inc., Thornwood, NY) was used to study the pore structure of the scaffolds. Specimens were mounted on an aluminum holder; the specimens were not gold coated. To study the mineral distribution through the wall thickness, specimens were embedded in resin (similar to the specimen preparation for the pore size measurement as described above) and 5 μm-thick sections were sliced out. The backscattered electron detector was used under variable pressure mode to obtain the images.

Mechanical characterization of the MCG Scaffolds

Compressive stress-strain curves for the dry scaffolds were measured for loading in the z-direction using an Instron model 4201 universal testing instrument (Instron Corporation, Norwood, MA). Compressive stress-strain curves for the hydrated scaffolds (soaked in 10% PBS for 72 hour prior to test) were measured using a Zwick/Roell Z2.5 static materials tester (Zwick GmbH & Co., Ulm, Germany). For each density of scaffold, six cylindrical specimens, 5 mm in diameter and 5-8 mm thick, were cut at different locations in the scaffold along the through-thickness direction (z-axis) using a laser cutter as described above. All of the specimens were compressed at a uniform strain rate of 0.002 sec^{-1} up to a maximum strain of 0.80.

The Young's modulus of the solid comprising the scaffold, E_S, was measured via bending of individual scaffold struts using an atomic force microscope (3DMFP, Asylum Research, Santa Barbara, CA) as described in CHAPTER 2 [103, 121-123]. Six rectangular beams were cut from the walls of the 1× scaffold at different locations using microsurgical forceps and a scalpel under an inverted optical microscope. One end of

each beam was bonded to a rigid support with cyanoacrylate, creating a cantilevered beam of length L from the support point (Figure 2.2). The bending test was carried out using an AC160TS cantilever (Olympus, Tokyo, Japan) of stiffness = 44.82 N/m, as measured via thermal power spectral density [121]. The force-deflection relation (F-Δ) of the beam is given by Eq (2.2); where $I = bh^3/12$ (where b and h are the width and thickness of the scaffold strut as shown in the figure). L could not be measured accurately from the beam set-up (Figure 2.2) because the support point was not well-defined, but it was estimated by loading the cantilever at various points along the length of each strut (five to seven points) and measuring F vs. Δ for each loading point [103].

The rupture strength of the solid for the 50 wt.% MCG scaffold, σ_{fs}, was estimated via nanoindentation using a Hysitron triboindenter (Hysitron, Inc., Minneapolis, MN) in our previous work [103]. Samples were cut from the walls of the scaffold using microsurgical forceps and a scalpel under a bottoms-up optical microscope. The samples were bonded to a glass slide using cyanoacrylate and indented using a Berkovich indenter (Hysitron, Inc., Minneapolis, MN). Rupture strength, σ_{fs}, was approximated from the calculated hardness, H, or mean pressure at maximum load given by Eq (2.3); where σ_{ys} is yield strength, P_{max} is the maximum indentation load and A_c is the projected area of contact.

Cellular solids model of the MCG scaffolds

The relative density of the scaffold can be related to the ratio of edge thickness, t, to the edge length, l, using a polyhedral unit cell model [95]. In the literature a tetrakaidecahedral unit cell (a fourteen-sided polyhedron that packs to fill space) has been

used to model the geometry of CG scaffolds (Figure 3.5) [66]. Here we have used the same unit cell to model the MCG scaffolds.

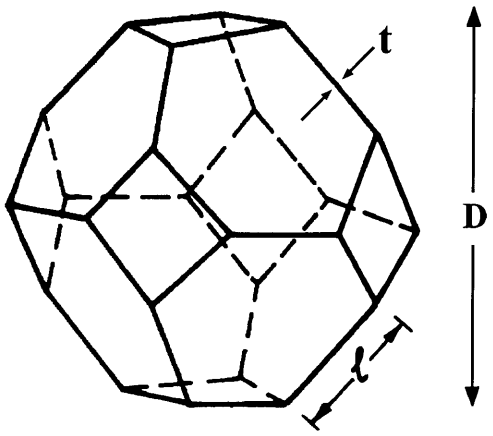

Figure 3.5. The tetrakaidecahedral unit cell that is used to model the unmineralized and mineralzeid CG scaffold microstructure [95].

The relative density of a low density open cell foam modeled with the tetrakaidecahedral unit cell is given as:

$$\frac{\rho^*}{\rho_s} = 1.06\left(\frac{t}{l}\right)^2 \tag{3.6}$$

where t is the edge thickness and l is the edge length of the unit cell [95]. To calculate the mean spacing (equivalent to the diameter, D) between opposite sides of this structure, we assume that the internal volume is similar to that of a sphere of diameter D. Using this assumption, the average pore diameter, D, can be calculated from the edge length by [66]:

$$D = 2.78l \tag{3.7}$$

Therefore the relative density can be represented in terms of the diameter, D, and edge thickness, t, as:

$$\frac{\rho^*}{\rho_s} = 8.19\left(\frac{t}{D}\right)^2 \tag{3.8}$$

From Eq (3.8) it is evident that the increase in relative density, ρ^*/ρ_s, of a scaffold results in either increase in the strut thickness, t, or decrease in the pore diameter, D, or both.

The mechanical properties of cellular solids depend on their relative density, the properties of the solid of which the cellular solid is made (such as Young's modulus, E_s, rupture strength, σ_{fs}) and the cell geometry (e.g., open- or closed-cells) [17, 95, 101, 103]. Simple relationships between overall foam mechanical properties (such as Young's modulus, E^*, and crushing strength, σ^*), and the relative density and solid cell wall properties can be derived using dimensional analysis [95, 101]. Eq (2.4) and (2.5) are the key relationships for the Young's modulus, E^*, and the crushing strength, σ^*, for open-cell foams that are relevant for mechanical characterization of the mineralized scaffolds.

Statistical analysis

One-way analysis of variance (ANOVA) and Fisher's protected least significant difference (Fisher's PLSD) methods were used to determine statistical significance between different sets of data and pair wise data sets, respectively. A probability value of 95% ($p < 0.05$) was used to determine the significance. All the measurements are reported as mean ± standard deviation. The symbols *, **, and *** in Table 3.1-3.4 indicates statistically significantly different results.

3.3 Results

Microstructural characterization

The measured overall scaffold dry densities (ρ^*) for the MCG scaffolds are listed in Table 3.2. The starting densities of the co-precipitate in the slurry were less than the dry scaffold densities (for example: for the 1× scaffold, 0.042 g ml^{-1} and 0.076 g cm^{-3} are the slurry and dry densities respectively) partly because some of the solvent was soaked into the collagen reducing the solidified solvent volume (and hence increasing the dry density) [56, 154, 155]. The relative densities can be calculated using Eq (2.1) and are listed in Table 3.2 as well. As expected, the relative densities of the 2×, 3×, and 4× scaffolds were roughly two, three, and four times that of the 1× scaffold, respectively.

Scaffold	ρ^* (g/cm^3)	ρ^*/ρ_s	D (μm)	t (μm)
1×	0.076 ± 0.003	0.045 ± 0.002	311 ± 85	23±2
2×	0.164 ± 0.006	0.098 ± 0.004	196 ± 31*	26±2*
3×	0.228 ± 0.004	0.137 ± 0.002	159 ± 30**	24±2
4×	0.312 ± 0.045	0.187 ± 0.027	136 ± 29**	34±5**

Table 3.2. Dry densities (ρ^*), relative densities (ρ^*/ρ_s), average pore diameters (D), and average wall thicknesses (t) for the 1×, 2×, 3×, and 4× MCG scaffolds [152].

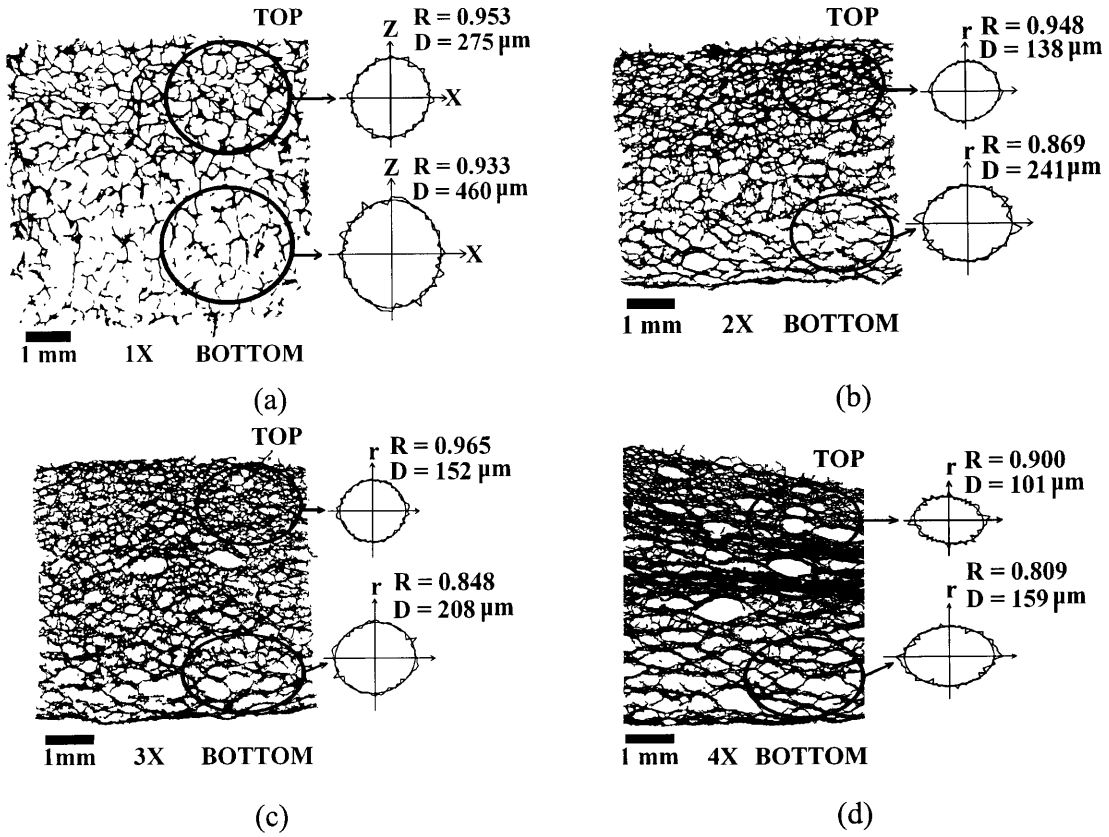

Figure 3.6. Optical micrographs of thin sections of the embedded MCG scaffolds in the *xz*, *yz* or *θz* planes: (a) 1×, (b) 2×, (c) 3×, and (d) 4×. Mean intercept length ellipses, average pore size, *D*, and anisotropy ratio, *R*, for the top and bottom layers of each thin section are shown to the right of each image [152].

Optical images of embedded specimens in the *xz*, *yz*, or *θz* planes, through the thickness of the scaffold sheet, are shown in Figure 3.6. Figure 3.6 also shows mean intercept ellipses with the anisotropy ratio, *R*, and the pore diameter, *D* (to the right of the optical images) at the top and bottom layers of the scaffolds. The scaffolds exhibited a gradation in pore size with smaller pores at the top, closer to the air side during freeze-drying, and increasing pore diameter through the thickness, closer to the cooling plate on the base. Figure 3.6 indicates that pores at the top of the scaffolds were roughly equiaxed for all densities, while the pores towards the bottom of the scaffold were more elliptical at

higher densities. The 4× scaffold had a layered structure in the plane of the scaffold sheet and a bimodal pore structure with significant large elliptical pores between these layers and smaller spherical pores along the surfaces of these large pores (Figure 3.6). The 4× scaffold also had a variation in thickness from the periphery to the center of the scaffold indicating inhomogeneity in the vacuum filtration process.

SEM micrographs of scaffolds showing the plane through the thickness (images taken along the planes containing the z-axis) are shown in Figure 3.7a-d. All the scaffolds exhibited walls as well as thin struts. The 4× scaffold had layered structure as described above with very large elliptical pores between these layers. An SEM micrograph of a resin-embedded 5 μm thick section of a 1× density scaffold strut is shown in Figure 3.7e. The mineral particles are homogeneously distributed through the thickness of the walls. EDAX analysis showed that the white flecks through the thickness of these walls are calcium- and phosphorous- rich particles. In our previous paper [103], we confirmed these to be either brushite or monetite. The mineral distribution was similar for the other scaffolds (2×, 3×, and 4×). Both optical (Figure 3.6) and SEM (Figure 3.7) micrographs show presence of defects such as disconnected walls and struts.

The average pore diameter, D, and the average wall thickness, t, for different relative densities, ρ^*/ρ_s, are also listed in Table 3.2; note that porosity is 1 - ρ^*/ρ_s. The average pore diameter and wall thicknesses were calculated by averaging all the measured values (on different planes). Average pore diameter decreases with increasing relative density of the scaffold. Average wall thickness remained same (statistically non-significant) for the

1×, 2×, and 3× scaffolds whereas it increased for the 4× scaffolds due to inhomogeneous microstructure with occasional thicker layers in the scaffold.

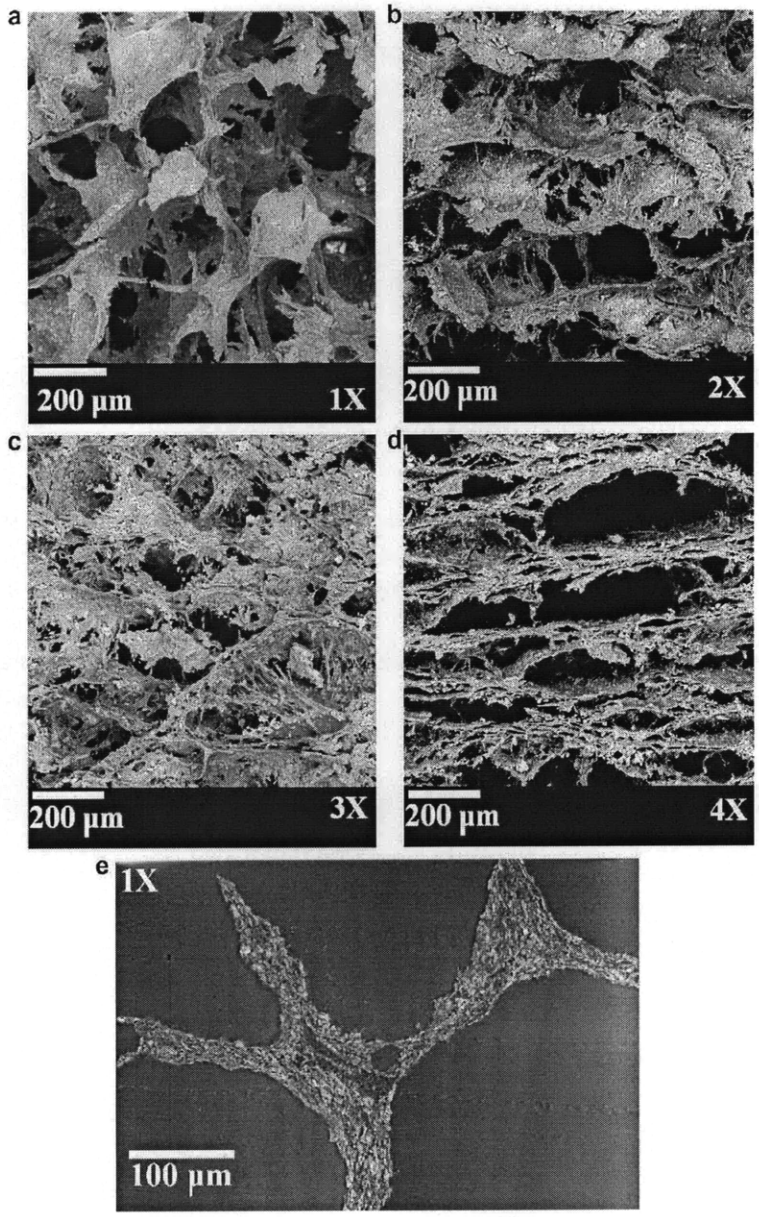

Figure 3.7. SEM micrographs of the MCG scaffolds: (a) 1×, (b) 2×, (c) 3×, and (d) 4×. (e) Mineral distribution through the thickness of the scaffold walls and struts for the 1× scaffold (mineral particles are white). Mineral distributions for 2×, 3×, and 4× scaffold were similar [152].

The relative density is plotted against t/D in Figure 3.8. The best fit curve ($R^2 = 0.9832$) through the data (that also passes through the origin) is:

$$\frac{\rho^*}{\rho_s} = 2.14\left(\frac{t}{D}\right)^{1.5} \tag{3.9}$$

The above equation is somewhat different from Eq (3.8), probably due to the presence of walls as well as edges in the scaffold. We note that for a closed-cell foam, (ρ^*/ρ_s) α (t/l) while for an open cell foam (ρ^*/ρ_s) α $(t/l)^2$; Eq (3.9) is intermediate to these two results. The data for the 4× scaffold is not included in the plot, as, unlike the other 3 densities, it had an inhomogeneous layered structure.

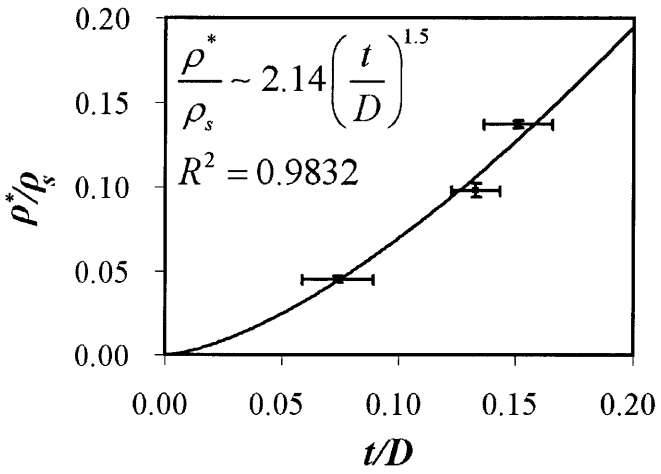

Figure 3.8. The relative density, ρ^*/ρ_s, plotted against the ratio of the wall thickness to the pore diameter, t/D, for the MCG scaffolds [152].

More detailed data for the pore diameter, D, and the anisotropy ratio, R, on different planes are listed in Table 3.3. All the scaffolds had roughly equiaxed pores in the planes of the scaffold sheet (planes xy for 1×, $r\theta$ for 2×, 3×, and 4×). However, as noted above, in the through thickness direction (planes xz or yz for 1×, and plane θz for 2×, 3×, and

4×), as the density increased, the pores towards the bottom of the scaffold were larger and more elliptical, decreasing the overall R.

Scaffold	Plane	D (μm)	R
1×	yz	339 ± 112*	0.945 ± 0.045
	xz	303 ± 85	0.923 ± 0.060
	xy	295 ± 40	0.940 ± 0.049
2×	θz	178 ± 31	0.905 ± 0.057
	rθ	208 ± 24*	0.929 ± 0.047
3×	θz	152 ± 31	0.852 ± 0.087*
	rθ	164 ± 28	0.928 ± 0.049
4×	θz	155 ± 30*	0.831 ± 0.088*
	rθ	123 ± 20	0.948 ± 0.042

Table 3.3. Pore sizes (D) and anisotropy ratios (R) measured on different planes of the MCG scaffolds. Note: 1× scaffold was fabricated as rectangular sheet (and hence Cartesian co-ordinate system) and 2×, 3×, and 4× scaffolds were fabricated as circular sheets (and hence cylindrical co-ordinate system) [152].

Mechanical characterization

Compressive stress-strain plots for loading dry and hydrated scaffolds in the z-direction are shown in Figure 3.9. Distinct linear elastic, collapse plateau and densification regimes were observed for all the scaffolds indicating behavior similar to that of foams [95]. Elastic modulus (E^*), crushing strength and strain (σ^* and ε^* respectively) and collapse modulus ($\Delta\sigma/\Delta\varepsilon$) are measured from the stress-strain curves [95, 103]. Briefly, E^* is the slope of the linear elastic regime, $\Delta\sigma/\Delta\varepsilon$ is the slope of the collapse regime, σ^* and ε^* are

the point of transition from linear to the collapse regime (determined from the intersection of the E^* and $\Delta\sigma/\Delta\varepsilon$ regression lines).

The values of E^*, σ^*, ε^* and $\Delta\sigma/\Delta\varepsilon$ for the scaffolds in the dry and hydrated states are listed in Table 3.4. E^*, σ^*, $\Delta\sigma/\Delta\varepsilon$ increase with increase in relative density of the scaffold from 1× to 3× in both dry and hydrated states. However, the properties of the 4× scaffold are lower compared to those of the 3× scaffold in both the states (except σ^* in the dry state). ε^* remains constant (not statistically different) for different relative densities in both the dry and hydrated states ($\varepsilon^* \sim 5\%$). The mechanical properties, E^*, σ^*, $\Delta\sigma/\Delta\varepsilon$ of the dry scaffolds are two orders of magnitude higher than those of the hydrated scaffolds. For both the dry and the hydrated scaffolds, $\Delta\sigma/\Delta\varepsilon$ is in the same order as that of the E^*. The values of E^*, σ^*, ε^* and $\Delta\sigma/\Delta\varepsilon$ in the z-direction for the 3× scaffolds with different crosslinking treatments are also listed in Table 3.4. The specific crosslinking treatments had no statistically significant effect on any of the properties ($p > 0.05$) for both scaffolds in the dry state, with the exception of the higher strength in the EDAC treatment. In the hydrated state, DHT and EDAC crosslinking increased the E^*, σ^*, and $\Delta\sigma/\Delta\varepsilon$ over that of the non-crosslinked scaffold by 1.5 and 3 times, respectively. There was no statistically significant effect on the crushing strain, ε^*.

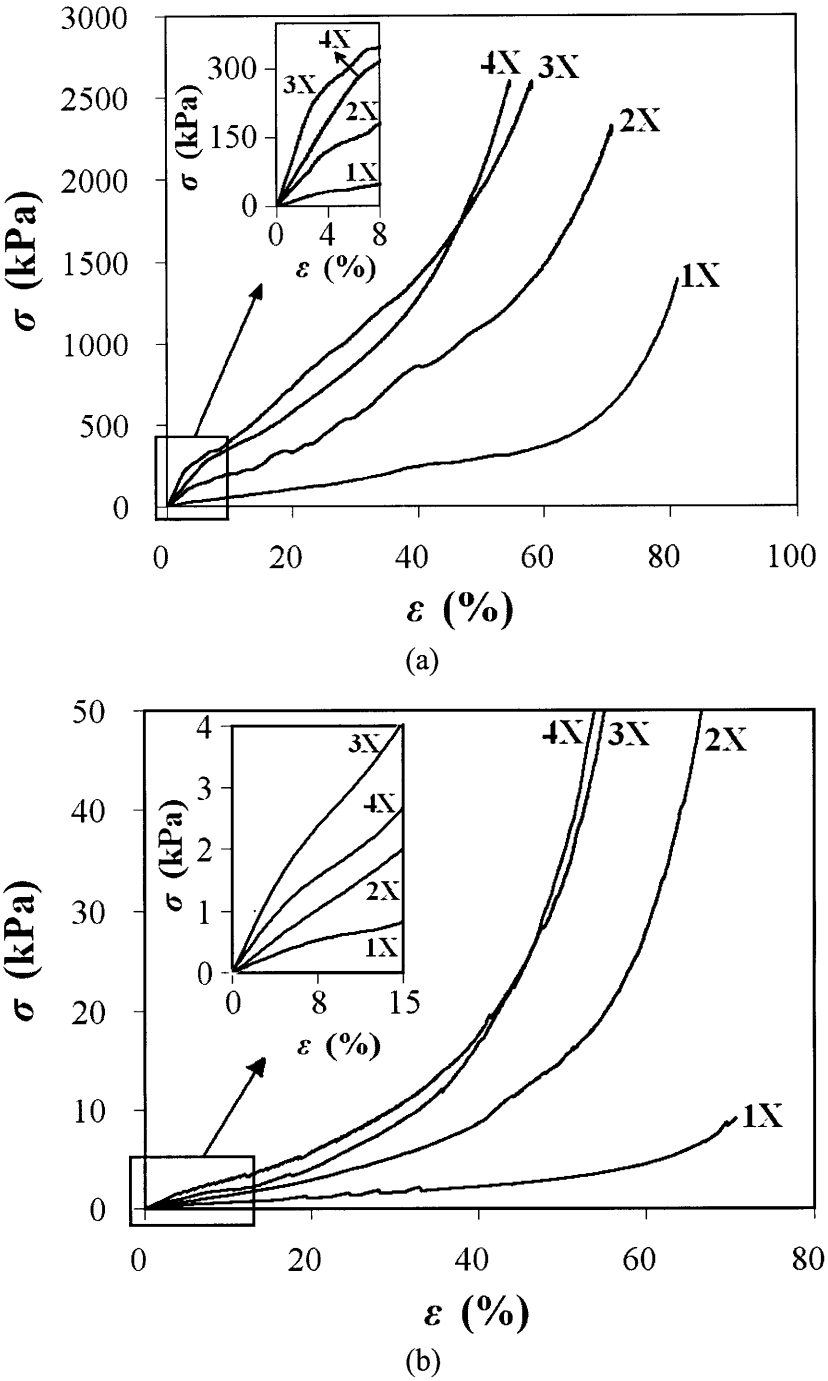

Figure 3.9. Compressive stress-strain plots for the MCG scaffolds: (a) dry (b) hydrated. Distinct linear elastic, collapse plateau and densification regimes were observed for the scaffolds. The linear elastic part is magnified in the insets to show the change in slope between the linear elastic and collapse plateau regimes [152].

Young's modulus of the solid, E_s, was measured on struts removed from the 1× scaffold using the AFM bending test. A typical plot of L vs. $(\Delta/F)^{1/3}$ is shown in Figure 3.10. The fact that the plot is linear indicates that the beam follows Eq (2.2) and the above method is appropriate for measuring the solid Young's modulus. The Young's modulus, E_s, for the dry solid strut from the 1× scaffold was measured to be 7.34 ± 3.73 GPa (Eq (2.2)). Since the higher density scaffolds have the same composition as the 1×, we assume that their solid properties are the same. The measured Young's modulus is not statistically different from the value obtained in our previous work (9.15 ± 0.983 GPa) [103] suggesting that the two different collagen sources used for making the scaffolds in the current paper and in our previous paper [103] have similar mechanical properties. These values are close to that of trabecular bone (e.g. E_s of dry trabecular bone is ~ 18 GPa) [156-160]. The rupture strength, σ_{fs}, is assumed to be 201 ± 52 MPa as measured in our previous work [103].

The data for the relative modulus, E^*/E_s, and the relative crushing strength, σ^*/σ_{fs}, for the dry scaffolds are plotted against relative density, ρ^*/ρ_s in Figure 3.11. The data for the 4× scaffold is not included as, unlike the other 3 densities, it had an inhomogeneous layered structure.

Dry properties					
Scaffold	ρ^*/ρ_s	E^* (kPa)	σ^* (kPa)	ε^* (%)	$\Delta\sigma/\Delta\varepsilon$ (kPa)
1×	0.045 ± 0.002	780 ± 95	39 ± 10	5.00 ± 1.00	480 ± 35
2×	0.098 ± 0.004	3156 ± 760*	132 ± 14*	4.00 ± 1.41	1300 ± 200*
3×	0.137 ± 0.002	6500 ± 1270**	242 ± 32**	4.00 ± 1.00	2680 ± 610**
4×	*0.187 ± 0.027*	*3660± 820**	*275 ± 50***	*4.38 ± 1.15*	*1875 ± 525****
Hydrated properties					
Scaffold	ρ^*/ρ_s	E^* (kPa)	σ^* (kPa)	ε^* (%)	$\Delta\sigma/\Delta\varepsilon$ (kPa)
1×	0.045 ± 0.002	6.44 ± 1.91	0.55 ± 0.07	6.80 ± 2.20*	3.18 ± 1.49
2×	0.098 ± 0.004	17.84 ± 3.61*	0.83 ± 0.18*	4.86 ± 1.37	11.99 ± 2.29*
3×	0.137 ± 0.002	34.83 ± 7.39**	2.12 ± 0.66**	5.63 ± 1.48*	26.78 ± 6.21**
4×	*0.187 ± 0.027*	*38.77 ± 31.2*	*1.79 ± 1.89*	*4.18 ± 1.26*	*15.95 ± 15.07*
Effect of Crosslinking (dry)					
Scaffold	**Treatment**	E^* (kPa)	σ^* (kPa)	ε^* (%)	$\Delta\sigma/\Delta\varepsilon$ (kPa)
3×	Non-crosslinked	6500 ± 1270	242 ± 32	4.00 ± 1.00	2680 ± 610
	DHT (105°C, 24h)	6147 ± 1459	264 ± 78	5.20 ± 2.50	2262 ± 492
	EDAC (5:2:1)	6889 ± 1116	358 ± 84*	6.10 ± 1.50	2544 ± 571
Effect of Crosslinking (hydrated)					
Scaffold	**Treatment**	E^* (kPa)	σ^* (kPa)	ε^* (%)	$\Delta\sigma/\Delta\varepsilon$ (kPa)
3×	Non-crosslinked	34.83 ± 7.39	2.12 ± 0.66	5.63 ± 1.48	26.78 ± 6.21
	DHT (105°C, 24h)	55.95 ± 10.19*	3.26 ± 1.19*	5.55 ± 0.84	43.00 ± 4.06*
	EDAC (5:2:1)	91.67 ± 10.88**	4.15 ± 0.95**	4.66 ± 0.88	79.17 ± 9.66**

Table 3.4. Mechanical properties of the MCG scaffolds in the dry as well as the hydrated state determined from the compression tests [152].

3.4 Discussion

We were able to increase substantially the Young's modulus and the crushing strength of the mineralized scaffold in both the dry and hydrated state by increasing the relative density by a factor of 3. The denser scaffolds, 2× and 3×, in the dry state sustained hard thumb pressure that is critical for scaffold implantation at the defect site. Cross-linking

the scaffolds with EDAC further increased the properties of the hydrated, but not the dry scaffolds. We were able to achieve an increase in Young's modulus of the hydrated scaffold from 6.44 kPa, for the non-cross-linked 1× scaffold, to 34.9 kPa for the non-cross-linked 3× scaffold. Note that the 3× hydrated scaffold has the stiffness in the right range (25-40 kPa as described in chapter 1) for the stem cells to differentiate into osteoblast-like cells. EDAC crosslinking increased the Young's modulus further for the 3× hydrated scaffold to 91.7 kPa. Similarly, we were able to achieve an increase in the crushing strength of the hydrated scaffold from 0.55 kPa, for the non-cross-linked 1× scaffold, to 4.15 kPa for the EDAC cross-linked 3× scaffold.

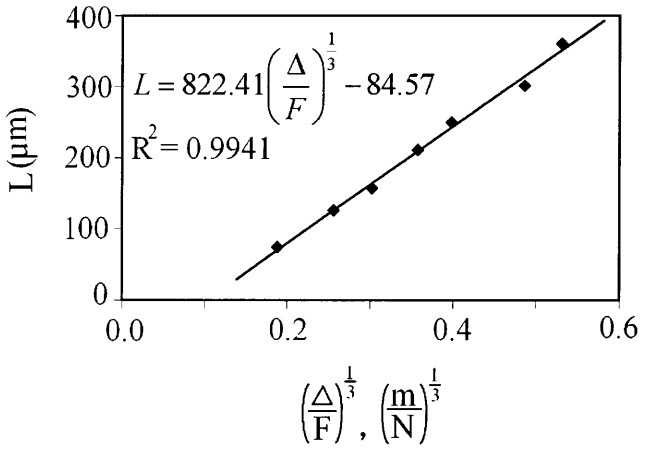

Figure 3.10. Plot of L vs. $(\Delta/F)^{1/3}$ for the 1× MCG scaffold is shown. The slope of this line fit is equal to $(3E_sI)^{1/3}$. A linear variation indicates the strut behaves like a cantilevered beam with constant moment of inertia. Knowing the dimensions of the beam E_s can be calculated [152].

The compressive stress-strain curves for the scaffolds were typical of cellular solids, showing the three regimes of linear elasticity, the collapse plateau and densification. The dependence of the relative Young's modulus and relative crushing strength on relative density were well described by the power exponents derived from cellular solids models

(Eq (2.4) and (2.5)). The curves plotted on Figure 3.11 correspond to the theory (Eq (2.4) and (2.5)) with different constants that reflect the effect of the defects, such as disconnected walls and struts, in the cellular structure. We note that the constants in Eq (2.4) and (2.5) are empirical, based on data in the literature, for intact foams without such defects. A previous finite element study of the effect of missing cell walls on the modulus and strength of two-dimensional honeycombs found that the defects reduced the constants but not the value of the exponent in the cellular solids models [101, 136, 138, 139, 161].

The Young's modulus and crushing strength of the 1× mineralized scaffolds in this study were similar to those of our previous study [103], although we used two different collagen sources in the two studies. Our previous study used a medical grade collagen (Integra Life Sciences, Plainsboro NJ); since then, this source became unavailable to us so that in this study we used a non-medical collagen source (Sigma-Aldrich Chemical Co., St. Louis MO). The slope of the stress-strain curve beyond the crushing strength was steeper in this study than in the previous one, suggesting that there was a larger difference between the weakest and the strongest cells in the structure in this study as compared with our previous one.

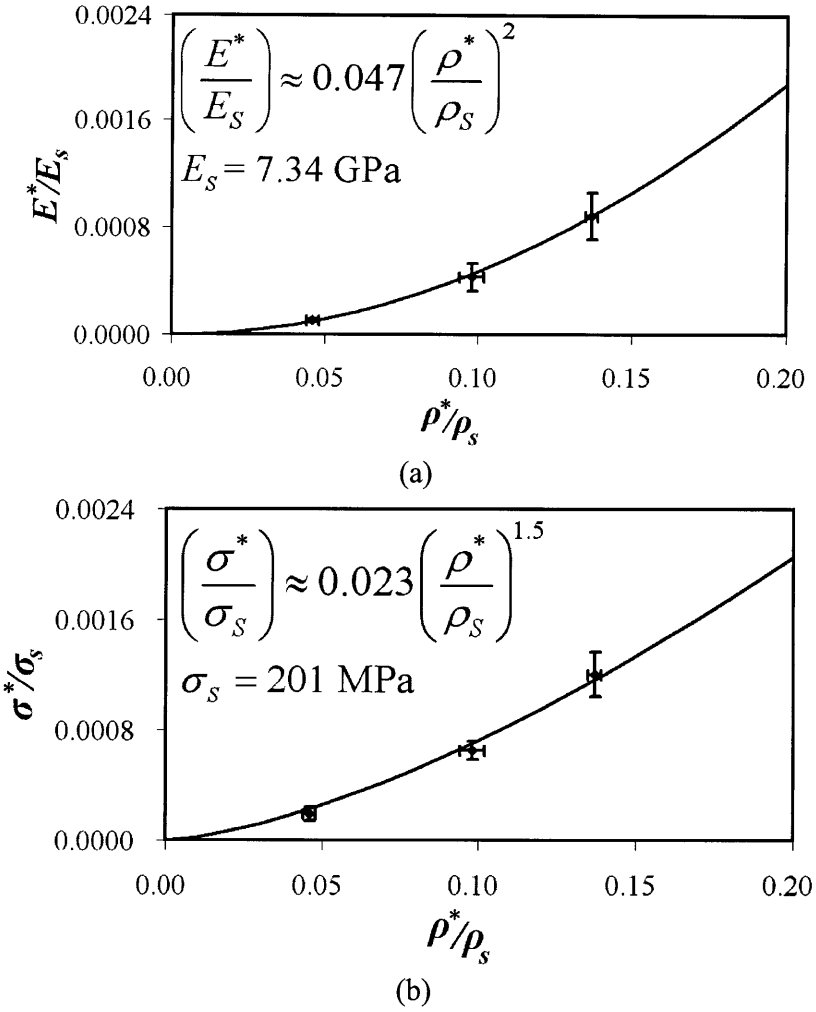

Figure 3.11. (a)E^*/E_s and (b) σ^*/σ_{fs} plotted against relative density, ρ^*/ρ_s, for the dry MCG scaffolds [152].

The maximum dry scaffold relative density that we were able to achieve while maintaining a more or less homogenous microstructure was 0.137 (or 3×). The 4× scaffold had a layered structure with numerous large elliptical cells with the major axis normal to the loading direction; the mechanical properties of the scaffold were adversely affected by this. A practical upper limit on the relative density is that which limits the degree of interconnection between the pores so that cells can migrate through the scaffold; for this reason, the maximum practical relative densities is probably less than

0.25. The cellular models suggest that an increase in the relative density from our base ρ^*/ρ_s = 0.045 (or 1×) to 0.25 should increase the Young's modulus by a factor of 30 and the crushing strength by a factor of 15. Further study is needed to develop methods of increasing the relative density up to this limit while maintaining a homogeneous microstructure.

The scaffolds had an interconnected pore structure with walls as well as struts. All the scaffolds had average pore sizes in the range of 130-350 μm with porosities greater than 80% (Table 3.2). Note that porosity is 1 - ρ^*/ρ_s. Bone cells are 10 – 20 μm in size [94, 162], substantially smaller than the smallest average pore size in our scaffolds. Previous studies have shown that polymer scaffolds with pore sizes between 100 and 1000 μm are suitable for bone growth [2-4, 62]. In addition, our group has previously demonstrated that MC3T3-E1 mouse osteogenic cells attach and migrate into CG scaffolds with average pore sizes between 96 – 150 μm [66]. MCG scaffolds have shown bone regeneration in a goat model [19]. While we have not definitively demonstrated by cell adhesion, migration, proliferation or differentiation studies that bone will grow in the denser scaffolds, they do have a composition, pore size and porosity consistent with those previously demonstrated to be suitable for bone growth. The mineral distribution was homogeneous through the thickness of the walls. The dry densities of the scaffolds were higher than the slurry densities due to the bound water content of the collagen [56, 154, 155]. All the scaffolds except the 4× had almost equiaxed pores but with increasing pore size through the depth of the scaffold, with the largest pores at the bottom of the scaffold for all the relative densities. During freeze drying the solidification front starts at the

bottom (near to the cooling plate on the base) and moves slowly towards the top due to the low thermal conductivity of polysulfone. Hence the coarsening time for the ice crystallites in the top layer was less than that for those at the bottom, near the cooling shelf, giving smaller pores at the top than at the bottom. The 4× scaffold had large elliptical pores through the thickness of the scaffold sheet giving a layered structure in that plane. This is due to the alignment of the collagen fibers in the plane of the scaffold as the densification increased during vacuum filtration, ultimately blocking the solvent filtration at ~ 4.5× (Figure 3.2).

3.5 Conclusions

50 wt.% MCG scaffolds with four different relative densities (0.045, 0.098, 0.137, and 0.187) were fabricated via a three step process: (1) titrant-free triple co-precipitation of the slurry, (2) vacuum filtering the slurry to the desired density, and (3) freeze drying the slurry to obtain the dry scaffold. The MCG scaffolds had an open cell pore structure with both walls and struts and interconnected pores. While we have not definitively demonstrated by cell adhesion, migration, proliferation or differentiation studies that bone will grow in the denser scaffolds, they do have a composition, pore size and porosity consistent with those previously demonstrated to be suitable for bone growth. As the relative density of the scaffolds increased, the average pore size decreased and wall thickness remained same. Pores varied from equiaxed to elliptical (in the planes perpendicular to the plane of the scaffold sheet) as the relative density of the scaffold increased. The densest scaffold (4×) had a layered structure (in the plane of the scaffold

sheet) with occasional struts across the layers making it mechanically weaker for loading in the z direction.

Compressive stress-strain plots of the scaffolds indicated distinct linear elastic, collapse plateau and densification regimes. Mechanical properties of the scaffold increased with increasing relative density. The Young's modulus and crushing strength of the scaffolds in the dry state ranged from 780 to 6500 kPa and from 39 to 275 kPa, respectively. In the hydrated state, the Young's modulus and crushing strength of the scaffolds ranged from 6.44 to 34.8 kPa and from 0.55 to 2.12 kPa, respectively. The density dependence of the Young's modulus and crushing strength were well described by cellular solids models. Specific cross-linking treatments increased the mechanical properties of the scaffolds in the hydrated state by several fold. Future research is directed towards increasing the mechanical properties of the unmineralized collagen-GAG scaffolds by increasing the relative densities of the scaffolds through vacuum filtering. These scaffolds have potential for regeneration of tissues such as cartilage, ligament, and tendon.

CHAPTER 4. Microstructure, Mechanical, and Cell Adhesion Properties of Collagen-Glycosaminoglycan Scaffolds with Increased Relative Density

4.1 Introduction

Scaffolds for tissue engineering serve as analogs of extracellular matrices that physically support cells and affect biological processes such as cell migration, differentiation, and proliferation. Scaffolds have been extensively used *in-vitro* to study cell-scaffold interactions and *in-vivo* for tissue and organ repair and regeneration. The cellular response and the success in regenerating the host tissue are affected by the scaffold microstructure [4, 5, 24, 64, 66], composition [163, 164], and mechanical properties (especially Young's modulus) [4, 17, 26, 64, 165-168]. Relevant microstructural properties include the pore size, the pore interconnectivity, and the relative density (the density of the cellular solid, ρ^*, divided by that of the solid from which it is made, ρ_S). Note that relative density is 1-porosity. Recently, Engler *et al.* [26] showed that human mesenchymal stem cells (MSC) differentiate into specific lineage and commit to phenotypes (neurogenic, myogenic, and osteogenic) depending on the matrix elasticity. Scaffold mechanical properties are also critical from an implementation point of view as the scaffold has to maintain its shape and size during surgical procedures [100]. Scaffolds

are usually made of either synthetic polymers (such as polylactic acid, polyglycolic acid) or natural polymers (such as collagen, proteoglycans). We use a collagen-glycosaminoglycan (CG) scaffold that has been studied for use in a variety of tissue engineering applications including skin [5, 22, 61], peripheral nerve [24, 31, 67, 143], muscle [169], cartilage, and bone [69, 74-76, 110]. Collagen is a significant constituent of natural extracellular matrices (ECM), possesses low antigenicity, and promotes cell attachment and proliferation [24]. Additionally, CG scaffolds are biocompatible, with non-toxic degradation products. They have a high porosity (> 90%), and interconnected pore network [68]. These characteristics make CG-based scaffolds attractive for use in tissue engineering applications. Unmineralzied CG scaffolds for skin, nerve, and cartilage regeneration are fabricated by freeze drying a CG suspension [22, 61] while mineralized CG scaffolds for the regeneration of bone are fabricated by freeze drying a triple co-precipitate of collagen, glycosaminoglycan, and calcium phosphate [69, 74-76, 103, 152].

There is interest in using collagen-based scaffolds to regenerate tendon and ligament [170-176]. The main function of ligaments and tendons is to transmit tensile loads [177]. Currently, if the damage is limited, the damaged tissue is surgically removed and the remaining tissue is reattached by suturing. If the damage is more extensive, treatment methods include: tissue grafts (such as bone-patellar tendon-bone, quadruple-strand semitendinosus and gracilis tendons, Achilles tendon, Flexor digitorum longus tendon, and fascia lata [177-179]) and synthetic grafts (such as carbon fiber graft, bundled polytetrafluoroethylene fibers, Dacron, polypropylene [180-182]). Grafts are fixed to the defect site through screws (metal or absorbable polymers) [182], suture anchors (such as

Nitinol, coated braided polyester, monofilament nylon, monofilament polypropylene, biodegradable poly-L-lactide) [183], staples [182], or cross-pins and titanium buttons [177]. The aim of the fixation of grafts is to provide sufficient initial stiffness and strength of the graft-bone interface at the attachment site such that appropriate stability can be achieved. Although initial pull-out strength of the fixation may be adequate, it has been shown that partial pull-out can occur during submaximal cyclic loading [184]. Therefore, in tendon and ligament repair, mechanical properties of the scaffold need to be closer to that of the host tissue, as early rehabilitation and physiotherapy are required to prevent joint stiffness after orthopedic surgery [178, 180].

The mechanical properties of current CG scaffolds are low. Typical CG scaffolds (ρ^*/ρ_S = 0.006) have compressive Young's modulus, E^*, of ~30 kPa (dry) and ~208 Pa (hydrated), and compressive strengths, σ^*_{el}, of ~5 kPa (dry) and ~21 Pa (hydrated) [17]. They have a uniform microstructure with roughly equiaxed pores (pore size 96 – 151 μm) [68]. The moduli and compressive strength of the scaffolds, which can be modeled as foams, are expected to increase with the square of the relative density [95]. Previous attempts to increase the mechanical properties have focused on mixing higher volume fractions of collagen and glycosaminoglycan into slurry prior to freeze drying, to increase the relative density of the scaffold. The increased viscosity of the slurry makes it more difficult to mix, however, giving an inhomogeneous CG scaffold. For ρ^*/ρ_S = 0.018 the maximum compressive Young's modulus and compressive strength in the dry state were ~80 kPa and ~15 kPa respectively [17]. Note that tripling the relative density tripled E^* and σ^*_{el}, rather than an increase of a factor of 9 as expected from the micromechanical models of

cellular materials [95]. The mechanical properties of the CG scaffolds are much lower than those of tissues such as tendon and ligament (Table 1.5) [185, 186]. Even if some of the load is carried by a surgical suture used in conjunction with the scaffolds, the mechanical properties of the CG scaffolds need to be greatly improved to meet the mechanical requirements.

We have previously characterized the microstructure and mechanical properties of mineralized CG scaffolds with varying mineral content and relative density [103, 152]. It was found, somewhat unexpectedly, that higher mineral content introduced defects such as cracked and disconnected pore walls into the scaffold, which resulted in a net decrease in the scaffold mechanical properties. We found we could produce a higher density mineralized scaffold by starting out with the low-density slurry and suctioning off solvent using vacuum. The resulting scaffolds were up to 3 times as dense as the initial ones, with mechanical properties about 9 times that of the original scaffold, a square relationship as expected from models for cellular solids.

In this paper we applied the same modified vacuum filtration process described above to unmineralized CG scaffolds to increase their relative density. The measured mechanical properties of the unmineralized CG scaffolds are compared with models for cellular solids. Models for cellular solids also suggest that the surface area per unit volume (and hence the number of binding sites per unit volume) increase with square root of the relative density and with the inverse of the pore size [66]. Therefore we completed our study by measuring the cell attachment on CG scaffolds of increasing relative density.

4.2 Materials and methods

Fabrication of CG suspension

A collagen-glycosaminoglycan suspension was fabricated using microfibrillar, type I collagen isolated from bovine dermis (Devro Pty Ltd, Bathurst, NSW, Australia), chondroitin-6-sulfate (GAG) isolated from shark cartilage (Sigma-Aldrich Chemical Co., St. Louis, MO), and 0.05 M glacial acetic acid (*pH* 3.2) (Mallinckrodt Chemical Co., Paris, KY). The suspension was prepared by combining collagen (0.019 wt.%) and GAG (0.002 wt.%), in a solution of 0.05 M acetic acid (*pH* 3.2) through a method described elsewhere [22, 61, 66, 68]. Briefly, the collagen, chondroitin-6-sulfate, and acetic acid were mixed at 15,000 rpm in an overhead blender (IKA Works Inc., Wilmington, NC); the temperature of the suspension was maintained at 4°C throughout mixing by a cooling system (Brinkman, Westbury, CT) to prevent denaturation of the collagen fibers as a result of the heat generated by mixing. The CG co-precipitate within the slurry had a density of 0.0054 grams per ml of slurry (denoted 0.0054 g ml^{-1}).

Densification of the CG slurry

The above slurry (denoted as 1×, where 1× = 0.0054 g ml^{-1}) was densified using a similar set-up as was used for the mineralized CG scaffolds in our previous work [152]. However, a vibrating base plate was used in the current set-up (Figure 4.1) in an attempt to avoid layering of the scaffold as was seen in the mineralized scaffold [152]. A cylindrical polysulfone mold (McMaster Carr Supplies, Dayton NJ), with a diameter of 5.7 cm, was perforated at the base with holes of 1 mm diameter for filtering the solvent to the aluminum base. Two filter papers with 5 μm pore diameter (VWR, West Chester,

PA) were placed at the base of the mold in order to filter out desired amount of the solvent.

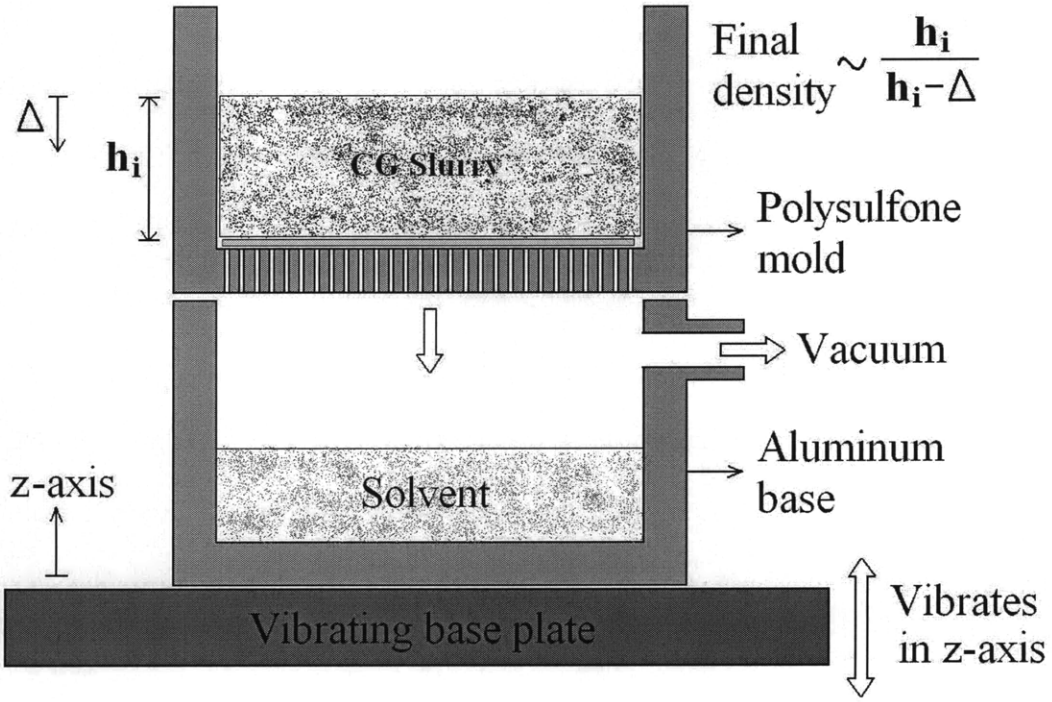

Figure 4.1. Schematic of the vacuum filtering process. The initial low density slurry is densified via vacuum suctioning the solvent to the bottom container. The final density of the slurry is controlled by the time the slurry is subjected to vacuum. Note that we have used a vibrating plate at the base in order to prevent layering of the scaffold (as was noticed in our previous work on mineralized scaffolds).

The 1× slurry was poured into the mold and subjected to vacuum as shown in the schematic (Figure 4.1). The extracted solvent was collected in the bottom container; the slurry remaining in the top compartment became denser as the time the suspension was subjected to vacuum increased. The density of the remaining slurry in the top

compartment was calculated by dividing the initial solid weight by the remaining volume of the slurry (or in other words × = h/(h-Δ) where h and (h-Δ) were the initial thickness of the 1× slurry and the final thickness of the densified slurry, respectively). The slurry density was plotted against the time it was subjected to vacuum, as shown in Figure 4.2. For a desired final slurry density the initial slurry can be filtered under vacuum for a specific time according to this plot. For this study the CG slurry was densified to three nominal higher densities of the co-precipitate within the slurry: 2× (0.0108 g ml^{-1}), 3× (0.0162 g ml^{-1}), and 4× (0.0216 g ml^{-1}).

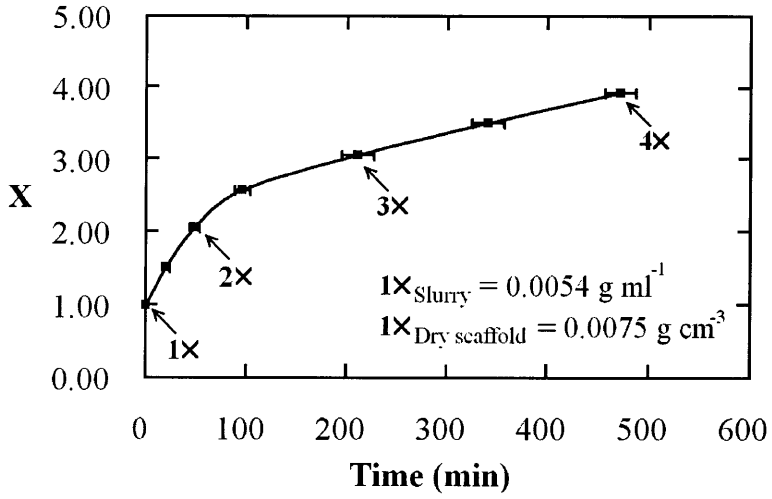

Figure 4.2. Densification vs. time for an input of 50 ml CG slurry is shown. The starting density was 0.0054 g of CG co-precipitate per 1 ml of slurry which corresponds to a dry scaffold density of 0.0076 ± 0.001 g cm^{-3}.

Fabrication of CG scaffolds using freeze-drying

Scaffolds with four nominal densities (1×, 2×, 3×, and 4×) were fabricated through freeze-drying. All the suspensions, 1×, 2×, 3×, and 4×, were freeze-dried in the

cylindrical polysulfone molds (r- and z-axis are the radial and through-thickness directions, respectively) in which they were subjected to vacuum because it was difficult to transfer the densified slurry to another mold without disturbing the homogeneity of the slurry (Figs. 1 and 3). The molds were placed in a freeze-drier at room temperature, and then freeze-dried as described elsewhere [17, 66, 68, 74, 111]. Briefly, the CG suspension was cooled to -10°C at a cooling rate of 0.1°C min^{-1} and kept at that temperature for 6 hours for the suspension to completely freeze. Heat transfer was primarily in the through-thickness or z-direction. The frozen suspension was then sublimated at 25°C under vacuum for 48 hours to obtain the dry scaffold.

Cross-linking of the CG scaffolds

Dehydrothermal treatment (DHT) was used to cross-link the scaffolds. The parameters for the DHT treatment were guided by previous work on CG scaffolds [17, 22, 69, 76, 110]. Briefly, the freeze-dried scaffold was placed under vacuum (30 mTorr) at a temperature of 105°C for 24 hr.

Microstructural characterization of the CG scaffolds

Relative density of the CG scaffolds, ρ^*/ρ_S, was calculated from the measured dry density of the CG scaffold (ρ^*) and the known dry density of solid collagen (ρ_S = 1.3 g cm^{-3}) [22, 116]. The contribution of GAG was not considered, as the amount of GAG was much less than that of the collagen. The mean pore diameter of the scaffold, D, on different $r\theta$ and θz planes (Figure 4.3) was measured using the mean intercept method. D for a particular plane is the average of the major and minor axes of the best-fit ellipse on that plane [66, 103]. The ratio of the minor to the major axes of the best-fit ellipse gives the

pore anisotropy ratio, R, on that plane [66, 103]. The average wall thickness, t, was calculated using Euclidean distance mapping from the 2D images of the scaffolds on different planes [153]. Briefly, six rectangular specimens with dimensions 5 × 5 × 5 mm were cut from different locations (for each plane: θz, $r\theta$; and for each of the 4 densities) and were embedded in glycolmythacrylate (Polysciences Inc., Warrington, PA). The embedded specimens were cut into 5 μm-thick sections (5 sections from each rectangular specimen) at various depths along the plane of analysis using a Leica RM2165 microtome (Mannheim, Germany). The sectioned films were stained with Aniline-Blue (Polysciences Inc., Warrington, PA) and observed under an inverted optical microscope (Nikon Optiphot, Japan) at 40× magnification. Images were obtained using a CCD color video camera (Optronics Engineering, Inc., Goleta, GA), and image analysis was conducted using Scion Image analysis software (Scion Corporation, Frederick, MD). Scanning electron microscopy (Leo VP438 SEM Leo Electron Microscopy Inc., Thornwood, NY) was used to study the pore structure of the scaffolds. Specimens were mounted on an aluminum holder; the specimens were not gold coated. The backscattered electron detector was used under variable pressure mode to obtain the images.

Mechanical characterization of the CG scaffolds

Compressive stress-strain curves for the dry scaffolds were measured for loading in the z-direction using a Zwick/Roell Z2.5 static materials tester (Zwick GmbH & Co., Ulm, Germany). For each density of scaffold, six cylindrical specimens, 5 mm in diameter and 5 mm thick, were cut using biopsy punches (Miltex Inc., York, PA) at different locations in the scaffold along the through-thickness direction (z-axis). All of the specimens were compressed at a uniform strain rate of 0.002 sec^{-1} up to a maximum strain of 0.80.

Tensile stress-strain curves for the dry scaffolds were measured for loading along the plane of the scaffold sheet (plane $r\theta$ in Figure 4.3) using the Zwick/Roell Z2.5 static materials tester. For each density of scaffold, six rectangular (width: 5 mm, thickness: ~3 mm, and gauge length: ~ 5 mm) specimens were cut from the plane of the sheet of the scaffold. All the specimens were stretched at a uniform strain rate of 0.002 sec^{-1} up to failure. The Young's modulus of the dry CG solid making up the scaffold, E_S, was previously measured via bending of individual scaffold struts using an atomic force microscope as described by Harley *et a.l* [17, 103, 121, 122, 152]: E_S = 762 MPa.

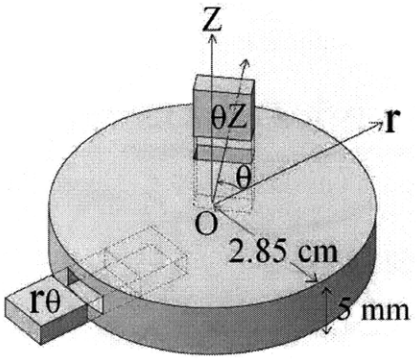

Figure 4.3. Scaffold geometries for the 1×, 2×, 3×, and 4× scaffolds. Rectangular specimens were cut out of these scaffolds from different planes (as shown above) for pore size analysis. Plane of the scaffold sheet is normal to the z-axis.

Cell attachment on the CG scaffolds

Six cylindrical samples with diameter of 6 mm and thickness of 5 mm were cut from each of the four CG scaffold variants (1×, 2×, 3×, and 4×) using biopsy punches. MC3T3-E1 mouse clonal osteogenic cells (ATCC, Manassas, VA) were maintained in MEM-α medium supplemented with 10% fetal bovine serum (FBS) (Invitrogen, Chicago, IL). MC3T3 cells were chosen for this study for comparison with the results of O'Brien *et al.*

[66], who also used MC3T3 cells. Cells were removed from the cultured flasks (VWR, Edison, NJ) to seed the scaffolds using a trypsin-EDTA solution (ATCC, Manassas, VA). Viable cell number was determined prior to seeding by live-cell staining using 0.4% Trypan Blue (Invitrogen, Chicago, IL) and counting viable cells with a standard hemocytometer (Bright-Line, Hausser Scientific, Horsham, PA) [18]. Prior to seeding, the scaffolds were placed into wells of a 6-well tissue culture ultra low attachment agarose coated plate (Corning Inc., Corning, NY). The CG scaffolds were hydrated with 10% phosphate buffered saline, PBS, (VWR, Edison, NJ) for 12 hr under vacuum followed by hydrating with the MEM-α medium supplemented with 10% FBS for another 12 hr under vacuum. CG scaffolds were removed from the medium and partially dried using a filter paper. The CG scaffolds were seeded on both sides with 2.5×10^5 cells in a manner that has previously been described [18, 167]. 10 μl of the MC3T3-E1 cell suspension (1.25×10^4 cells/μl) was pipetted onto one surface of the dry scaffold. The scaffolds were then placed inside an incubator for 30 min to allow for initial cell attachment through that surface. The seeded scaffolds were then turned over and an additional 10 μl of the cell suspension was pipetted onto the reverse surface of the scaffold. The scaffolds were then returned to the incubator for additional 30 min to allow for initial cell attachment through the reverse surface. The wells were then filled with 3ml of the MEM-α medium (supplemented with 10% FBS) and placed into a cell culture incubator and maintained at 37°C with 5% CO_2 for 24 hr. The relatively high cell density was chosen to provide a high density of integrins (cells) to allow a test of the hypothesis that the density of available ligands increases with increased relative density and decreased pore size as described below (Eq (4.4)). The attachment time of 24 hr was

selected based on a previous study by O'Brien *et al.* [66] who found that there was no significant difference in the percentage of cells attaching to the CG scaffold after 24 hr and 48 hr post seeding (using MC3T3-E1 mouse clonal osteogenic cells). Following each adhesion experiment, the seeded scaffold was removed from the tissue culture plate. Each sample was rinsed with 10% PBS at 37°C to remove unattached cells and was then placed in a 2.0 U/ml solution of dispase (Invitrogen, Chicago, IL) for 15 min to digest the scaffold [18, 167]. The number of attached, viable cells was then counted using a hemocytometer.

Cellular Solids Model of the CG scaffolds

The relative density of the scaffold can be related to the ratio of edge thickness, t, to the average pore diameter, D, using a polyhedral unit cell model [95, 152]. In the literature a tetrakaidecahedral unit cell (Figure 3.5) (a fourteen-sided polyhedron that packs to fill space) has been used to model the geometry of CG scaffolds [66]. Here we have used the same unit cell to model the CG scaffolds. The relative density of a low density open cell foam modeled with the tetrakaidecahedral unit cell is given as [152]:

$$\frac{\rho^*}{\rho_s} = 8.19\left(\frac{t}{D}\right)^2 \tag{4.1}$$

From eqn (1) it is evident that the increase in relative density, ρ^*/ρ_s, of a scaffold results in either increase in the strut thickness, t, or decrease in the pore diameter, D, or both.

For an open-cell tetrakaidecahedral unit cell with edges of circular cross-section, the surface area per unit volume (SA/V), or specific surface area can be described by the relation [66, 95]:

$$\frac{SA}{V} = \frac{3.65}{l}\left(\frac{\rho^*}{\rho_s}\right)^{1/2} \tag{4.2}$$

where l is the edge length of the tetrakaidecahedral unit cell. Edge length, l, can be related to the average pore diameter, D, by [66, 95]:

$$D = 2.78l \tag{4.3}$$

Therefore the specific surface area of the unit cell is calculated using Eq(4.2) and (4.3) as:

$$\frac{SA}{V} = \frac{10.15}{D}\left(\frac{\rho^*}{\rho_s}\right)^{1/2} \tag{4.4}$$

Specific surface area of the CG scaffold can be calculated by measuring the relative density (ρ^*/ρ_S) and the average pore diameter (D).

The mechanical properties of foams (Young's modulus, E^*, and elastic compressive strength, σ^*_{el}) depend on their relative density (ρ^*/ρ_S), the properties of the solid of which the cellular solid is made (such as Young's modulus, E_s) and the cell geometry (e.g., open- or closed-cells) [17, 95, 103]. Simple relationships between overall foam mechanical properties (Young's modulus, E^*, and elastic compressive strength, σ^*_{el}), and the relative density and solid cell wall properties can be derived using dimensional analysis [95]. Key relationships for the Young's modulus, E^*, and elastic buckling compressive strength, σ^*_{el}, for open-cell foams that are relevant for mechanical characterization of the CG scaffolds are given below:

$$\frac{E^*}{E_s} = C_1 \left(\frac{\rho^*}{\rho_s} \right)^2 \tag{4.5}$$

$$\frac{\sigma_{el}^*}{E_S} = C_2 \left(\frac{\rho^*}{\rho_s} \right)^2 \tag{4.6}$$

where C_1 and C_2 are empirical constants derived by comparing data for a variety of open cell foams. Both E^*, and σ^*_{el}, vary with the square of the relative density so that the strain at which cells collapse by bucking, ε^*_{el}, remains constant and equal to C_2/ C_1. C_1 and C_2 are empirically determined to be 1 and 0.05 respectively, for open-cell engineering foams.

Statistical analysis

One-way analysis of variance (ANOVA) and Fisher's protected least significant difference (Fisher's PLSD) methods were used to determine statistical significance between different sets of data and pair wise data sets, respectively. A probability value of 95% ($p < 0.05$) was used to determine the significance. All the measurements are reported as mean ± standard deviation. The symbols *, **, and *** indicates statistically significantly different results.

4.3 Results

Microstructural characterization

The measured overall scaffold dry densities (ρ^*) for the CG scaffolds are listed in Table 4.1. The starting densities of the co-precipitate in the slurry were less than the dry scaffold densities (for example: for the 1× scaffold, 0.0054 g ml^{-1} and 0.0076 g cm^{-3} are the slurry and dry densities respectively) partly because some of the solvent was soaked

into the collagen reducing the solidified solvent volume (and hence increasing the dry density) [56, 154, 155]. This was also observed in previous work on umineralized CG scaffolds [17] and mineralized CG scaffolds [103, 152]. The relative densities are calculated as described above and are also listed in Table 4.1. As expected, the relative densities of the 2×, 3×, and 4× scaffolds were roughly two, three, and four times that of the 1× scaffold, respectively.

Scaffold	ρ^* (g cm^{-3})	ρ^*/ρ_s	D_{avg} (μm)	t_{avg} (μm)
1X	0.0076 ± 0.0010	0.0062 ± 0.0008	343 ± 61	11.9 ± 0.57
2X	0.0153 ± 0.0020	0.0120 ± 0.0016	279 ± 70 *	13.1 ± 1.66 *
3X	0.0257 ± 0.0018	0.0198 ± 0.0014	258 ± 54 **	14.1 ± 2.27 **
4X	0.0311 ± 0.0040	0.0239 ± 0.0021	257 ± 57 **	15.6 ± 2.88 ***

Table 4.1. Dry densities (ρ^*), relative densities (ρ^*/ρ_s), average pore diameters (D), and average wall thicknesses (t) for the 1×, 2×, 3×, and 4× CG scaffolds.

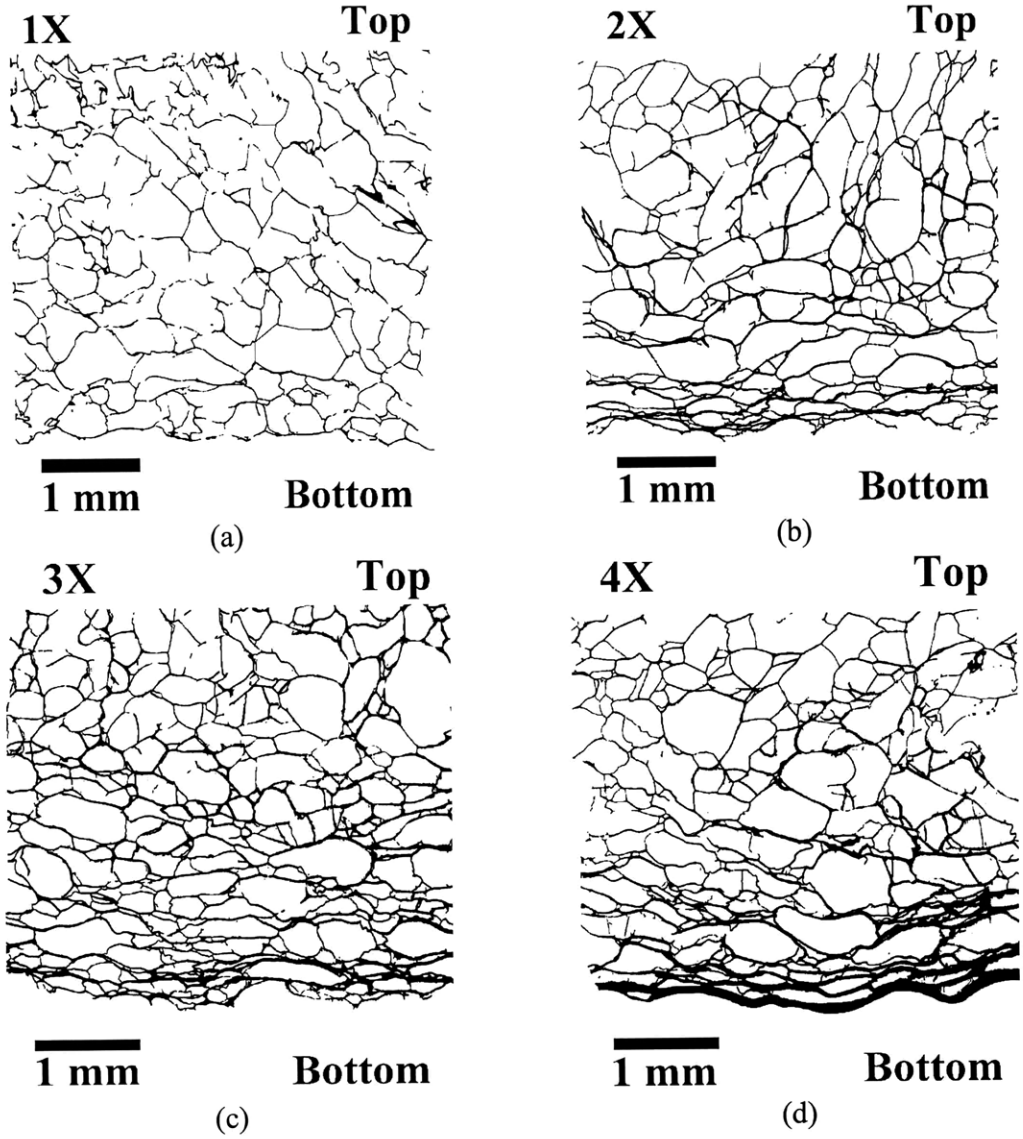

Figure 4.4. Optical micrographs of thin sections of the embedded CG scaffolds in the θz planes: (a) 1×, (b) 2×, (c) 3×, and (d) 4×.

Optical images of embedded specimens in the *θz* planes, through the thickness of the scaffold sheet, are shown in Figure 4.4. Figure 4.4 indicates that pores in the bulk of the scaffolds were roughly equiaxed for all densities, while the pores towards the bottom of the scaffolds were more elliptical at higher densities. This was expected as vacuum was applied at the bottom of the slurry which formed a boundary layer that prohibited further

densification. The strut thickness appeared thicker with increasing relative density. SEM micrographs of scaffolds showing the plane through the thickness (images taken along the planes containing the z-axis) are shown in Figure 4.5a, b, c, d. All the scaffolds exhibited low density open cell structure with mostly struts and some thin walls; the occurrence of walls increased with increasing relative density. This is expected as with increasing density more material is available to form walls as well as struts.

The average pore diameter, D, and the average wall thickness, t, for different relative densities are also listed in Table 4.1. The average pore diameter and wall thicknesses were calculated by averaging all the measured values (on planes $r\theta$ and θz). Average pore diameter decreased (except 4× which was statistically equivalent to 3×) and average wall thickness roughly remained constant with increasing relative density of the scaffold. The relative density is plotted against t/D in Figure 4.6. The curve plotted on Figure 4.6 corresponds to the theory (Eq (4.1)) indicating that the scaffold behaves very much like an open cell foam with slightly different constants that reflect that the geometry of the scaffold is more complex than an array of identical tetrakaidecahedral cells [95, 138, 139]. More detailed data for the pore diameter, D, and the anisotropy ratio, R, on different planes are listed in Table 4.2. All the scaffolds had roughly equiaxed pores with higher anisotropy ratio, R, on the θz plane (through the thickness of the scaffold). The pore sizes were slightly different in the two planes, $r\theta$ and θz. However, as noted above, in the through thickness direction (plane θz), as the density increased, the pores towards the bottom of the scaffold were more elliptical, decreasing the overall R.

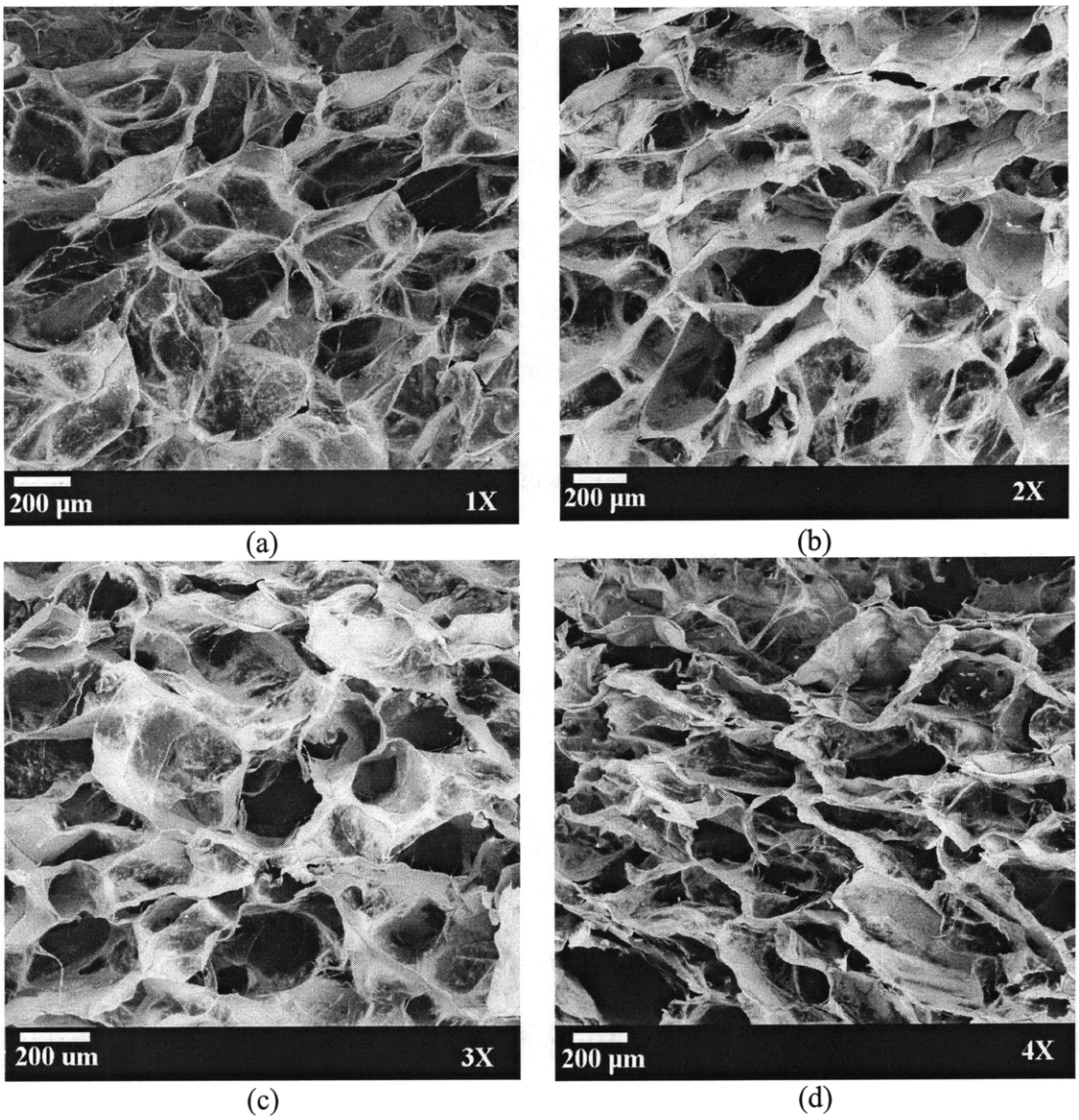

Figure 4.5. SEM micrographs of the CG scaffolds: (a) 1×, (b) 2×, (c) 3×, and (d) 4×.

Scaffold	Plane	D (μm)	R
1X	θz	365 ± 58	0.750 ± 0.089
	$r\theta$	306 ± 48*	0.856 ± 0.058*
2X	θz	246 ± 52	0.738 ±0.109
	$r\theta$	308 ± 71*	0.835 ± 0.075*
3X	θz	219 ± 46	0.761 ± 0.118
	$r\theta$	285 ± 42*	0.804 ± 0.086
4X	θz	268 ± 62	0.676 ± 0.124
	$r\theta$	244 ± 48*	0.803 ± 0.114*

Table 4.2. Pore sizes (D) and anisotropy ratios (R) measured on different planes of the MCG scaffolds.

Mechanical characterization

Compressive stress-strain plots for loading dry, DHT cross-linked scaffolds in the z-direction are shown in Figure 4.7. Distinct linear elastic, collapse plateau and densification regimes were observed for all the scaffolds indicating behavior similar to that of foams [95]. Elastic modulus (E^*), elastic compressive strength (σ^*_{el}), elastic compressive strain (ε^*_{el}), and collapse modulus ($\Delta\sigma/\Delta\varepsilon$) are measured from the stress-strain curves [95, 103]. Briefly, E^* is the slope of the linear elastic regime, $\Delta\sigma/\Delta\varepsilon$ is the slope of the collapse regime, σ^*_{el} and ε^*_{el} are the point of transition from linear to the collapse regime (determined from the intersection of the E^* and $\Delta\sigma/\Delta\varepsilon$ regression lines). The values of E^*, σ^*_{el}, ε^*_{el} and $\Delta\sigma/\Delta\varepsilon$ for the scaffolds in the DHT cross-linked dry state are listed in Table 4.3. E^*, σ^*, $\Delta\sigma/\Delta\varepsilon$ increase with increase in relative density of the scaffold from 1× to 4×. ε^*_{el} roughly remains constant for different relative densities ($\varepsilon^*_{el} \sim C_2/C_1 \sim 17\%$) as predicted by Eq (2.4) and (4.6). Therefore we have used C_1 and C_2 to be

1 and 0.15 respectively in our analysis. $\Delta\sigma/\Delta\varepsilon$ is in the same order as that of the E^*. The data for the relative modulus (E^*/E_s) and the relative elastic compressive strength (σ^*_{el}/E_s) for the scaffolds are plotted against relative density (ρ^*/ρ_S) in Figure 4.8. The best-fit curves through the data for the relative modulus ($R^2 = 0.996$) and for the relative strength ($R^2 = 0.958$) are:

$$\frac{E^*}{E_s} = 0.006\left(\frac{\rho^*}{\rho_s}\right)^{0.98} \tag{4.7}$$

$$\frac{\sigma^*_{el}}{E_S} = 0.0009\left(\frac{\rho^*}{\rho_s}\right)^{0.94} \tag{4.8}$$

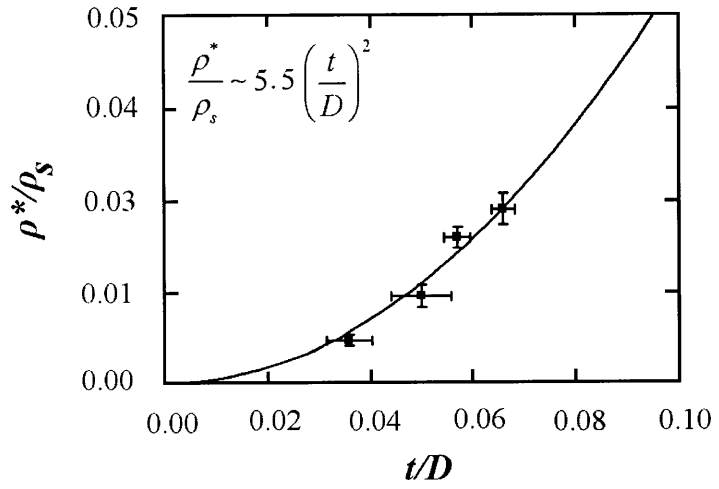

Figure 4.6. The relative density, ρ^*/ρ_s, plotted against the ratio of the wall thickness to the pore diameter, t/D, for the CG scaffolds.

E^*/E_s and σ^*_{el}/E_s vary roughly linearly with ρ^*/ρ_S while cellular solids model predicts a square relationship (Eq (2.4) and (4.6)). Data from Harley *et al.* [17] for relative modulus and the relative elastic compressive strength are also plotted against respective relative

densities in Figure 4.8. Their data also varied linearly with relative density and is similar to the data of this study.

Scaffold	ρ^*/ρ_s	E^* (kPa)	σ^* (kPa)	ε^* (%)	$\Delta\sigma/\Delta\varepsilon$ (kPa)	$E_{Tens}{}^*$ (kPa)
1x	0.0062 ± 0.0008	32.4 ± 6.25	5.02 ± 1.09	15.8 ± 3.52	10.6 ± 1.03	295 ± 123
2x	0.0120 ± 0.0016	60.6 ± 4.96*	11.8 ± 2.36*	18.9 ± 2.46*	43.6 ± 2.51*	810 ± 221*
3x	0.0198 ± 0.0014	97.3 ± 16.7**	15.6 ± 3.13**	15.9 ± 1.19	54.8 ± 9.25**	971 ± 202**
4x	0.0239 ± 0.0021	127 ± 23.1**	19 ± 3.93*	14.6 ± 3.45	43.3 ± 5.62**	3087 ± 488***

Table 4.3. Mechanical properties of the CG scaffolds in the DHT cross-linked dry state determined from the uniaxial compression and tension tests.

Tensile stress strain curves for loading dry, DHT cross-linked scaffolds along the plane of the scaffold sheet are shown in Figure 4.9a. The curves are typical of the tensile response of foams, with increasing stiffness with increasing strain, as the cell walls align with the direction of loading [95]. The tangent stiffness at any given strain increased with relative density. Failure occurred at the grips, and so is not characteristic of the tensile strength of the scaffold, due to the non-uniform stress state at the grips. The Young's modulus was calculated from the initial linear slope of the stress-strain curve (Table 4.3). The tensile modulus is greater than the compressive modulus. The data for the relative moduli are plotted against relative density in Figure 4.9b, along with the best-fit curve through the data ($R^2 = 0.852$):

$$\frac{E^*}{E_s} = 0.56\left(\frac{\rho^*}{\rho_s}\right)^{1.43} \tag{4.9}$$

The relative modulus-relative density relationship is closer to the squared dependence as predicted by the cellular solids model (Eq (2.4)).

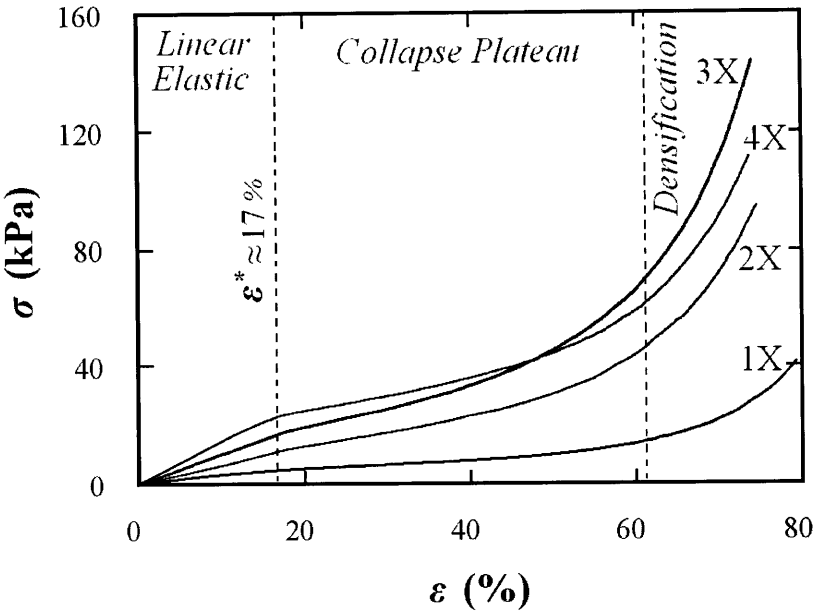

Figure 4.7. Compressive stress-strain plots for the CG scaffolds in the DHT crosslinked dry state. Distinct linear elastic, collapse plateau and densification regimes were observed for the scaffolds.

Cell attachment

The specific surface area for the scaffolds, *SA/V*, was calculated according to Eq (4.4). The percentage of viable MC3T3-E1 cells attached to the scaffolds 24 hr after seeding, *N*, is plotted against the measured specific surface area for the scaffolds in Figure 4.10. The best-fit curve through the data ($R^2 = 0.972$) is:

$$N = 8.88\frac{SA}{V} - 0.595 \tag{4.10}$$

There is a strong linear relationship between the percent cells attached and the specific surface area of the scaffolds. There was no statistical difference between the percent of cells attached to the 3× and 4× scaffolds. As described above, cells were seeded from both top and bottom surfaces. We believe that the thicker elliptical pore walls (Figure

4.4) at the bottom of the 4× scaffold acted as barrier to cell migration through that surface inhibiting cell attachment relative to that for the 3× scaffold. Data from O'Brien *et al.* [66] for percentage of viable MC3T3-E1 cells attached to the their CG scaffolds 24 hr post seeding is also plotted against the respective specific surface area for their scaffolds in Figure 4.10. The best-fit curve through their data ($R^2 = 0.954$) is:

$$N = 7.16\frac{SA}{V} - 12.6 \tag{4.11}$$

Their data also varied linearly, but, follows a different regression line that does not pass through the origin; the reason for this is not clear.

4.4 Discussion

In our previous work on mineralized CG scaffolds [152], we were able to achieve an increase in Young's modulus from 780 kPa, for the 1× dry scaffold, to 6500 kPa for the 3× dry scaffold. Similarly, we were able to achieve an increase in the crushing strength from 39 kPa, for the 1× dry scaffold, to 242 kPa for the 3× dry scaffold. The densification was achieved by vacuum filtering the 1× slurry as described above. The dependence of the relative Young's modulus and relative crushing strength on relative density were well described by the power exponents derived from cellular solids models [95]. In this work we expected a similar increase in the mechanical properties of the unmineralized CG scaffolds by increasing the relative density of the 1× CG slurry through the vacuum filtration method.

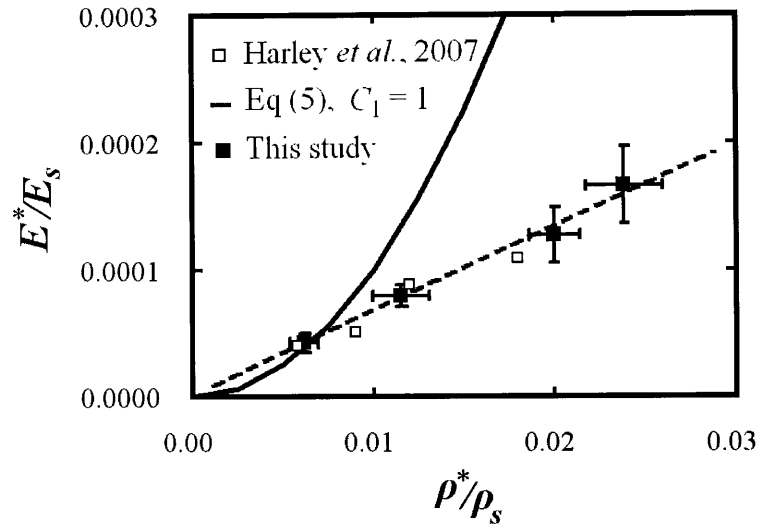

(a)

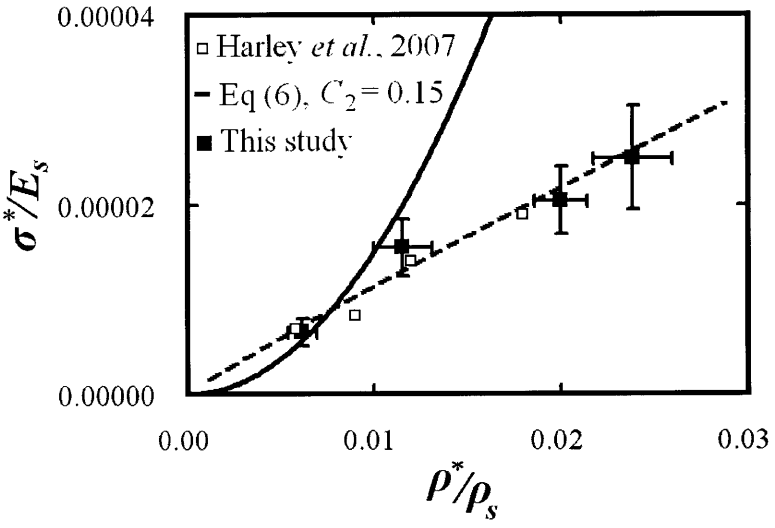

(b)

Figure 4.8. (a) Compressive E^*/E_s and (b) compressive σ^*/E_s plotted against relative density, ρ^*/ρ_s, for the dry CG scaffolds. Data obtained from Harley *et al.* [17] is also plotted for comparison.

In this work on unmineralized CG scaffolds, the compressive stress-strain curves for the scaffolds were typical of foams, showing the three regimes of linear elasticity, the collapse plateau and densification. The relative density, ρ^*/ρ_s, varied with $(t/D)^2$, suggesting an open cell microstructure of the CG scaffolds (Figure 4.6) [95]. We were

able to achieve an increase in Young's modulus from ~32 kPa, for the 1× dry scaffold, to ~127 kPa for the 4× dry scaffold. Similarly, we were able to achieve an increase in the elastic compressive strength from ~5 kPa, for the 1× dry scaffold, to ~19 kPa for the 3× dry scaffold. However, the dependence of the relative Young's modulus, E^*/E_s, and relative elastic compressive strength, σ^*_{el}/E_s, on relative density were linear (Figure 4.8) in contrast to Eq (2.4) and (4.6) which predicts a squared dependence. The model predicts E^*/E_s and σ^*/E_s well for the standard 1× scaffold ($\rho^*/\rho_s = 0.0062$), but overestimates the experimental results for the higher ρ^*/ρ_s (Figure 4.8).

Previous work on unmineralized CG scaffolds by Harley *et al.* [17] also predicted a linear relationship for E^*/E_s and σ^*_{el}/E_s. In his work, the higher density scaffolds were fabricated by blending high volume fraction slurries that resulted in microstructural heterogeneities in the scaffolds with holes as well as local regions of higher densities. These heterogeneities contributed to properties lower than that predicted by the model. One of the objectives in our current fabrications technique was to avoid these local microstructural heterogeneities by using the vacuum filtration method. While we succeeded in avoiding local heterogeneities with the current method, we revealed that as we increased the relative density of the scaffolds, the pores at the bottom became increasingly elliptical with the major axis perpendicular to the loading directions (Figure 4.4). These elliptical pores adversely affected the compressive behavior of the higher density scaffolds. Clearly, vacuum filtration of the CG slurry can achieve higher densities than that obtained by blending high volume fraction slurries as was done by Harley *et al.* (Figure 4.8).

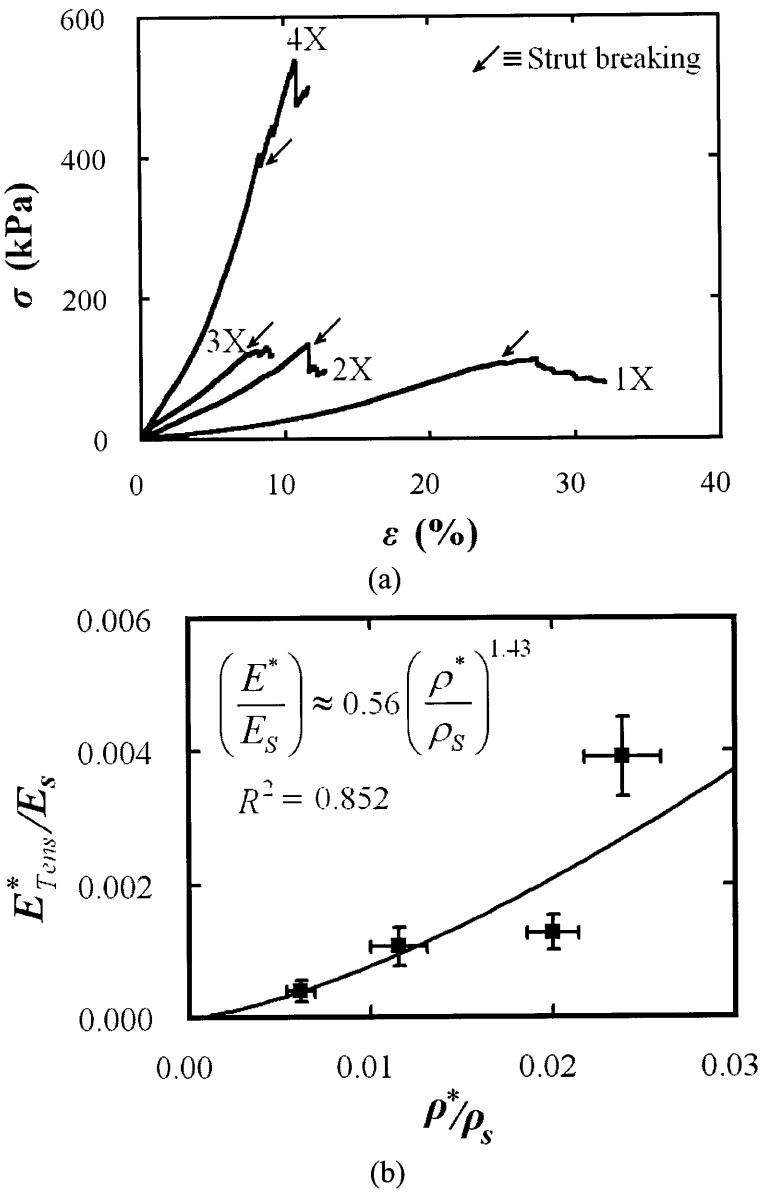

Figure 4.9. (a) Tensile stress-strain plots for the CG scaffolds in the DHT cross-linked dry state. E_{Tens}^* was calculated from the initial linear slope of the stress-strain plot for each scaffold. (b) Relative tensile modulus, E_{Tens}^*/E_s, plotted against relative density, ρ^*/ρ_s, for the DHT cross-linked dry CG scaffolds.

The tensile stress-strain behavior is consistent with those for foams: increased stiffness at higher strain as the pore struts and walls align with the direction of loading [18, 167, 187-

189]. The CG scaffolds were significantly stiffer under tension (Table 4.3), similar to previous investigations [17, 18, 187]. A mechanistic explanation of this phenomenon based upon the observation of a thin layer of higher density scaffold at the top surface of the scaffold sheets has been given by Harley *et al.* [17]. We also observed a similar thin denser layer at top of our scaffold sheets which partly explains the stiffer behavior under tension. In addition, with increasing relative density the scaffolds formed thicker pore walls and struts towards the bottom of the scaffold sheet (Figure 4.4). These thicker layers significantly increased the stiffness under tension in the plane of the scaffold sheet. The relative modulus under tension is somewhat closer to the squared dependence predicted by the cellular solids model (Figure 4.9b) as a result of the thicker pore walls in the higher density scaffolds. Even though the tensile Young's modulus (Table 4.3) is lower than those for tendon and ligament (Table 1.5), we have achieved a significant increase (~ 11×) in the properties by increasing the relative density of the scaffold.

Mechanical properties of the scaffolds in the hydrated state are critical as the scaffolds are hydrated by the body fluid soon after placed in the defective tissue site. We did not measure the hydrated properties of the CG scaffolds in this work as the effect of hydration on CG scaffolds has been well documented by Harley *et al.* [17]. Hydration decreases E^* and σ^*_{el} of the CG scaffolds by 150 and 250 times respectively. Therefore, E^* and σ^*_{el} of the hydrated CG scaffolds (1×, 2×, 3×, and 4×) can be predicted using the above factors. The Young's modulus and elastic compressive strength in the hydrated state will increase with increasing relative density from 213 Pa to 844 Pa and 20 Pa to 75 Pa, respectively. Effect of different cross-linking on the mechanical properties can also be

predicted in a similar fashion based on the results documented by Harley *et al.* on CG scaffolds [17]. The maximum Young's modulus and elastic compressive strength in the hydrated state that can be achieved through EDAC (5:2:1) cross-linking for the 4× scaffold is ~ 6 kPa and 540 Pa respectively. Note that these values are an order of magnitude higher than that of the 1× CG scaffold in hydrated state.

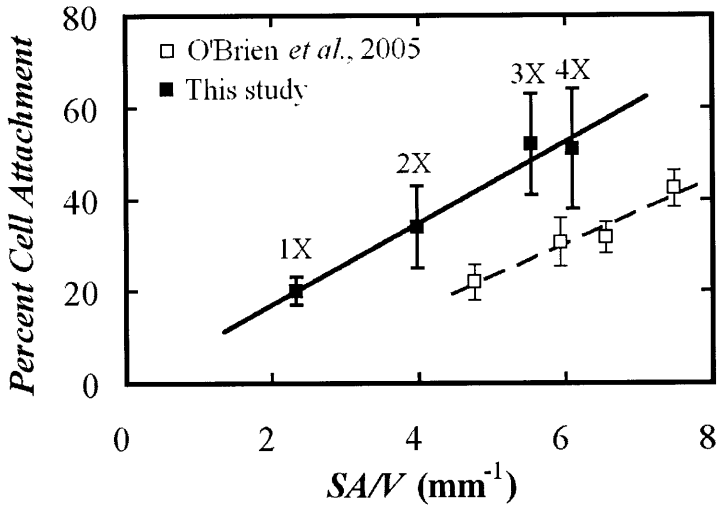

Figure 4.10. Compressive stress-strain plots for the CG scaffolds in the DHT crosslinked dry state. Distinct linear elastic, collapse plateau and densification regimes were observed for the scaffolds.

A practical upper limit on the relative density is that which limits the degree of interconnection between the pores so that cells can migrate through the scaffold; for this reason, the maximum practical relative densities is probably less than 0.25 [101, 152]. Our experimental results suggest that an increase in the relative density from our base ρ^*/ρ_s = 0.0062 (or 1×) to 0.25 should increase the Young's modulus and elastic collapse strength almost by a factor of 40. Further study is needed to develop methods of

increasing the relative density up to this limit while maintaining a homogeneous microstructure.

The scaffolds had an interconnected pore structure with mostly struts and occasional walls. All the scaffolds had average pore sizes in the range of 250-350 μm with porosities greater than 97% (Table 4.2). The dry densities of the scaffolds were higher than the slurry densities due to the bound water content of the collagen [56, 154, 155]. All the scaffolds had similar pore sizes throughout except at the bottom of the scaffold where the pores become increasingly elliptical with increase in density. This is due to the alignment of the collagen fibers in the plane of the scaffold as the densification increased during vacuum filtration.

In a previous study by O'Brien *et al.* [66], the MC3T3-E1 cell attachment was found to be inversely proportional to the average pore size of the CG scaffolds (with a constant relative density) for a pore size range of 96-151 μm. However, the relationship between cell attachment and relative density of the scaffold has not been studied before. In this study we used our CG scaffolds with four different relative densities to investigate the cell attachment behavior. The specific surface area of the scaffolds, SA/V, was estimated using a tetrakaidecahedral unit cell (Figure 3.5, Eq (4.4)). The density of ligands available for binding on each scaffold is assumed to be proportional to the scaffold specific surface area; the specific surface area is proportional to the square root of the relative density and inversely proportional to the mean pore diameter (Eq (4.4)). The estimated specific surface area of the scaffolds is remarkably consistent with the results from the cell attachment study, showing a linear relationship between the percentage of

cell attached and specific surface area (Figure 4.10, Eq (4.10)). The attached cell number increases linearly with specific surface area similar to the results by O'Brien *et al.*, [66], although with a slightly difference slope and intercept. We believe that there are three reasons for this: (1) we hydrated our scaffolds with the MEM-α medium prior to cell seeding while they used dry scaffolds, (2) we used smaller cylindrical specimens rather than the rectangular specimens used by O'Brien *et al.*, and (3) our scaffolds are made from a different collagen source compared to O'Brien *et al.* (their source was Integra LifeSciences, Plainsboro, NJ).

4.5 Conclusions

Collagen-GAG scaffolds with four different relative densities (0.0062, 0.0120, 0.0198, and 0.0239) were fabricated via a three step process: (1) coprecipitation of the CG slurry, (2) vacuum filtering the slurry to the desired density, and (3) freeze drying the slurry to obtain the dry scaffold. The CG scaffolds had an open cell pore structure with mostly struts and interconnected pores. As the relative density of the scaffolds increased, the average pore size decreased and wall thickness remained roughly constant. Pores varied from equiaxed to elliptical at the bottom (with the major axis perpendicular to the through thickness direction) as the relative density of the scaffold increased. Compressive stress-strain plots of the scaffolds indicated distinct linear elastic, collapse plateau and densification regimes. Compressive properties of the scaffold increased roughly linearly with increasing relative density in contrast to the square dependence described by cellular solids models. Young's modulus under tension was an order of magnitude higher than the compressive Young's modulus due to presence of a dense thin layer at the top of the

scaffold sheet as well as thicker walls at the bottom of the scaffold sheet with increasing relative density. The tensile relative Young's modulus increased with relative density raised to the power 1.43, somewhat less than the squared dependence predicted by the cellular solids model. A linear relationship was found between cell attachment and specific surface area, indicating that over the range of pore sizes (257–353 μm) and relative densities (0.0062-0.0239) studied short-term MC3T3 cell viability is governed by the specific surface area available for binding. Future research is directed towards increasing the mechanical properties of the unmineralized collagen-GAG scaffolds by increasing the relative densities of the scaffolds by applying external load instead of vacuum.

CHAPTER 5.Conclusions and Recommendations for Future Research

5.1 Thesis conclusions

Mechanical properties (Young's modulus and strength) of scaffolds used for tissue regeneration are critical from an implantation perspective (the scaffold should have sufficient stiffness and strength to maintain its shape and size during surgical procedures) [100, 151] as well as tissue regeneration perspective (human mesenchymal stem cells (MSC) differentiate into specific lineages and commit to phenotypes (neurogenic, myogenic, and osteogenic) depending on the substrate elasticity)[21, 25, 26, 28]. Currently collagen-based scaffolds have been approved by the United States Food and Drug Administration (FDA) for regenerating skin and nerves [24]. However, the mechanical properties of the current collagen-based scaffolds are low for use in regeneration of relatively stiffer tissues such as bone, tendon, and ligament. Therefore the goal of this thesis was to improve the mechanical properties of the collagen-based scaffolds by manipulating the current techniques for fabricating these scaffolds. The microstructure and mechanical properties of these newly developed scaffolds have been characterized.

Collagen-glycosaminoglycan (CG) scaffolds have been fabricated through freeze-drying a CG suspension. Recently, mineralized CG (MCG) scaffolds have been developed by Lynn *et al.* [69] through a titrant-free triple co-precipitation method followed by freeze-drying for bone regeneration. Bi-layer scaffolds with CG and MCG layers have been developed for cartilage-bone joint regeneration. The two types of scaffolds, CG and MCG, have been the subject of this thesis. We describe the mechanical properties of MCG scaffolds for bone regeneration in chapter 2 and 3, and CG scaffolds for tendon and ligament regeneration in chapter 4.

MCG scaffolds made by previous techniques (ρ^*/ρ_S = 0.15, and 50 wt.% mineral content) have a compressive Young's modulus, E^*, of ~762 kPa (dry), and a compressive strength, σ^*, of ~85 kPa (dry) [69]. The compressive strength is so low that the scaffold can be compressed between the thumb and fingers. From an implementation perspective the dry scaffolds should at least withstand hard thumb pressure. The hydrated properties of these scaffolds had not been characterized by Lynn *et al.* [69]. For the MCG scaffold, we set our target mechanical properties (especially Young's modulus) to be the modulus at which MSC stem cells differentiate into osteoblast-like cells: 25-40 kPa [26]. The Young's modulus of the scaffolds in the hydrated state should optimally be in this range for bone regeneration. Typical CG scaffolds (ρ^*/ρ_S = 0.006) have a compressive Young's modulus, E^*, of ~30 kPa (dry) and ~208 Pa (hydrated), and compressive strengths, σ^*_{el}, of ~5 kPa (dry) and ~21 Pa (hydrated) [17], much lower than those of tendon and ligament (E^* ~500 MPa and σ^*_{el}, of ~50 MPa). In tendon and ligament repair, it is anticipated that the scaffolds would be used in conjunction with sutures that would carry load, at least

temporarily, while the tissue is regenerated. For the CG scaffolds our target was to increase the mechanical properties as much as possible.

Models for cellular solids suggest that the overall mechanical properties (E^* and σ^*) of a foam can be increased by either increasing the mechanical properties of the solid (E_S, σ_S) from which the foam is made or by increasing the relative density, ρ^*/ρ_S, of the foam (Eqs 2.4, 2.5, 4.6). Previous studies have shown that CG scaffolds, with porous microstructure, can be mechanically modeled as foams [17, 66]. Therefore, we first attempted to increase the mechanical properties of the MCG scaffold by increasing the mechanical properties of the solid (chapter 2). Next, we attempted to increase the mechanical properties of the MCG scaffolds by increasing the relative density of the scaffold (chapter 3). Finally we attempted to increase the mechanical properties of the CG scaffolds by increasing the relative density of the scaffold (chapter 4).

MCG solid is made from the CG copolymer and a calcium phosphate mineral phase. The mechanical properties (Young's modulus and strength) of the calcium phosphate ceramic phase are much higher than that of the CG copolymer. A simple composites model suggests that the overall mechanical properties of the MCG solid can be improved by increasing the mineral content of the solid. One of the advantages of the triple co-precipitation method is that we can control the mineral phase and content by the *pH* of the solvent and molar ratios of the reactants (calcium hydroxide and calcium nitrate). We fabricated MCG scaffolds with two different mineral contents (chapter 2): 50 wt.% (as a control) and 75 wt.%. We were able to fabricate scaffolds with pore sizes between 200-350 μm, which is optimal for bone growth [20, 37, 128, 129]. The mechanical properties

of the 50 wt% MCG scaffold (control scaffold) had similar properties as that fabricated by Lynn *et al.* ($E^* \sim 780$ kPa and $\sigma^* \sim 91$ kPa). Unfortunately, the 75 wt.% MCG scaffold mechanical properties ($E^* \sim 367$ kPa and $\sigma^* \sim 35$ kPa) were lower than the 50 wt.% MCG scaffold mechanical properties. The pore microstructure revealed that there are higher fraction of disconnected pore walls and struts in the 75 wt.% scaffold compared to the 50 wt.% scaffold. It has been shown that the overall mechanical properties (Young's modulus and strength) of the foam decreases significantly with slight increase in the fraction of disconnected pore walls and struts (for example: a 10% disconnected pore walls and struts corresponds to roughly ~ 40% decrease in the Young's modulus and strength)[136]. In addition, measurement of the mechanical properties of the MCG solid for both the scaffolds also showed that the 75 wt.% solid had slightly lower Young's modulus than the 50 wt.% scaffold. Microstructural characterization showed that there are more defects in the pore walls such as voids and cracks, in the higher mineral content scaffold reducing the solid mechanical properties which in turn reduce the overall scaffold mechanical properties. X-ray analysis showed that the higher mineral content scaffold also had an undesirable mineral phase, monetite (30% of the mineral content was monetite in the 75 wt.% scaffolds compared to 100% brushite in the 50 wt.% scaffold) that reduced the mechanical properties of the solid (and in turn that of the scaffold). Apart from reduction in properties for the higher mineral content scaffold, the 50 wt.% scaffold mechanical properties did not match up to the mechanical properties predicted by cellular solids models; partly because the scaffold microstructure was not exactly like an ideal open cell foam microstructure. In addition, even though there were not as many defects as

were in the higher mineral content scaffold, there were some and the overall combined effect of these defects reduced the mechanical properties.

Next, we attempted to increase the properties of the 50 wt.% scaffold by increasing the relative density of the scaffold. An attempt to increase the relative density by increasing the solid volume fraction of the slurry did not work satisfactorily as the high viscosity slurry was difficult to mix homogeneously using an overhead blender. Then, we developed a new technique of vacuum filtering low-viscosity slurry. We fabricated 50 wt.% MCG scaffolds with four different relative densities (chapter 3) between 0.045-0.187 and pore sizes between 100-350 μm (appropriate for bone regeneration). The pore sizes decreased and wall thickness remained roughly constant with increasing relative density. The mechanical properties-relative density relationship of the MCG scaffolds followed closely to the predictions of the cellular solids model: a squared dependence of the Young's modulus and to the power 3/2 dependence of the collapse strength on relative density [95]. We were able to increase the Young's modulus and collapse strength from 780 kPa to 6.5 MPa (~9 times) and 39 kPa to 242 kPa, respectively (~ 6 times) with three times increase in the relative density. More importantly, the hydrated Young's modulus of the scaffolds increased from ~ 6 kPa to ~35 kPa. This is critical from bone regeneration point of view, because as described above, MSC stem cells differentiate into osteblast-like cells on a substrate with stiffness ranging from 25-40 kPa. The 50 wt.% MCG scaffold with a relative density of 0.137 has the Young's modulus (~35 kPa) in the optimal range for bone regeneration. In addition, the denser scaffolds

could withstand hard thumb pressure without deforming which is critical from implementation perspective as described above.

Inspired by the success of the vacuum filtration technique to improve the mechanical properties of the 50 wt.% MCG scaffold, we attempted to improve the mechanical properties of the CG scaffold using the same techcnique. There is interest in using collagen-based scaffolds to regenerate tendon and ligament [170-176]. We fabricated CG scaffolds with four different relative densities (chapter 4) between 0.045-0.187 and pore sizes between 250-350 μm. Similar to the trend noticed in the MCG scaffolds with different relative densities, pore sizes decreased and wall thickness remained roughly constant with increasing relative density. The mechanical properties-relative density relationship of the CG scaffolds followed a linear relationship in contrast to the predictions of the cellular solids model: a squared dependence [95]. We were able to increase the dry compressive Young's modulus and compressive elastic strength from 32 kPa to 127 kPa (~4 times) and 5 kPa to 19 kPa, respectively (~ 4 times) with four times increase in the relative density. Dry tensile Young's modulus increased from 295 kPa to 3.1 MPa (closely following the squared dependence as expected by the cellular solids model). Cell adhesion experiments showed a linear relationship between the fraction of cells attached to the scaffold and the measured scaffold specific surface area (calculated from the relative density and mean pore diameter) confirming the fact that fraction of viable cells attached to the scaffolds is primarily influenced by the scaffold specific surface area.

The key results of this thesis are:

- Higher mineral content decreased the overall mechanical properties of the MCG scaffolds due to defects such as disconnected pore walls, cracks and holes on the pore walls, and an undesirable mineral phase.

- Higher relative density MCG scaffolds fabricated using the vacuum filtration technique had significantly higher mechanical properties that closely followed the models for cellular solids. The pore sizes were in the right range for bone regeneration.

- Further control over mechanical properties can be achieved by cross-linking the scaffolds chemically (EDAC) or physically (DHT).

- 50 wt.% MCG scaffold with relative density of 0.137 in the hydrated state has Young's modulus of ~35 kPa that is in the optimal range of stiffness required for MSC stem cells to differentiate into osteoblast-like cells.

- Denser MCG scaffolds could withstand hard thumb pressure making them suitable from an implementation point of view where the scaffolds are often subjected to different stresses in this range during surgery.

- MCG scaffolds closely followed characteristics of cellular solids. Therefore, the mechanical properties can be further improved by increasing the relative density further beyond what we have achieved.

- Denser CG scaffolds fabricated using the above vacuum filtration technique had improved mechanical properties; however they did not follow the squared dependence as expected by the cellular solids model.

- Cell attachment increased linearly with increasing specific surface area (which increases with the square root of the relative density and inversely with the mean pore size) of the CG scaffolds. Therefore the increasing relative density not only increases the mechanical properties of the scaffold, but also improves the cell attachment characteristic of the scaffold.

5.2 Future work

Consolidation of CG and MCG slurry by application of external load

One of the disadvantages of the above vacuum filtration technique is that for denser scaffolds, the pores become increasingly elliptical (Fig. 3.6 and Fig. 4.4) and layering (Fig. 3.7) of the scaffold takes place on the side which is subjected to vacuum. As a result, denser scaffolds had a gradual pore size and shape change from the top of the scaffold to the bottom of the scaffold (vacuum was applied from the bottom). In order to fabricate a more homogeneous scaffold with uniform pore microstructure, pressure has to be applied from both the surfaces, top and bottom. We believe that by applying external load in a manner that has been applied to densify soil [190], CG slurries can be densified more homogeneously. The set-up for the load application technique is demonstrated in Figure 5.1a.

The top piston as well as the base of the mold is perforated to allow solvent filtration from both the surfaces. The whole set-up is submerged in distilled water to counter the gravitational effect which might drive solvent filtration through the bottom surface more than the top surface. For a specific load, W (corresponding to a stress of σ), the piston gradually moves down with time (t) from the initial thickness, h, ultimately saturating at a specific strain, $(\Delta/h)_c$ (Figure 5.1b). The saturation densification $(\Delta/h)_c$ for different stresses can be measured and plotted versus the stress (Figure 5.1c). Using the densification-stress plot (Figure 5.1c) the amount of load can be exactly predicted for a known densification. The time of densification can also be predicted from the (Δ/h)-t plot at that stress (Figure 5.1b).

Preliminary studies on densification of CG slurries using the above technique have been performed in our lab. A typical (Δ/h)-t plot for a CG slurry (0.0054 g ml^{-1}) at a stress of ~75 Pa is shown in Figure 5.2a. The variation of (Δ/h) with t is very similar to that obtained in densification of soil (Figure 5.1b). $(\Delta/h)_c$-σ plot for the CG scaffold is shown in Figure 5.2b. Clearly, $(\Delta/h)_c$ varies linearly with σ as expected from densification of the soil (Figure 5.1c). Further research needs to be performed to fabricate and characterize scaffolds of various densities to understand structure-property relationship of the denser scaffolds.

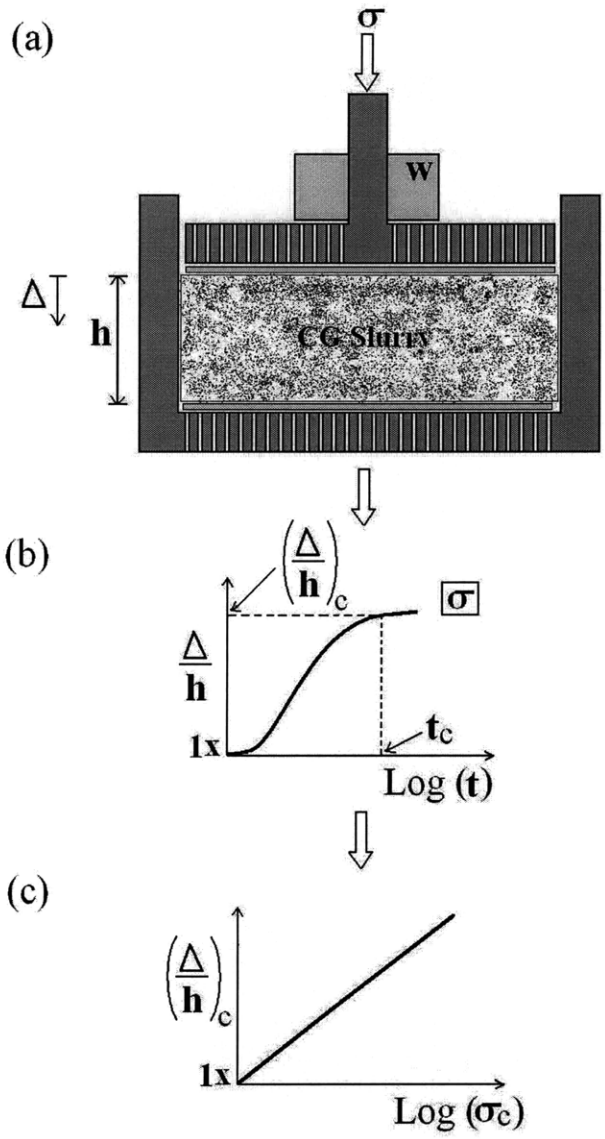

Figure 5.1. (a) Set-up for the consolidation of the CG slurry using external loads [190]. An external load, W (corresponding to a stress σ_c), is applied to the top piston that moves down from the initial slurry thickness of h. (b) The variation of the distance moved down by the top piston (Δ) versus time (t) for a specific stress (σ) is plotted. The piston saturats after a critical time (t_c). (c) The above steps can be carried out for various stresses and the saturation densification $(\Delta/h)_c$ can be plotted versus the applied stress (σ).

Fabrication of denser and higher mineral content MCG scaffolds

We observed higher fraction of defects such as disconnected pore walls, cracks and holes on pore walls for the higher mineral content MCG scaffolds (such as 75 wt.% mineral content). We believe that in the higher mineral content MCG scaffold, the fraction of CG copolymer was lower which may have contributed to the pore wall defects. Densification (using the vacuum filtration technique or the external load technique) may avoid these defects and improve the mechanical properties.

Cell adhesion, traction and contraction on MCG scaffolds

We fabricated 50 wt.% MCG scaffolds with higher relative densitites using the vacuum filtration technique. However, the cell adhesion properties of these scaffolds were not measured. For final application of this higher density MCG scaffolds at the osteochondral defect sites, cell (osteogenic cells such as MC3T3 cells) adhesion, traction, and contraction in the scaffolds are critical. Therefore, MC3T3 osteogenic cells can be seeded to these scaffolds with different pore sizes, densitites, and mineral contents, and cell-matrix interaction can be studied subsequently.

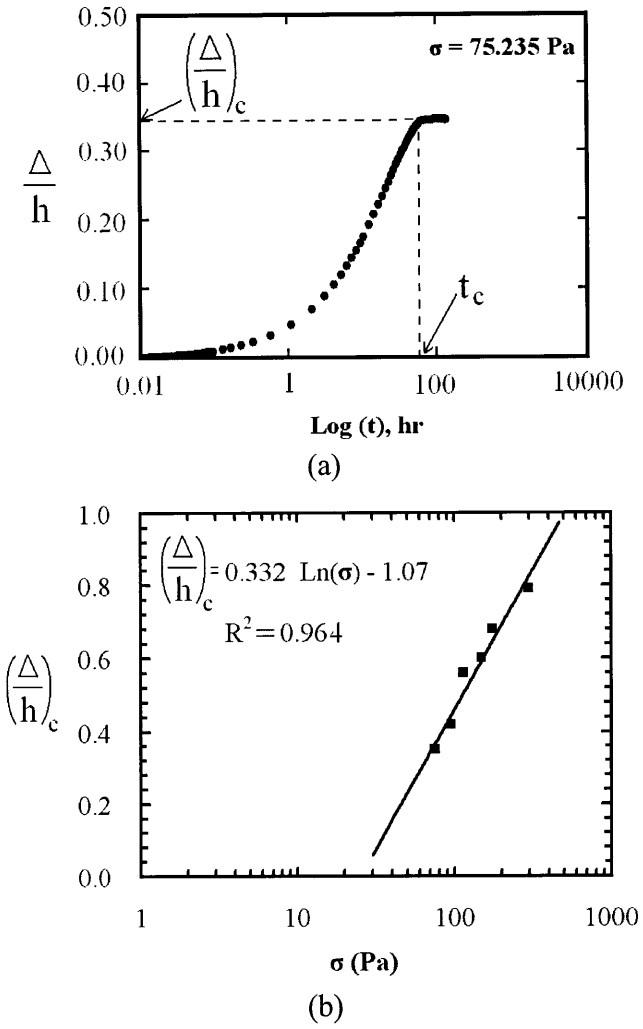

Figure 5.2. (a) A typical Δ-t plot for the CG slurry with a starting density of 0.0054 g ml^{-1} at a stress of ~75 Pa. (b) A typical $(\Delta/h)_c$-σ plot for the CG slurry. These plots are similar to the schematic plots shown in Figure 5.1b and c.

Bi-layer CG-MCG scaffolds for cartilage repair

Bi-layer osteochondral scaffolds have been developed by Lynn *et al.* for repair of articular cartilage defects [69]. Their scaffolds were made by freeze-drying a slurry consisting of two layers: MCG layer on the top (0.042 g ml^{-1}) and CG layer on the bottom (0.0054 g ml^{-1}). The slurries were kept in touch in the liquid phase for the slurries to

inter-diffuse and create a diffused boundary layer that mimics the cartilage-bone interface. However, we believe that the gradation of the diffused boundary can be improved by application of pressure through the external loads (as described above) from both the surfaces. Therefore, scaffolds with a gradual change in mineral content can be fabricated with coherent mechanical properties through the boundary.

APPENDIX A *Collagen-Based Scaffold Fabrication and Characterization Protocols*

A.1 Collagen-Glycosaminoglycan (CG) Suspension Protocol

References: [5, 66, 68, 145]

Supplies

- 3.6 gm type I microfibrillar collagen isolated from bovine ((1) Integra LifeSciences, Inc., Plainsboro, NJ, (2) Sigma-Aldrich Chemical Co, St. Louis, MO, (3) Devro Pty Ltd, Bathurst, NSW, Australia); store at 40C.
- 2991.3 ml distilled, deionized water
- 8.7 ml Glacial Acetic Acid (Mallinckrodt Chemical Co., Paris, KY)
- 0.32 gm Chondroitin 6-sulfate from shark cartilage (Cat. No. C-4384, Sigma-Aldrich Chemical Co., St. Louis, MO); store at 4°C.

Procedure

1. Turn on the cooling system (Brinkman model RC-2T) for the blender (Ultra Turrax T18 Overhead blender, IKA Works) and allow the mixing chamber to cool to 4°C (~30 minutes).

2. Prepare a 0.05 M acetic acid (HOAc) (*pH* 3.2) solution: add 8.7 ml HOAc (Glacial Acetic Acid, Mallinckrodt Chemical Co) to 2991.3 ml of distilled, deionized water in the chemical fume hood. This solution has a shelf life of approximately 1 week.

3. Blend 3.6 gm of microfibrillar bovine tendon collagen with 600 ml of 0.05 M acetic acid at 15,000 rpm (Blender Setting: 3.25) for 90 minutes at 4°C.

4. Prepare the chondroitin 6-sulfate solution: dissolve 0.32 gm chondroitin 6-sulfate (from shark cartilage: Cat. No. C-4384, Sigma-Aldrich) in 120 ml of 0.05 M acetic acid.

5. Calibrate the peristaltic pump (Manostat Cassette Pump, Cat. No. 75-500-000) to 120 ml per 1. 5 minutes.

6. Add the 120 ml chondroitin 6-sulfate solution dropwise to the blending collagen dispersion over 15 minutes using the peristaltic pump, while maintaining the blender at 15,000 rpm (Blender Setting: 3.25) and 4°C.

7. Blend the collagen-GAG suspension an additional 90 minutes at 15,000 rpm (Blender Setting: 3.25) at 4°C.

8. Degas the collagen-GAG suspension in a vacuum flask for 60+ minutes until bubbles are no longer present in the solution.

9. Store the suspension in a capped bottle at 40C; it will keep for up to four months.

10. If collagen-GAG suspension has been stored for more than one week, re-blend it for fifteen minutes at 10,000rpm (Blender Setting: 2) at 4°C and degas again.

A.2 Mineralized Collagen-Glycosaminoglycan (MCG) Suspension Protocol

References: [69, 70, 72, 74-76]

Supplies

- Type I microfibrillar bovine tendon collagen ((1) Integra LifeSciences, Inc., Plainsboro, NJ, (2) Sigma-Aldrich Chemical Co, St. Louis, MO, (3) Devro Pty Ltd, Bathurst, NSW, Australia); store at 40C.
- Distilled, deionized water
- Phosphoric acid (H_3PO_4) (EMD Chemicals Inc., Gibbstown, NJ)
- Chondroitin 6-sulfate from shark cartilage (Cat. No. C-4384, Sigma-Aldrich Chemical Co., St. Louis, MO); store at 4°C.
- calcium nitrate ($Ca(NO_3)_2.4H_2O$) and calcium hydroxide ($Ca(OH)_2$) (Sigma-Aldrich Chemical Co., St. Louis, MO).

Table A. 1 lists the amount of different supplies and the molarity of the solvent (H_3PO_4) for the 50 wt.% and 75 wt.% mineralized CG slurries.

Procedure

1. Turn on the cooling system (Brinkman model RC-2T) for the blender (Ultra Turrax T18 Overhead blender, IKA Works) and allow the mixing chamber to cool to 4°C (~30 minutes).

2. Prepare 0.138M and 0.225M phosphoric acid solutions (*pH* 1.47 and 1.35 respectively) in the chemical fume hood for the 50 wt.% and 75 wt.% MCG slurries respectively. These solutions have a shelf life of approximately 1 week.

3. Weigh out the required amount of collagen on weighing papers (don't use the plastic boats as they create too much static electricity). Add the collagen to a 250mL beaker, then add 171.4mL of the appropriate H_3PO_4 solution (Table A. 1). Before placing the collagen on to blend, weigh out the appropriate amount of chondroitin-6-sulphate into a 25mL vacuum flask, and add 14.3mL of the same phosphoric acid solution, then cover with parafilm. Be sure that the entire GAG is immersed in the solution, and that none is left dry on the walls of the flask above the liquid surface. Allow the GAG to dissolve over the 90 minutes that the collagen is blending, swishing the solution around in the flask periodically (i.e. once every 20 minutes or so).

4. Place beaker containing the collagen and acid in the cooling vessel, place the plastic lid over the top of the vessel, and then blend at 15,000rpm for 90 minutes. The stator should be cleaned with detergent, rinsed thoroughly with warm tap water, and finally rinsed with demonized water before it is placed in the solution.

5. After 90 minutes of stirring, confirm that all the chondroitin-6-sulphate has dissolved (when the solution is swished, there should be no translucent streaks), then add the GAG solution to the mixing collagen suspension using the peristaltic pump. Note that the pump should be set to reverse. The end of the hose nearest the mixing can be

secured in place using tape, to ensure that the GAG solution actually ends up in the collagen solution and not on the side of the cooling vessel. Be extremely careful that (i) the 25mL vacuum doesn't tip over (i.e. hold or secure it until all the solution goes through), (ii) that all of the solution enters the pump (tip the flask on its side and stick the tubing in the bottom corner and (iii) that all of the solution travels all the way through the tubing to and out the other end (this may require some lifting of various parts of the hose to coax the last drops through to the end). Allow the slurry to mix for 60 minutes.

6. Measure out the required quantity of calcium nitrate ($Ca(NO_3)_2.4H_2O$) on to a sheet of weighing paper; set aside. Measure out the required quantity of calcium hydroxide ($Ca(OH)_2$) onto another sheet of weighing paper. Slide the calcium nitrate onto the sheet holding the calcium hydroxide (don't try doing it the other way as calcium hydroxide is a little harder to transfer), then mix the two substances together with a spatula, until they are well dispersed.

7. After the collagen-GAG slurry has mixed for 60 minutes, remove the beaker from the cooling vessel, and place it on the bench top. Reinsert the stator and continue to blend, making sure that there is at least a portion of the suspension surface that is not covered by foam. Add the mixed calcium powders a little bit at a time; full addition of the powders should take about 15 minutes. Once a given spatula-full of powder enters the slurry and sinks to the bottom, move the beaker around so as to disperse any clumps of the powder. Make sure that all the powder from the paper and spatula gets into the slurry, that no powder is caught in the foam, and that all large clumps are broken up by moving the beaker up, down and around with your hand.

8. Add an additional 14.3mL of the same H_3PO_4 solution used to disperse the collagen and the GAG. This should be added using a pipette, and should be used to rinse any calcium powders stuck to the stator or the side of the beaker into the solution. Allow the slurry to mix for an additional 30 minutes.

9. Turn off the blender, and remove the stator. Insert a cleaned and sterilized stir bar (medium length), cover tightly with parafilm and place on a stir plate to mix for 24 hours at room temperature at setting 10 (on the blue and white plates). Be sure that the stir bar is spinning in a stable manner, and not jumping all over the beaker randomly. If the latter occurs, turn the stir plate setting to zero, and slowly increase it back to 10.

10. After 24 hours stirring, transfer both the solution and the stir bar to a labeled, cleaned and sterilized 250mL bottle and store in the fridge.

11. Before use, blend at 15,000 rpm at room temperature for 5 minutes, making sure to move the container around to break-up any clumps that have formed. The blended solution should then be allowed to stir on a stir plate for 1 hour at setting 10. Before pipetting into moulds, remove the solution from the stir plate and allow it to settle for

about 1 minute before pipetting (this will ensure that there aren't too many air bubbles in it).

Table A. 1 Concentration of reactants for a 200 ml MCG slurry.

CaP (%)	Molarity (H_3PO_4)	H_3PO_4 (ml)	dIH_2O (ml)	Collagen (gm)	GAG (gm)	$Ca(OH)_2$ (gm)	$Ca(NO_3)_2.4H_2O$ (gm)
50	0.138	3.25	347	3.86	0.336	1.81	0.780
75	0.225	5.00	360	1.93	0.168	3.03	0.966

A.3 Scaffold Fabrication: Constant Cooling Lyophilization Protocol

References: [66, 68]

Supplies
- CG/MCG slurry
- Cylindrical polysulfone mold

Equipment
- Genesis freeze dryer (VirTis)

Procedure
1. Turn on the freeze dryer (VirTis Genesis):

    - Check that the vacuum oil level is at least 2/3, the oil appears clean, and that the vacuum pump is properly vented (either outside or into a chemical fume hood)
    - Plug the condenser drain valve and close the condenser and main chamber door
    - T urn the main *Power* switch on
    - T urn the *Condenser* switch on
    - Set the *SV* gauge to 20°C and turn on the *Freeze* and *Heat* switches

You need to allow approximately 60 minutes for the freeze dryer temperature to stabilize and for the condenser to reach a cold enough temperature to continue.

2. Degas the CG suspension in a vacuum flask (Pressure: ~50 mTorr). Degas approximately twice the required volume to allow appropriate removal of all air bubbles. The length of time needed to degas the suspension varies from 30-90 min. depending on the total volume being degassed and the length of time the entire volume of suspension was degassed immediately following mixing.

3. Clean the stainless steel pan (VirTis) with ethanol and wipe the inside with Kim-Wipes to remove all dust and any remaining CG content from the previous run. When cleaning and handling the pan, do not touch the inside of the pan with your bare hands. Use gloves. Allow the pan to air dry.

4. Put enough CG/MCG suspension into the polysulfone mold such that the height of the slurry is ~ 5 mm. Remove any air bubbles introduced into the suspension during the pipetting step using a 200 µl pipette tip. Drag the bubbles to the edge of the pan, allowing them to stick to the edge. Place the pan into the freeze dryer.

5. Freeze the CG suspension using a ramping protocol to produce uniform CG scaffolds. Check the appropriate program is selected using the Wizard controller. Press the button under ***Program X (X*** = 1 - 12) (Button #1) on the digital display. Select the appropriate program number using the ***Up and Down*** keys and then press the ***Edit***

key. Check the program variables (Temperature, Time, Ramp/Hold). If the progression is incorrect, correct the values. Use the outer two buttons to scroll left or right through the program and the inner two keys to change the value of the selected criteria to match the desired program. In this thesis we have used different freezing temperature and freezing rates as described below.

- Maintain freeze dryer chamber temperature at 20°C for 5 minutes
- Ramp the chamber temperature from 20°C to the final freezing temperature (T_f = -10, -20, -30, -40°C) at a specific rate (0.9, 0.33, 0.1°C/min).
- Maintain the chamber temperature at the final freezing temperature for 12 hr to allow solidification to complete.
- After confirming the program, press the two middle keys on the Wizard together to end the editing step. Select the ***Save*** option from the menu displayed after ending the editing step. The Wizard screen should return to the original screen seen at start-up.

6. Turn off the ***Freeze*** and ***Heat*** buttons, turn the ***Auto*** button on, and press the ***Start*** key. The program should start running. Leave the program to run for the specified length of time.

7. At the end of the 12 hr annealing period, cancel the program. Press the inner two buttons on the wizard controller together, and then when prompted press the outer two keys. Turn off the ***Auto*** switch, then turn on the ***Freeze*** and ***Heat*** switches and set the ***SV*** to the appropriate freezing temperature (-10, -20, -30, or -40°C).

8. Turn on the ***Vacuum*** switch. Make sure the seal on the condenser and main chamber doors is tight and put pressure on the door to the main chamber until a vacuum pressure registers on the Wizard control screen (typically -1900 mTorr).

9. When the vacuum pressure reaches below 300 mTorr, raise the temperature in the *SV* display to 0°C. Allow the freeze dryer to run for 17 hours at 0°C and a pressure <300 mTorr.

10. After 17 hours, raise the value of the ***SV*** control to 20°C. Wait for the chamber temperature to equilibrate to 20°C (temperature displayed in the ***PV*** display). Turn off the ***Vacuum*** switch and turn on the ***Chamber Release*** switch. Wait for the pressure to equilibrate to atmospheric pressure. Remove the pan from the main chamber.

11. Turn off the freeze dryer:

- Turn off the ***Chamber Release*** switch
- Turn off the ***Freeze*** and ***Heat*** switches
- Turn off the ***Condenser*** Switch
- Turn off the ***Power*** Switch
- Open the condenser door, unplug the condenser drain line allow condense to drain

12. Remove the CG/MCG scaffold from the pan with gloved hands. Place the scaffold into an aluminum foil packet and store it in a desiccator.

13. Wash the stainless steel pan with ethanol or 0.05 M acetic acid and wipe down with kim-wipes to remove any portion of the scaffold that may have torn during removal. Return the pan to storage.

14. Make a notation on the run sheet attached to the front of the freeze dryer in order to keep track of the total number of runs between oil changes. When a row is completely checked off (8 freeze dryer runs), change the oil.

A.4 Dehydrothermal Crosslinking Protocol

References: [5, 116, 143]

Equipment

- Isotemp vacuum oven (Model 201, Fisher Scientific, Hanover Park, IL)

Procedure

1. Place the collagen-GAG scaffold into an aluminum foil packet. Leave the packet open at the top.

2. Select the appropriate processing conditions. The following processing conditions are those that are typically utilized:

   Table A. 2 Typical dehydrothermal cross-linking conditions used on CG/MCG scaffolds.

DHT identifier	Cross-linking Temperature	Cross-linking Time
DHT90/24	90°C	24 hr
DHT 105/24 (lab standard)	105°C	24 hr
DHT120/24	120°C	24 hr
DHT120/48	120°C	48 hr

   DHTI05/24 is the accepted laboratory standard crosslinking technique and is the default crosslinking applied to collagen-GAG scaffolds unless otherwise noted.

3. Place the packet into vacuum oven (Isotemp Model 201, Fisher Scientific) maintained at the desired temperature. Open the ***"Vacuum"*** knob (turn the knob counterclockwise) and close the ***"Purge"*** knob (turn the knob clockwise).

4. Turn on the vacuum pump. Wait until the vacuum has been obtained (nearly full scale on the vacuum oven dial).

5. At the end of the processing period, turn off the vacuum and vent the chamber by closing the **"Vacuum"** knob (clockwise) and opening the **"Purge"** knob (counterclockwise). Once the vacuum has completely vented, open the vacuum oven door and immediately seal the aluminum foil bag(s). The scaffold is now cross-linked and considered sterile; to maintain sterility, handle the scaffold from this point on using aseptic techniques.

6. Store the scaffold in a desiccator. Cross-linked scaffolds can remain indefinitely in a desiccator prior to use.

A.5 1-Ethyl-3-(3-Dimethylaminopropyl) Carbodiimide (EDAC) Cross-linking Protocol

References: [191-193]

Supplies

- 1-ethyl-3-(3-dimethylaminopropyl)carbodiimide (EDAC, Cat. No. E-7750, Sigma- Aldrich Chemical Co., St. Louis, MO); store in a dessicator at -20°C.
- N-hydroxysuccinimide (NHS, Cat. No. H-7377, Sigma-Aldrich); store in a dessicator at room temperature.
- Polystyrene cell culture 6-well plate (BD Falcon Multiwell Flat-Bottom Plates, Cat. No. 62406-161, VWR Scientific, Inc., Bridgeport, NJ)
- Sterile Phosphate Buffered Saline (PBS, Cat. No. 20012-043, Invitrogen, Inc., Carlsbad, CA)

Equipment

- Analytical balance (Model No. CP124S, Sartorius AG, Goettingen, Germany)
- 5, 6, or 8 mm dermal biopsy punch (Miltex, Cat. No. 52441, 52442, 52443, Moore Medical LLC, New Britain, CT)

Procedure

1. Cut the scaffold samples to be cross-linked using a 5, 6, or 8 mm dermal biopsy punch (Miltex) or using a razor blade.

2. Weigh the scaffold samples to determine the average mass of each scaffold sample to be cross-linked $(M_{scaffold})$T. o maintain the sterility of the scaffold samples to be used, weigh a series of additional samples that you can remove from the sterile environment for weighing and then discard.

3. For cross-linking scaffold disks, 1 ml of cross-linking solution volume will be required for each disk.

4. Determine the concentrations of EDAC and NHS to be used in the cross-linking solution. This protocol was designed to determine the molar ratio of EDAC:NHS:Carboxylic Acid (where the carboxylic acid groups are on the CG scaffold) based off of the mass of the scaffold samples, the assumption that the scaffolds are entirely composed of collagen, and the observed 1.2 mmol of carboxylic acid (COOH) groups per gram of collagen (Olde Damink, Dijkstra, *et al..*, 1996). Typical EDAC:NHS:COOH concentrations used to crosslink CG scaffolds are 1:1:5, 5:2:5, and 5:2:1 (primary crosslinking density). The mass of EDAC (M_{EDAC}) and NHS (M_{NHS}) required for a 5:2:1 EDAC:NHS:COOH solution are calculated here (Eq.(A1.1), Eq. (A1.2)) as an example:

$$M_{EDAC} = (\#Samples).M_{Scaffold}.\left(0.0012\frac{mol_{COOH}}{gm_{Collagen}}\right).\left(\frac{5mol_{EDAC}}{1mol_{COOH}}\right).\left(\frac{191.7gm_{EDAC}}{1mol_{EDAC}}\right) \quad \text{(A1.1)}$$

$$M_{NHS} = (\#Samples).M_{Scaffold}.\left(0.0012\frac{mol_{COOH}}{gm_{Collagen}}\right).\left(\frac{2mol_{NHS}}{1mol_{COOH}}\right).\left(\frac{116.0gm_{NHS}}{1mol_{NHS}}\right) \quad \text{(A1.2)}$$

5. Mix the EDAC and NHS in a half volume (0.5 ml/disk) of sterile PBS (Invitrogen), making a 2X EDAC/NHS solution.

6. Hydrate the scaffolds in a 6 well tissue culture plate (VWR) in the sterile tissue culture hood. Place 5 to 6 scaffold disks in each well and hydrate in a half volume (0.5 ml/disk) of sterile PBS (Invitrogen). Allow the scaffolds to become initially hydrated ('-15 minutes)

7. Pipette the half volume of the EDAC/NHS solution (the 2x EDAC/NHS solution in PBS made in step 5) into each well and mix thoroughly.

8. Allow crosslinking to take place for 30 minutes.

9. Remove the EDAC/NHS solution with a pipette and rinse twice with sterile PBS for an additional thirty minutes. Transfer the crosslinked scaffolds to a sealed, sterile container containing sterile PBS for storage.

10. Do not allow the scaffolds to dehydrate once they have been hydrated as this will lead to complete pore collapse.

A.6 CG Scaffold Glycolmethacrylate Embedding Protocol

References: [66, 68, 167]

Supplies

- Plastic embedding mold (Cat. No. 16643A, Polysciences, Inc., Warrington, PA)
- JB-4 plastic block holders (Cat. No. 15899-50, Polysciences)
- 10% Neutral buffered formalin (Cat. No. 08379-3.75, Polysciences):
  - 900 ml dH20
  - 100 ml 38% formaldehyde
  - 4 g monobasic sodium phosphate NaH_2PO4
  - 8.95 g dibasic sodium phosphate Na_2HPO4
- JB-4 A embedding solution:
  - 100 ml JB-4 A monomer solution (Cat. No. 0226A-800, Polysciences)
  - 0.9 g JB-4 A catalyst, (Benzoyl Peroxide, plasticized, Cat. No. 02618-12, Polysciences)
- JB-4 B embedding solution (Cat. No. 0226B-30, Polysciences)

Equipment

- Chemical Fume Hood

Procedure

1. Cut samples from the scaffold for analysis. For analysis of CG scaffold sheets, remove samples from five locations equidistantly spaced through the sheet; for analysis of the longitudinal plane through the scaffold cut 10 x 10 mm square sections, and for analysis of the transverse plane cut 10 x 5 mm rectangular sections.

2. Fix the samples in 10% neutral buffered formalin for 24-48 hrs at room temperature

3. Dehydrate the samples in increasing concentrations of ethanol in water as follows (5 min. in each bath): 0% (dH_2O), 50%, 70%, 80%, 95%, 95%, 100%, 100%, 100%.

4. Infiltrate the samples with catalyzed JB-4 A solution (Polysciences) at 4°C for 24 h in the chemical fume hood in a sealed vacuum flask. Replace with fresh JB-4 A and place under vacuum for several hours. Hold at 4°C for an additional 24 h in a sealed vacuum flask. If air bubbles are present, repeat vacuum treatment. All infiltration steps should be performed in the fume hood.

5. Mix 25ml of the JB-4 A solution with lml of the JB-4 B solution (Polysciences) and pipet ~4 ml into each well of the plastic embedding mold (Polysciences).

6. Place each sample into a well. The JB-4 mixture will polymerize quickly (< 25 min.) so make sure the samples are placed in the proper orientation. The mixture will become progressively browner in color as polymerization proceeds.

7. After the JB-4 mixture becomes viscous enough that the samples do not float, place one plastic stub (Sample block holder, Polysciences) onto each well and place the plastic mold tray in a refrigerator (4°C). Wait overnight for the polymerization to complete.

8. Remove the embedded samples from the mold and store at 4°C until use.

A.7 Sectioning the Embedded CG Scaffold Samples Protocol; Aniline Blue Staining Protocol

References: [66, 68]

Supplies

- Aniline Blue
  - 2.5 gm aniline blue (Cat. No. AC40118-0250, Fisher Scientific, Hanover Park, IL)
  - 2 ml glacial acetic acid (Mallinckrodt Chemical Co., Paris, KY)
  - 100 ml distilled water
  - Filter before use
- 1% Acetic Acid
  - 1 ml glacial acetic acid (Mallinckrodt Chemical Co.)
  - 99 ml distilled water
- 95%, 100% ethanol
- Cytoseal 60 (Cat. No. NC9472256, Fisher Scientific)

Equipment

- Leica RM2165 microtome (Mannheim, Germany)

Procedure

1. Serially section the embedded CG scaffold samples on a Leica RM2165 microtome
2. (Mannheim, Germany) at a 5m thickness. Mount each section on a glass microscope slide.
3. Dip the slides in the Aniline Blue solution for 2 - 4 minutes.
4. Place the slides into a 1% acetic acid solution for 1 minute.
5. Dip each slide 5-10 times in 95% alcohol until most of background staining goes away.
6. Dip each slide 5-10 times 100% alcohol to complete the rinsing process.
7. Mount each sample with 4 drops of Cytoseal 60 (Fisher Scientific) and coverslip. Try to not introduce air bubbles when placing the coverslip onto the sample.
8. Dry the coverslipped samples laying flat in a chemical fume hood for 1 hour (arbitrary time). Continue to dry the coverslipped samples while laying flat for an additional 2 days on the bench top or in the chemical fume hood.

A.8 CG Scaffold Pore Size Analysis Protocol: Image Acquisition and Linear Intercept Analysis using Scion Image Software

References: [66, 68, 103, 167]

Equipment

- Inverted optical microscope (Nikon Optiphot, Japan)
- CCD color video camera (Optronics Engineering, Inc., Goleta, GA)
- Scion Image analysis software (Scion Corporation, www.scioncorp.com, Frederick, MD)

Procedure

Image Acquisition

1. Visualize the embedded, sectioned, and stained scaffold samples using an optical microscope (Nikon Optiphot).

2. Acquire digital images from the longitudinal section and the transverse section using a CCD color video camera (Optronics Engineering).

Image Editing

1. Open Scion Image. Open each scaffold image and prepare it for pore size analysis.

2. Under the *'Options"* menu, select *"Threshold."* Change the threshold values until an optimal image of struts is visible. Clean up any remaining spots with the erase tool. The pore analysis macro will not count any artifact under 5 pixels across, so it is not necessary to remove every stray spot.

3. Under *"Process"* menu, select *"Make Binary"* under the *"Binary"* sub-menu. This will transform the thresholded image into a permanent binary image. Save the image as an edited *.TIF file.

Pore Analysis

1. Under the Special menu in Scion Image, select "*Load macros*", and open the "*pore characterization macros*" file.

2. Set the scale for the analysis using the "*Set Scale*" option in the *"Analyze"* menu. Under the "*Analyze*" menu, choose "*Options*" and select the number of significant digits to be displayed after the decimal point to be 5. The microscope scale was calibrated for the microscope-camera assembly in the Mechanical Behavior of Materials laboratory (Prof. Lorna Gibson), rm. 8-102:

Table A. 3 Calibration scales for Scion image for the camera-microscope assembly in 8-102.

Objective Magnification	Known Distance	No. of Pixels
4×	1 mm	325.43
10×	1 mm	838.31
40×	1 μm	2.5279
100×	1 μm	8.3842

3. Select an area of the image to be analyzed using the oval drawing tool. Try to get as much of the viable image enclosed within the curve.

4. Under the *"Special"* menu, run *Linear Intercept.* The distance between the pore walls along lines at various angles emanating from the center of the selected region will be calculated. Next, run the *Plot Intercepts* macro. This macro will transform the average distance between struts along each line into a best-fit ellipse and will calculate linear intercept coefficients CO, C1, and C2 for that ellipse.

5. Transfer C_0, C_1, and C_2 data to an Excel spreadsheet for each scaffold sample. Calculate the minor *(a)* and major *(b)* axes of the best-fit ellipse describing the average CG scaffold pore as well as the aspect ratio using the following equations:

$$a = \frac{1}{\sqrt{C_0 + \sqrt{C_1^2 + C_2^2}}} \tag{A1.3}$$

$$b = \sqrt{\frac{\sqrt{C_1^2 + C_2^2}}{C_0\sqrt{C_1^2 + C_2^2} + C_2^2 - C_1^2}} \tag{A1.4}$$

$$\text{AspectRatio} = \frac{a}{b} \tag{A1.5}$$

6. Calculate the mean pore diameter *(d)* from the major and minor axes of the best-fit ellipse (Eq (A1.6))**.** To account for the effects of pores that were not sectioned through their maximal cross-section but rather at an arbitrary angle, the ellipse major and minor axes were corrected by multiplying by 1.5 [95]. The mean pore size was calculated from the average radius by multiplying by a factor of 2.

$$d = 1.5 \times 2\sqrt{\frac{a^2 + b^2}{2}} \tag{A1.6}$$

Linear Intercept Macro Code:

```
macro 'Linear Draw'
{This macro is used for testing different line drawing routines
for use
with the macro 'Linear Intercept'}
var
  left,top,width,height,MinDim,nx,ny,i,j,k:integer;
ThetaStep,NSteps,PI,x1,x2,y1,y2,dy,dx:real;
  Theta,valx,valy,plength,scale,AspectRatio:real;
   IntLength,LineSum:real;
  Intercepts:integer;
   switch,indicator:boolean;
   unit:string;
begin
   GetRoi(left,top,width,height);
   if width=0 then begin
      PutMessage('Selection required.');
      exit;
   end;
   if width<height  then MinDim:=width
      else MinDim:=height;
   PI:=3.141592654;
   GetScale(scale,unit,AspectRatio);
   NSteps:=GetNumber('Enter theta steps between 0 and 90
deg.',3,0);
   ThetaStep:=PI/(2*NSteps);
   for j:=0 to 2*NSteps-1 do begin
      x1:=left;
      y1:=top;
  Theta:=j*ThetaStep;
     nx:=5*sin(Theta)*width/height;
     ny:=5*abs(cos(Theta));
     for i:=0 to nx do begin
        if Theta=0 then begin
                    x1:=left;
                    x2:=x1+width;
        end  else begin
                    x1:=left+(width*i/(nx+1))+width/(2*(nx+1));
                    x2:=x1+(height*cos(Theta)/sin(Theta));
                  end;
   y2:=top+height;
if x2>=left+width then begin
          x2:=left+width;
          y2:=y1+(x2-x1)*sin(Theta)/cos(Theta);
        end  else if x2<left then begin
                           x2:=left;
                          if Theta>PI/2 then y2:=y1+(x2-
x1)*sin(Theta)/cos(Theta);
                         end;
```

```
         {plength is the length of the line to be drawn in
pixels}
plength:=sqrt(sqr(x2-x1)+sqr((y2-y1)/AspectRatio));
        valx:=x1;
valy:=y1;
        dx:=(x2-x1)/plength;
        dy:=(y2-y1)/plength;
        switch:=true;
        if plength>=MinDim then begin
   for k:=0 to plength do
              PutPixel(x1+k*dx,y1+k*dy,255);
         end;
     end;
     for i:=1 to ny do begin
        if Theta<=PI/2 then begin
                  x1:=left;
                  x2:=left+width
          end  else begin
                  x1:=left+width;
                  x2:=left;
          end;
        y1:=top+height*i/(ny+1);
        y2:=y1+(width*sin(Theta)/abs(cos(Theta)));
if y2>top+height then begin
           y2:=top+height;
           x2:=x1+((y2-y1)*cos(Theta)/sin(Theta));
         end;
         {plength is the length of the line to be drawn in
pixels}
plength:=sqrt(sqr(x2-x1)+sqr((y2-y1)/AspectRatio));
        valx:=x1;
valy:=y1;
        dx:=(x2-x1)/plength;
        dy:=(y2-y1)/plength;
        switch:=true;
        if plength>=MinDim then begin
   for k:=0 to plength do
             PutPixel(x1+k*dx,y1+k*dy,255);
        end;  {if}
     end;{i}
   end; {j}
end;


macro 'Linear Intercept'
{This macro measures the linear intercept distance over a giver
ROI
at intervals of angle}
var
  left,top,width,height,MinDim,nx,ny,i,j,k:integer;
```

```
ThetaStep,NSteps,PI,x1,x2,y1,y2,dy,dx:real;
  Theta,valx,valy,plength,scale,AspectRatio:real;
   IntLength,LineSum,dummy:real;
  Intercepts:integer;
   switch,indicator:boolean;
   unit:string;
begin
   SetOptions('User1;User2');
   GetRoi(left,top,width,height);
   if width=0 then begin
      PutMessage('Selection required.');
      exit;
   end;
   if width<height  then MinDim:=width
      else MinDim:=height;
   PI:=3.141592654;
   GetScale(scale,unit,AspectRatio);
   NSteps:=18;{GetNumber('Enter # steps between 0 and 90
deg.',3,0);}
   ThetaStep:=PI/(2*NSteps);

{block out next line when doing cumulative measurements}

   SetCounter(2*NSteps);
   SetUser1Label('Theta(rad)');
   SetUser2Label('Lx10^3');
   for j:=0 to 2*NSteps-1 do begin
      LineSum:=0;
      Intercepts:=0;
      x1:=left;
      y1:=top;
  Theta:=j*ThetaStep;
     nx:=10*sin(Theta)*width/height;
     ny:=10*abs(cos(Theta));
      for i:=0 to nx do begin
        if Theta=0 then begin
                    x1:=left;
                    x2:=x1+width;
        end  else begin
                    x1:=left+(width*i/(nx+1))+width/(2*(nx+1));
                    x2:=x1+(height*cos(Theta)/sin(Theta));
                  end;
   y2:=top+height;
if x2>=left+width then begin
          x2:=left+width;
          y2:=y1+(x2-x1)*sin(Theta)/cos(Theta);
        end  else if x2<left then begin
                           x2:=left;
                          if Theta>PI/2 then   y2:=y1+(x2-
x1)*sin(Theta)/cos(Theta);
```

```
                              end;
         {plength is the length of the line to be drawn in
pixels}
plength:=sqrt(sqr(x2-x1)+sqr((y2-y1)/AspectRatio));
        valx:=x1;
valy:=y1;
        dx:=(x2-x1)/plength;
        dy:=(y2-y1)/plength;
        switch:=true;
        if plength>=MinDim then begin
        LineSum:=LineSum+(plength/scale);
   for k:=0 to plength do begin
               if GetPixel(x1+k*dx,y1+k*dy)>0
                    then indicator:=true
                    else indicator:=false;
               if (switch=true) and (indicator=true) then begin
                   Intercepts:=Intercepts+1;
                   switch:=false;
               end;
               if  (indicator=false) then switch:=true;
           end;
       end;
     end;
    for i:=1 to ny do begin
        if Theta<=PI/2 then begin
                   x1:=left;
                   x2:=left+width
          end  else begin
                   x1:=left+width;
                   x2:=left;
          end;
        y1:=top+height*i/(ny+1);
        y2:=y1+(width*sin(Theta)/abs(cos(Theta)));
if y2>top+height then begin
           y2:=top+height;
           x2:=x1+((y2-y1)*cos(Theta)/sin(Theta));
         end;
         {plength is the length of the line to be drawn in
pixels}
plength:=sqrt(sqr(x2-x1)+sqr((y2-y1)/AspectRatio));
        valx:=x1;
valy:=y1;
        dx:=(x2-x1)/plength;
        dy:=(y2-y1)/plength;
        switch:=true;
        if plength>=MinDim then begin
        LineSum:=LineSum+(plength/scale);
   for k:=0 to plength do begin
               if GetPixel(x1+k*dx,y1+k*dy)>0
                    then indicator:=true
```

```
                    else indicator:=false;
                if (switch=true) and (indicator=true) then begin
                    Intercepts:=Intercepts+1;
                    switch:=false;
                end;
                if  (indicator=false) then switch:=true;
            end;
        end;
      end;{i}
     IntLength:=LineSum/Intercepts;
    dummy:=rUser2[j+1];
     rUser1[j+1]:=180*Theta/PI;

{to do cumulative measurements, type in 'dummy+ before Intlength
in the next line}

     rUser2[j+1]:=IntLength*1000;
   end; {j}
   ShowResults;
end;

macro 'Linear Intercept +'
{This macro measures the linear intercept distance over a giver
ROI
at intervals of angle}
var
  left,top,width,height,MinDim,nx,ny,i,j,k:integer;
ThetaStep,NSteps,PI,x1,x2,y1,y2,dy,dx:real;
  Theta,valx,valy,plength,scale,AspectRatio:real;
   IntLength,LineSum,dummy:real;
  Intercepts:integer;
   switch,indicator:boolean;
   unit:string;
begin
   SetOptions('User1;User2');
   GetRoi(left,top,width,height);
   if width=0 then begin
      PutMessage('Selection required.');
      exit;
   end;
   if width<height  then MinDim:=width
      else MinDim:=height;
   PI:=3.141592654;
   GetScale(scale,unit,AspectRatio);
   NSteps:=18;{GetNumber('Enter # steps between 0 and 90
deg.',3,0);}
   ThetaStep:=PI/(2*NSteps);

{block out next line when doing cumulative measurements}
```

```
   {SetCounter(2*NSteps);}
   SetUser1Label('Theta(rad)');
   SetUser2Label('Lx10^3');
   for j:=0 to 2*NSteps-1 do begin
      LineSum:=0;
      Intercepts:=0;
      x1:=left;
      y1:=top;
  Theta:=j*ThetaStep;
     nx:=10*sin(Theta)*width/height;
     ny:=10*abs(cos(Theta));
      for i:=0 to nx do begin
        if Theta=0 then begin
                     x1:=left;
                     x2:=x1+width;
        end  else begin
                     x1:=left+(width*i/(nx+1))+width/(2*(nx+1));
                     x2:=x1+(height*cos(Theta)/sin(Theta));
                  end;
   y2:=top+height;
if x2>=left+width then begin
           x2:=left+width;
           y2:=y1+(x2-x1)*sin(Theta)/cos(Theta);
        end  else if x2<left then begin
                              x2:=left;
                             if Theta>PI/2 then   y2:=y1+(x2-
x1)*sin(Theta)/cos(Theta);
                           end;
         {plength is the length of the line to be drawn in
pixels}
plength:=sqrt(sqr(x2-x1)+sqr((y2-y1)/AspectRatio));
        valx:=x1;
valy:=y1;
        dx:=(x2-x1)/plength;
        dy:=(y2-y1)/plength;
        switch:=true;
        if plength>=MinDim then begin
        LineSum:=LineSum+(plength/scale);
   for k:=0 to plength do begin
               if GetPixel(x1+k*dx,y1+k*dy)>0
                    then indicator:=true
                    else indicator:=false;
               if (switch=true) and (indicator=true) then begin
                   Intercepts:=Intercepts+1;
                   switch:=false;
               end;
               if  (indicator=false) then switch:=true;
           end;
       end;
     end;
```

```
    for i:=1 to ny do begin
        if Theta<=PI/2 then begin
                  x1:=left;
                  x2:=left+width
          end  else begin
                  x1:=left+width;
                  x2:=left;
          end;
        y1:=top+height*i/(ny+1);
        y2:=y1+(width*sin(Theta)/abs(cos(Theta)));
if y2>top+height then begin
           y2:=top+height;
           x2:=x1+((y2-y1)*cos(Theta)/sin(Theta));
         end;
         {plength is the length of the line to be drawn in
pixels}
plength:=sqrt(sqr(x2-x1)+sqr((y2-y1)/AspectRatio));
        valx:=x1;
valy:=y1;
        dx:=(x2-x1)/plength;
        dy:=(y2-y1)/plength;
        switch:=true;
        if plength>=MinDim then begin
        LineSum:=LineSum+(plength/scale);
   for k:=0 to plength do begin
               if GetPixel(x1+k*dx,y1+k*dy)>0
                    then indicator:=true
                    else indicator:=false;
               if (switch=true) and (indicator=true) then begin
                   Intercepts:=Intercepts+1;
                   switch:=false;
               end;
               if  (indicator=false) then switch:=true;
           end;
       end;
     end;{i}
    IntLength:=LineSum/Intercepts;
   dummy:=rUser2[j+1];
    rUser1[j+1]:=180*Theta/PI;

{to do cumulative measurements, type in 'dummy+ before Intlength
in the next line}

    rUser2[j+1]:=dummy+IntLength*1000;
   end; {j}
   ShowResults;
end;

Macro 'Plot Intercepts'
```

```
{This macro plots the linear intercept distance as a function of
angle
in cylindrical coordinates
It then finds the best-fit ellipse to a set of linear intercept
distance vs. angle data
using multiple linear regression of the equation Y=C0+C1*X+C2*Z,
where
Y=1/L^2 ,  where L is one half  the linear intercept distance at
Theta
X=cosine(2*Theta),    Z=sine(2*Theta)
C0=(Mii+Mjj)/2 , C1=(Mii-Mjj)/2 , C2=Mij.
The objective is to solve for M11, Mjj, and Mij
The best-fit ellipse it then plotted on top of the linear
intercept measurements}

var
   left,top,width,height,X0,Y0,X1,Y1,i,n:integer;
   pscale,aspectRatio,dx1,dx2,dy1,dy2,maxdim:real;
   unit:string;
  sumX,sumY,sumZ,sumXZ,sumXY,sumYZ,sumZsqr,sumXsqr:real;
  C0,C1,C2,Mii,Mjj,Mij,Y,X,Z,PI,Theta1,Theta2,L1,L2:real;

begin
  PI:=3.141592654;
 SaveState;
  SetForegroundColor(255);
  SetBackgroundColor(0);
  width:=400;
  height:=400;
  maxdim:=0;
  for i:=1 to rCount do begin
     if rUser2[i]>maxdim then maxdim:=rUser2[i];
  end;
  pscale:=.8*(width+height)/(2*maxdim);
  SetNewSize(width,height);
  MakeNewWindow('Linear Intercepts vs. Theta');
  SetLineWidth(1);
  X0:=(width/2);
  Y0:=(height/2);
  MakeLineROI(0,Y0,width,Y0);
  Fill;
  MakeLineROI(X0,0,X0,height);
  Fill;
   for i:=1 to rCount do begin
     dx1:=pscale*0.5*rUser2[i]*cos(rUser1[i]*PI/180);
     dy1:=pscale*0.5*rUser2[i]*sin(rUser1[i]*PI/180);
     if i<rCount then begin
        dx2:=pscale*0.5*rUser2[i+1]*cos(rUser1[i+1]*PI/180);
        dy2:=pscale*0.5*rUser2[i+1]*sin(rUser1[i+1]*PI/180);
     end else begin
```

```
         dx2:=-pscale*0.5*rUser2[1]*cos(rUser1[1]*PI/180);
         dy2:=-pscale*0.5*rUser2[1]*sin(rUser1[1]*PI/180);
      end;
      MoveTo(X0+dx1,Y0+dy1);
      LineTo(X0+dx2,Y0+dy2);
      MoveTo(X0-dx1,Y0-dy1);
      LineTo(X0-dx2,Y0-dy2);
   end;
   n:=rCount;
   sumX:=0;
   sumY:=0;
   sumZ:=0;
   sumXY:=0;
   sumYZ:=0;
   sumXZ:=0;
   sumZsqr:=0;
   sumXsqr:=0;
   for i:=1 to n do begin
      Y:=1/(sqr(rUser2[i]/2));
      X:=cos(2*PI*rUser1[i]/180);
      Z:=sin(2*PI*rUser1[i]/180);
      sumX:=sumX+X;
      sumY:=sumY+Y;
      sumZ:=sumZ+Z;
      sumXY:=sumXY+(X*Y);
      sumYZ:=sumYZ+(Y*Z);
      sumXZ:=sumXZ+(X*Z);
      sumZsqr:=sumZsqr+sqr(Z);
      sumXsqr:=sumXsqr+sqr(X);
   end;
   C1:=((sumXY*sumZsqr)-(sumXZ*sumYZ))/((sumXsqr*sumZsqr)-
sqr(sumXZ));
   C2:=((sumYZ*sumXsqr)-(sumXY*sumXZ))/((sumXsqr*sumZsqr)-
sqr(sumXZ));
   C0:=(sumY/n)-C1*(sumX/n)-C2*(sumZ/n);
   for i:=1 to rCount do begin
      Theta1:=rUser1[i]*PI/180;
      if i<rCount then Theta2:=rUser1[i+1]*PI/180
       else Theta2:=rUser1[1]*PI/180;
      L1:=1/sqrt(C0+C1*cos(2*Theta1)+C2*sin(2*Theta1));
      L2:=1/sqrt(C0+C1*cos(2*Theta2)+C2*sin(2*Theta2));
      dx1:=pscale*L1*cos(Theta1);
      dy1:=pscale*L1*sin(Theta1);
      if i<rCount then begin
         dx2:=pscale*L2*cos(Theta2);
         dy2:=pscale*L2*sin(Theta2);
       end else begin
         dx2:=-pscale*L2*cos(Theta2);
         dy2:=-pscale*L2*sin(Theta2);
      end;
```

```
      MoveTo(X0+dx1,Y0+dy1);
      LineTo(X0+dx2,Y0+dy2);
      MoveTo(X0-dx1,Y0-dy1);
      LineTo(X0-dx2,Y0-dy2);
    end;
NewTextWindow('Results');
write('C0 = ',C0:8:8);
write('C1 = ',C1:8:8);
write('C2 = ',C2:8:8);
end;


macro 'Count Black and White Pixels [B]';
{Counts the number of black and white pixels in the current
selection and stores the counts in the User1 and User2 columns.}
begin
  RequiresVersion(1.44);
  SetUser1Label('Black');
  SetUser2Label('White');
  Measure;
  rUser1[rCount]:=histogram[255];
  rUser2[rCount]:=histogram[0];
  UpdateResults;
end;


macro 'Compute Percent Black and White';
{Computes the percentage of back and white pixels in the
current selection. This macro only works with binary images.}
var
  nPixels,mean,mode,min,max:real;
begin
  RequiresVersion(1.44);
  SetUser1Label('Black');
  SetUser2Label('White');
  Measure;
  GetResults(nPixels,mean,mode,min,max);
  rUser1[rCount]:=histogram[255]/nPixels;
  rUser2[rCount]:=histogram[0]/nPixels;
  UpdateResults;
  if (histogram[0]+histogram[255])<>nPixels
    then PutMessage('This macro requires a binary image.');
end;


macro 'Compute Area Percentage [P]';
{Computes the percentage of foreground
pixels in the current selection.}
var
  mean,mode,min,max:real;
```

```
  i,lower,upper,fPixels,nPixels,count:integer;
begin
  RequiresVersion(1.50);
  SetUser1Label('%');
  Measure;
  GetResults(nPixels,mean,mode,min,max);
  GetThresholds(lower,upper);
  if (lower=0) and (upper=0) and
     ((histogram[0]+histogram[255])<>nPixels)
     then begin
       PutMessage('This macro requires a binary or thresholded
image.');
       exit;
     end;
  if nPixels=0 then begin
  end;
  if (lower=0) and (upper=0) then begin
    if nPixels=0
      then rUser1[rCount]:=0
      else rUser1[rCount]:=(histogram[255]/nPixels)*100;
    UpdateResults;
    exit;
  end;
  fPixels:=0;
  nPixels:=0;
  for i:=0 to 255 do begin
    count:=histogram[i];
    nPixels:=nPixels+count;
    if (i>=lower) and (i<=upper)
      then fPixels:=fPixels+count;
  end;
  rUser1[rCount]:=(fPixels/nPixels)*100;
  UpdateResults;
end;
```

A.9 CG Scaffold Pore Size and pore wall thickness Analysis Protocol: Image Acquisition and Analysis using Matlab Software

References: [104, 152]

Equipment

- Inverted optical microscope (Nikon Optiphot, Japan)
- CCD color video camera (Optronics Engineering, Inc., Goleta, GA)
- Matlab software (https://nic-too.mit.edu/cgi-bin/matlab)

Procedure

Image Acquisition

1. Visualize the embedded, sectioned, and stained scaffold samples using an optical microscope (Nikon Optiphot).

2. Acquire digital images from the longitudinal section and the transverse section using a CCD color video camera (Optronics Engineering). Save the images in the BMP format with two digit numbers, such as *01.BMP*, *02.BMP*, etc. Also acquire a background image of the "glass slide + glycomethacrylate" (without any scaffold cross-section) with the same microscope set up (magnification and brightness) and name it as *bkg.BMP*.

3. For each of the planes: *xy*, *yz*, and *xz* (in case of the rectangular scaffolds) and $r\theta$, and θz (in case of the circular scaffolds), put all the images of that plane and the background image (bkg.BMP) in a specific folder.

Pore Diameter and Thickness Analysis

1. Seven different programs are written in Matlab to do the pore microstructure calculations. The programs are:

    - eliminateComponents.m
    - ellipsefit.m
    - getThickness.m
    - main1.m
    - main2.m
    - poreDia.m
    - poreThickness.m

The files are written out below. Put all these files in one folder and name it as "*code*". Open matlab and direct the "*current directory*" (in the top of the window) to the folder "*code*".

2. In the command window type "*edit main1*", adjust the "*thresh*" value to the desired threshold value to get the optimum black and white image from the actual images.

Also adjust the "*threshSize*" to the optimum value so that you do not include stray spots. Under "*Directories*", for "*codepath*" write the path to the folder "*code*", and for "*Path to the images*", write the path name to the specific image folder you want to run the analysis on.

3. Run the file "*main1*". It creates a folder called "*thresh#*" (# is the threshold value you put in the *main1* program in the previous step). Look at the thresholded images in this folder and see if the images are thresholded well enough to calculate the pore diameter and thickness. Otherwise delete the folder and go back to previous step and put a different "*thresh*" value and "*threshSize*". Keep trying step 2 and 3 until you have a set of images that is good enough to run the analysis.

4. In the command window type "*edit main2*", adjust the "*scale*" to the scale of the image in "*μm/pixel*". It can be calculated from Table A1.3. Adjust "*minSize*" and "*maxSize*" to the minimum and maximum possible pore wall thickness in *μm*. Under "*Directories*", for "*codepath*" write the path to the folder "*code*", and for "*threshpath*", write the path name to the folder "*thresh#*" (from step 3).

5. Run the file "*main2*". It creates a text file called "*output.txt*" within the folder "*thresh#*" (from step 3). The folder "*output.txt*" has the outputs in the order of: a, b, R, d, and t_{2D} (*a*: major axis, *b*: minor axis, *R*: anisotropic ratio, *d*: pore diameter, and t_{2D}: pore thickness measured in 2D). The pore wall thickness in 3D can be calculated from t_{2D} by Eq (3.5).

MatLab Codes

eliminateComponents

```
function L = eliminateComponents(Im,sc)[L,num] = bwlabel(Im);

      for i = 1:num
          s = sum(sum(L==i));
          if s<sc
              L = L.*(L~=i);
          end
      end
      L=L>0;
```

ellipsefit

```
function [varargout]=ellipsefit(x,y)
%ELLIPSEFIT Stable Direct Least Squares Ellipse Fit to Data.
% [Xc,Yc,A,B,Phi,P]=ELLIPSEFIT(X,Y) finds the least squares
ellipse that
% best fits the data in X and Y. X and Y must have at least 5
data points.
```

```
% Xc and Yc are the x- and y-axis center of the ellipse
respectively.
% A and B are the major and minor axis of the ellipse
respectively.
% Phi is the radian angle of the major axis with respect to the
x-axis.
% P is a vector containing the general conic parameters of the
ellipse.
% The conic representation of the ellipse is given by:
%
% P(1)*x^2 + P(2)*x*y + P(3)*y^2 + P(4)*x + P(5)*y + P(6) = 0
%
% S=ELLIPSEFIT(X,Y) returns the output data in a structure with
field names
% equal to the variable names given above, e.g., S.Xc, S.Yc, S.A,
S.B,
% S.Phi and S.P
%
% Reference: R. Halif and J. Flusser, "Numerically Stable Direct
Least
% Squares FItting of Ellipses," Department of Software
Engineering, Charles
% University, Czech Republic, 2000.

% Conversion from conic to conventional ellipse equation inspired
by
% fit_ellipse.m on MATLAB Central

% D.C. Hanselman, University of Maine, Orono, ME 04469
% Mastering MATLAB 7
% 2005-02-28
% Rotation angle fixed 2005-08-09

%------------------------------------------------------------------
x=x(:); % convert data to column vectors
y=y(:);
if numel(x)~=numel(y) || numel(x)<5
   error('X and Y Must be the Same Length and Contain at Least 5
Values.')
end

D1=[x.*x x.*y y.*y]; % quadratic terms
D2=[x y ones(size(x))]; % linear terms
S1=D1'*D1;
S2=D1'*D2;

[Q2,R2]=qr(D2,0);
if condest(R2)>1.0e10
   warning('ellipsefit',...
```

```
      'Data is Poorly Conditioned and May Not Represent an
Ellipse.')
end
T=-R2\(R2'\S2'); % -inv(S3) * S2'

M=S1+S2*T;
CinvM=[M(3,:)/2; -M(2,:); M(1,:)/2];
[V,na]=eig(CinvM);
c=4*V(1,:).*V(3,:) - V(2,:).^2;
A1=V(:,c>0);
P=[A1; T*A1];

% correct signs if needed
P=sign(P(1))*P;

Phi=atan(P(2)/(P(3)-P(1)))/2;
c=cos(Phi);
s=sin(Phi);

% rotate the ellipse parallel to x-axis
Pr=zeros(6,1);
Pr(1)=P(1)*c*c - P(2)*c*s + P(3)*s*s;
Pr(2)=2*(P(1)-P(3))*c*s + (c^2-s^2)*P(2);
Pr(3)=P(1)*s*s + P(2)*s*c + P(3)*c*c;
Pr(4)=P(4)*c - P(5)*s;
Pr(5)=P(4)*s + P(5)*c;
Pr(6)=P(6);

% extract other data
XcYc=[c s;-s c]*[-Pr(4)/(2*Pr(1));-Pr(5)/(2*Pr(3))];
Xc=XcYc(1);
Yc=XcYc(2);
F=-Pr(6) + Pr(4)^2/(4*Pr(1)) + Pr(5)^2/(4*Pr(3));
AB=sqrt(F./Pr(1:2:3));
A=AB(1);
B=AB(2);
Phi=-Phi;
if A<B % x-axis not major axis, so rotate it pi/2
   Phi=Phi-sign(Phi)*pi/2;
   A=AB(2);
   B=AB(1);
end
S.Xc=Xc;
S.Yc=Yc;
S.A=A;
S.B=B;
S.Phi=Phi;
S.P=P;
if nargout==1
   varargout{1}=S;
```

```
else
   outcell=struct2cell(S);
   varargout=outcell(1:nargout);
end
```

getThickness

```
function avg = getThickness(line)
len = length(line);
grad = line(2:len) - line(1:len-1);
n = sum(line(1:len));
t = sum(grad>0);
if (n==len)
    avg = n;
    return;
end
if (t~=0)
    avg = (n/t);
else
    avg = 0;
end
```

main1

```
clear all;clc;close all

% Parameters for calculation of pore diameter
thresh = 25; % intensity for cleaning images
threshSize = 30; % maximum component size that gets deleted

% Directories
codepath = 'C:\Documents and Settings\Biraja
Kanungo\Desktop\code';
path(path,'C:\Documents and Settings\Biraja
Kanungo\Desktop\Code'); % Path to code

% Path to images
pathname = 'C:\Documents and Settings\Biraja Kanungo\Desktop\PORE
ANALYSIS\1X';
% Cleaned images are written here
threshpath = ['C:\Documents and Settings\Biraja
Kanungo\Desktop\PORE ANALYSIS\1X\thresh' num2str(thresh)];

%%%%%%%%%%%%%%%%%%%%%%%%%%%%%%%%%%%%%%%%%%%%%%%%%%%%%%%%%%%%%%%%%%%%%%%%
mkdir(threshpath);
cd(pathname)
files = dir;
for ind = 1:length(files)
    name = files(ind).name
    if ( (upper(name(end)) == 'P') && (upper(name(end-4))~='G') )
        % Note the file extension of the background
```

```
        bgname = ['bkg.BMP'];

        cd (pathname)
        If = imread(name);
        Ib = imread(bgname);

        if size(If,3)>1
            If = rgb2gray(If);
        end
        if size(Ib,3)>1
            Ib = rgb2gray(Ib);
        end
        If = double(If);
        Ib = double(Ib);
        Im = Ib - If < thresh;
        Im = eliminateComponents(Im, threshSize);
        Im = ~eliminateComponents(~Im, threshSize);

        cd(threshpath)
        imwrite(uint8(255*(Im)),[name(1:end-4) '.bmp'])
    end
end
cd(codepath);
```

main2

```
clear all;clc;close all

stepSize = 5; % angle discretization in [0, 180]
lineSpacing  = 10; %

scale = 1000/746; % Scaling
minSize = 5; % Minimum wall thickness possible
maxSize = 120; % Maximum wall thickness possible

% Directories
codepath = 'C:\Documents and Settings\Biraja
Kanungo\Desktop\Code';
path(path,'C:\Documents and Settings\Biraja
Kanungo\Desktop\Code'); % Path to code

% Cleaned images are written here
threshpath = 'C:\Documents and Settings\Biraja
Kanungo\Desktop\PORE ANALYSIS\1X\thresh25';

%%%%%%%%%%%%%%%%%%%%%%%%%%%%%%%%%%%%%%%%%%%%%%%%%%%%%%%%%%%%%%%%%%%%%%%%%%%%
cd(threshpath)
files = dir;
fid = fopen('output.txt', 'w');
for ind = 1:length(files)
```

```
    name = files(ind).name
    if ( (upper(name(end)) == 'P') )
        Im = imread(name);

        [X Y b a phi aspect_ratio D Dscale] = ...
           poreDia(Im,stepSize,lineSpacing,scale);

        thickness = poreThickness(Im,scale,minSize,maxSize);

        %Dscale and thickness in microns
        out = [b a aspect_ratio Dscale thickness];
        fprintf(fid,'%s %6.2f %6.3f %6.2f %6.2f
%6.2f\n',name,out);

%         % Graphical plotting of results
%         figure,
%         subplot(2,2,1),imagesc(If),colormap gray,axis
equal,axis tight
%         title('Original Image')
%         subplot(2,2,2),imagesc(Im),colormap gray,axis
equal,axis tight
%         title('Thresholded Image')
%         subplot(2,2,3),plotellipse(gca,[Xc Yc],a,b,phi,'k-
'),hold;
%         subplot(2,2,3),plot([X X(1)],[Y Y(1)],'rx-'), axis
equal,axis tight
%         title('Least square ellipse fit in polar coordinates');
%         xlabel('X\rightarrow'); ylabel('Y\rightarrow');

    end
end
fclose(fid);  %Closes the file opened for writing results
cd(codepath);
```

poreDia

```
function [X Y b a phi aspect_ratio D Dscale] = ...
    poreDia(Im, step_size,line_spacing,scale)
[row,col] = size(Im);
angles = [0:step_size:180-step_size];
N = length(angles);
for i = 1:N
    Jr = (imrotate(Im,angles(i),'crop')>0.5);
    n=0;s=0;
    for j = 1:line_spacing:row
        t = getThickness(Jr(j,:));
        s = s + t;
        n = n + (t~=0);
    end
    if (n == 0)
```

```
        intercepts(i) = 0;
    else
        intercepts(i) = s/n;
    end
end
% Figure quantities
X = cos(pi*angles/180).*intercepts/2;
Y = sin(pi*angles/180).*intercepts/2;
X = [X -X]; Y = [Y -Y];
% Final parameters
[Xc,Yc,a,b,phi,p] = ellipsefit(X,Y);
aspect_ratio = b/a;
D = 2 * sqrt( (a^2 + b^2)/2 );
Dscale = 1.5*D*scale;
% [b a phi aspect_ratio D Dscale]
```

poreThickness

```
function dia = poreThickness(Im,scale, minSize, maxSize)
If = ~Im;
Ib = Im;
L = bwdist(Ib);
T = imdilate(L,ones(5,5));
S = (T==L).*(If).*(L>minSize).*(L<maxSize);
% Diameter
D = (L.*S);
radius = sum(sum(D))/sum(sum(S));
dia = 2*radius*scale;
```

A.10 CG Scaffold Mechanical Characterization Protocol using Zwick Mechanical Tester: Compression

References: [17, 103, 104, 152]

Supplies

- 5 mm dermal biopsy punch (Miltex, Cat. No. 52442 or 52443, Moore Medical LLC, New Britain, CT)
- Phosphate Buffered Saline (PBS, Cat. No. 20012-043, Invitrogen, Inc., Carlsbad, CA)

Equipment

- Zwick/Roell Mechanical Tester (Model No. Z2.5/TN1S, Zwick GmbH & Co., Ulm, Germany)
- 20 N load cell (Part No. BTC-LC0020N.P01, Zwick)
- Video Extensometer software (Correlated Solutions, Inc., West Columbia, SC)
- High-speed, digital CCD Camera (Retiga 1300, QImaging Corp., Canada)
- 200 mm lens (Nikon, Japan)

Procedure

1. Attach the 20 N load cell (Zwick Part No. BTC-LC0020N.P01) to the mechanical tester (Zwick Model No. Z2.5/TN1S). Confirm the connection between the load cell and the testXpert (Zwick) test environment and data acquisition software package.

2. Using the integrated testXpert software package, define the mechanical characterization environment. Save the test environment as a *.ZPV file.

    - Test type: *Unconfined compression*
    - Sample geometry: *Cylindrical disk, 5 mm diameter*
    - Strain range: *0 - 95% strain*
    - Loading rate: *0. 1-2% strain/sec, strain controlled*
    - Sampling frequency: *2 Hz*
    - Hold time at max strain: *30 seconds*

3. For mechanical characterization of dry or hydrated CG scaffolds, cut cylindrical disks from the scaffold sheet using a 6 or 8 mm diameter dermal biopsy punch (Miltex). Hydrate the scaffold samples, if necessary, for 12 hours in Phosphate Buffered Saline (PBS, Invitrogen).

4. Measure the dimensions of each scaffold sample being tested in order to calculate stress and strain from the load-displacement data.

5. In order to measure the lateral strains of the scaffold sample under unconfined compression and calculate the Poisson's ratio of the scaffold, set up the high-speed, digital CCD Camera (Retiga 1300, QImaging Corp.) with a 200 mm lens (Nikon) linked to a laptop running the video extensometer software (Correlated Solutions);

link the data acquisition laptop to the Zwick mechanical tester so that a lateral strain data point is acquired every time an unconfined compression data point is taken.

6. Using the testXpert control software, perform sequential mechanical tests on a series of CG scaffold samples. Save the data file for each series of tested scaffolds as a *.ZSE file.

7. Export the acquired *Standard Force (N), Standard Strain* (%), and *Test Time (s)* data from the testXpert software package to an Excel spreadsheet. Export the lateral strain data from the video extensometer package to the same spreadsheet.

8. Calculate stress from the acquired force data and the measured scaffold dimensions.

9. Determine E^* and $\Delta\sigma/\Delta\varepsilon$ from the linear regions of the linear elastic and collapse plateau regimes. Calculate σ^* and ε^* from the intersection of the linear regressions of E^* and $\Delta\sigma/\Delta\varepsilon$.

10. Determine the Poisson's ratio, υ, from the measured vertical and lateral strains in the linear elastic and collapse plateau regimes.

A.11 CG Scaffold Mechanical Characterization Protocol using Zwick Mechanical Tester: Tension

References: [17, 103, 104, 152]

Supplies

- Rectangular specimen cut on the plane of the scaffold sheet (length: ~ 15 mm, width: ~ 10 mm, and thickness: ~ 5 mm). After clamping the specimen on the top and bottom, the effective length of the sample becomes ~ 5 mm.
- Phosphate Buffered Saline (PBS, Cat. No. 20012-043, Invitrogen, Inc., Carlsbad, CA)
- Special fixtures to hold the samples under tensile loading

Equipment

- Zwick/Roell Mechanical Tester (Model No. Z2.5/TN1S, Zwick GmbH & Co., Ulm, Germany)
- 20 N load cell (Part No. BTC-LC0020N.P01, Zwick)
- Video Extensometer software (Correlated Solutions, Inc., West Columbia, SC)
- High-speed, digital CCD Camera (Retiga 1300, QImaging Corp., Canada)
- 200 mm lens (Nikon, Japan)

Procedure

1. Attach the 20 N load cell (Zwick Part No. BTC-LC0020N.P01) to the mechanical tester (Zwick Model No. Z2.5/TN1S). Confirm the connection between the load cell and the testXpert (Zwick) test environment and data acquisition software package.

2. Clamp the samples at the top and bottom by the special fixtures for tension tests. After clamping ~ 5mm of the scaffold specimen on both ends, the effective testing length becomes ~ 5mm.

3. Using the integrated testXpert software package, define the mechanical characterization environment. Save the test environment as a *.ZPV file.

    - Test type: *Uniaxial Tension*
    - Sample geometry: *Rectangular, 5×10× 5 mm^3*
    - Strain range: *0 - 95% strain*
    - Loading rate: *0.1-2% strain/sec, strain controlled*
    - Sampling frequency: *2 Hz*
    - Hold time at max strain: *30 seconds*

4. For mechanical characterization of dry or hydrated CG scaffolds, cut rectangular samples from the scaffold sheet Hydrate the scaffold samples, if necessary, for 12 hours in Phosphate Buffered Saline (PBS, Invitrogen).

5. Measure the dimensions of each scaffold sample being tested in order to calculate stress and strain from the load-displacement data.

6. In order to measure the lateral strains of the scaffold sample under uniaxial tension and calculate the Poisson's ratio of the scaffold, set up the high-speed, digital CCD Camera (Retiga 1300, QImaging Corp.) with a 200 mm lens (Nikon) linked to a laptop running the video extensometer software (Correlated Solutions); link the data acquisition laptop to the Zwick mechanical tester so that a lateral strain data point is acquired every time an unconfined compression data point is taken.

7. Using the testXpert control software, perform sequential mechanical tests on a series of CG scaffold samples. Save the data file for each series of tested scaffolds as a *.ZSE file.

8. Export the acquired *Standard Force (N), Standard Strain* (%), and *Test Time (s)* data from the testXpert software package to an Excel spreadsheet. Export the lateral strain data from the video extensometer package to the same spreadsheet.

9. Calculate stress from the acquired force data and the measured scaffold dimensions.

10. Determine E^* from the initial linear region of the stress-strain plot (at ~ 0% strain).

11. Determine the Poisson's ratio, υ, from the measured vertical and lateral strains in the linear elastic and collapse plateau regimes.

A.12 MC3T3-E1 mouse clonal osteogenic cell passaging

Supplies

- MC3T3-E1 mouse clonal osteogenic cells (ATCC, Manassas, VA)
- Pre-warmed complete MEM-α media supplemented with 10% FBS (Invitrogen, Chicago, IL)
- Pre-warmed Dulbecco's Phosphate Buffered Saline Solution (PBS, Invitrogen)
- Pre-warmed trypsin-EDTA (Catlog# 25300062, Invitrogen)
- Trypan blue (15250-01, Gibco, Grand Island, NY)

Equipment

- Hemacytometer, cleaned and washed (Bright-Line, Hausser Scientific, Horsham, PA)
- Inverted microscope
- 10, 25, and 50 ml Pipettes
- 10, 25, and 50 ml pipette tips
- 10, 200, 1000 FL pipettes and pipette tips
- 75 cm^2 tissue culture flasks (BD Falcon T-75, 353136)
- Centrifuge (Labofuge 400, Heraeus)
- 50 ml Falcon tubes
- 1 ml Eppendorf tubes or PCR tubes

Procedure

1. Turn on the water bath.

2. Prepare the hemocytometer.

    - Clean the hemocytometer and cover slip with water and ethanol (EtOH).
    - Check under the microscope for debris that can be mistaken for cells. If debris is present, clean the hemocytometer again. Otherwise position the cover slip.

3. Thaw and/or warm up media, PBS, and trypsin-EDTA in the 37 C water bath (about 30 min before passaging).

4. Remove the cells from the incubator and place them in the hood.

5. Remove the media from each culture flask.

6. Wash the cells in each flask with 5 ml PBS.

    - Add the PBS to the cells.
    - Gently rock the flask back and forth to spread the PBS over the entire surface area.
    - Leave the PBS on the cells for about 20 seconds; then pipette it out of the flasks.

7. Pipette 4 ml trypsin in each flask and put cells in incubator 8 min. Make sure that the trypsin solution covers the cells.

8. After 8 min, take the cells out of the incubator. Shake the flasks gently and check for cells floating in the trypsin (visible without microscope). Double check for

9. non-adherent cells under the microscope. If the cells are still adherent, incubate them in trypsin a little longer. Otherwise put cells in hood and continue.

10. Deactivate the trypsin by adding 6 ml of media to each flask.

11. Put the cells+media+trypsin in a 50 ml falcon tube.

12. Remove 100 uL of cells and transfer them to an eppendorf tube. Centrifuge the remainder of the cells at 2700 rpm for 5 min to pellet the cells.

13. While the cells are centrifuging, determine the cell the total cell number.

    - Add 100 uL trypan blue to the 100 uL of cells in the eppendorf tube; i.e., *dilution factor* of 2.
    - Mix well.
    - Remove 10 uL and pipette it onto the hemocytometer.
    - Count the number of cells, N, in a given number of squares, n (at least 5) using the counter.
    - Calculate the total cell number, TN, from the following formula:

$$TN = \frac{N \times dilution\ factor \times 10000 \times (\#ml\ the\ 100\ \mu l\ of\ cells\ were\ taken\ from)}{n} \quad \text{(A1.7)}$$

    - Dispose of the trypan blue cells in a special waste container.
    - Wash off hemocytometer with water and ethanol.

14. After centrifuging, decant the media, being careful not to disturb the cell pellet.

15. Resuspend the cells in fresh media to the desired concentration.

16. Pipette the desired number of cells into culture flasks, and add media so that the final volume concentration is about 17 ml.

17. Put cells in incubator, changing media every 3-4 days if cells are not passaged. Passage the cells again when they subconfluent.

18. Clean everything, making sure to bleach any items that came in contact with cells.

Note: When using flasks that don't have vented caps, be sure that the cap is untwisted about a quarter or half turn while the cells are in the incubator.

A.13 MC3T3-E1 mouse clonal osteogenic cell seeding onto the scaffolds and counting the cells after 24 hour.

Supplies

- MC3T3-E1 mouse clonal osteogenic cells (ATCC, Manassas, VA)
- Pre-warmed complete MEM-α media supplemented with 10% FBS (Invitrogen, Chicago, IL)
- Pre-warmed Dulbecco's Phosphate Buffered Saline Solution (PBS, Invitrogen)
- Pre-warmed trypsin-EDTA (Catlog# 25300062, Invitrogen)
- 6 mm diameter and 5 mm thick CG scaffolds
- 6-well tissue culture ultra low attachment agarose coated plate (Corning Inc., Corning, NY).
- Dispase (Invitrogen, Chicago, IL)

Procedure

1. Place the CG scaffold samples into wells of a 6-well tissue culture ultra low attachment agarose coated plate (Corning Inc., Corning, NY). Hydrate the CG scaffolds with 10% PBS for 12 hr under vacuum followed by hydrating with the MEM-α medium supplemented with 10% FBS for another 12 hr under vacuum.

2. Remove the CG scaffolds from the medium and partially dry using a filter paper.

3. Pipette 10 μl of the MC3T3-E1 cell suspension (1.25×10^4 cells/μl) onto one surface of the partially dry scaffold.

4. Place the scaffolds inside an incubator for 30 min to allow for initial cell attachment through that surface.

5. Turn over the seeded scaffolds and pipette an additional 10 μl of the cell suspension onto the reverse surface of the scaffold.

6. Place the scaffolds in the incubator for additional 30 min to allow for initial cell attachment through the reverse surface.

7. Fill the with 3ml of the MEM-α medium (supplemented with 10% FBS) and place into a cell culture incubator and maintained at 37°C with 5% CO_2 for 24 hr.

8. Remove the seeded scaffold samples from the tissue culture plate. Rinse each sample with 10% PBS at 37°C to remove unattached cells and place it in a 2.0 U/ml solution of dispase for 15 min to digest the scaffolds.

9. Count the number of viable cells attached using a hemocytometer as mentioned in previous protocol (Eq (A1.7)).

Bibliography

1. Langer R,Vacanti JP. Tissue Engineering. Science 1993;260 (5110): p 920-926.
2. Lee KY,Mooney DJ. Hydrogels for tissue engineering. Chemical Reviews 2001;101 (7): p 1869-1879.
3. Mason C,Dunnill P. The strong financial case for regenerative medicine and the regen industry. Regenerative Medicine 2008;3 (3): p 351-363.
4. Harley BA. Cell-matrix interactions : collagen-GAG scaffold fabrication, characterization, and measurement of cell migratory and contractile behavior via confocal microscopy. Sc. D Thesis; Mechanical Engineering; Massachusetts Institute of Technology 2006: p. 393.
5. Yannas IV, Lee E, Orgill DP, Skrabut EM,Murphy GF. Synthesis and Characterization of a Model Extracellular-Matrix That Induces Partial Regeneration of Adult Mammalian Skin. Proceedings of the National Academy of Sciences of the United States of America 1989;86 (3): p 933-937.
6. Yang J, Yamato M, Kohno C, Nishimoto A, Sekine H, Fukai F,Okano T. Cell sheet engineering: Recreating tissues without biodegradable scaffolds. Biomaterials 2005;26 (33): p 6415-6422.
7. Victor J, Bellemans J, Witvrouw E, Govaers K,Fabry G. Graft selection in anterior cruciate ligament reconstruction - Prospective analysis of patellar tendon autografts compared with allografts. International Orthopaedics 1997;21 (2): p 93-97.
8. Horas U, Pelinkovic D, Herr G, Aigner T,Schnettler R. Autologous chondrocyte implantation and osteochondral cylinder transplantation in cartilage repair of the knee joint - A prospective, comparative trial. Journal of Bone and Joint Surgery-American Volume 2003;85A (2): p 185-192.
9. Cole DW, Ginn TA, Chen GJ, Smith BP, Curl WW, Martin DF,Poehling GG. Cost comparison of anterior cruciate ligament reconstruction: Autograft versus allograft. Arthroscopy-the Journal of Arthroscopic and Related Surgery 2005;21 (7): p 786-790.
10. Noyes FR,BarberWestin SD. Reconstruction of the anterior cruciate ligament with human allograft - Comparison of early and later results. Journal of Bone and Joint Surgery-American Volume 1996;78A (4): p 524-537.
11. Starzl TE,Warty VS. Baboon-to-Human Liver-Transplantation - Reply. Lancet 1993;341 (8853): p 1158-1158.

12. Mueller YM, Davenport C,Ildstad ST. Xenotransplantation: Application of disease resistance. Clinical and Experimental Pharmacology and Physiology 1999;26 (12): p 1009-1012.
13. Cascalho M,Platt JL. Xenotransplantation and other means of organ replacement. Nature Reviews Immunology 2001;1 (2): p 154-160.
14. Cascalho M,Platt JL. New technologies for organ replacement and augmentation. Mayo Clinic Proceedings 2005;80 (3): p 370-378.
15. Copeland JG, *et al.* Cardiac replacement with a total artificial heart as a bridge to transplantation. New England Journal of Medicine 2004;351 (9): p 859-867.
16. Rideout WM, Eggan K,Jaenisch R. Nuclear cloning and epigenetic reprogramming of the genome. Science 2001;293 (5532): p 1093-1098.
17. Harley BA, Leung JH, Silva ECCM,Gibson LJ. Mechanical characterization of collagen-glycosaminoglycan scaffolds. Acta Biomaterialia 2007;3 (4): p 463-474.
18. Freyman TM, Yannas IV,Gibson LJ. Cellular materials as porous scaffolds for tissue engineering. Progress in Materials Science 2001;46 (3-4): p 273-282.
19. Vickers SM. Cell-seeded type II collagen scaffolds for articular cartilage tissue engineering. PhD Thesis; Mechanical Engineering; Massachusetts Institute of Technology 2007: p. 241.
20. Hollinger JO, Einhorn TA, Doll BA,Sfeir C. Bone Tissue Engineering 2005; CRC press, p. 336.
21. Lee KY. Design parameters of polymers for tissue engineering applications. Macromolecular Research 2005;13 (4): p 277-284.
22. Yannas IV, Burke JF, Gordon PL, Huang C,Rubenstein RH. Design of an Artificial Skin .2. Control of Chemical-Composition. Journal of Biomedical Materials Research 1980;14 (2): p 107-132.
23. Yannas IV,Spector M. Design of Medical Devices and Implants. *MIT course No: 3.961* 2006; Cambridge.
24. Yannas IV. Tissue and Organ Regeneration in Adults 2001; Springer: New York, p. 383.
25. Lo CM, Wang HB, Dembo M,Wang YL. Cell movement is guided by the rigidity of the substrate. Biophysical Journal 2000;79 (1): p 144-152.
26. Engler AJ, Sen S, Sweeney HL,Discher DE. Matrix elasticity directs stem cell lineage specification. Cell 2006;126 (4): p 677-689.
27. Flanagan LA, Ju YE, Marg B, Osterfield M,Janmey PA. Neurite branching on deformable substrates. Neuroreport 2002;13 (18): p 2411-2415.
28. Engler AJ, Griffin MA, Sen S, Bonnetnann CG, Sweeney HL,Discher DE. Myotubes differentiate optimally on substrates with tissue-like stiffness: pathological implications for soft or stiff microenvironments. Journal of Cell Biology 2004;166 (6): p 877-887.
29. Garcia AJ,Reyes CD. Bio-adhesive surfaces to promote osteoblast differentiation and bone formation. Journal of Dental Research 2005;84 (5): p 407-413.
30. Yarlagadda P, Chandrasekharan M,Shyan JYM. Recent advances and current developments in tissue scaffolding. Bio-Medical Materials and Engineering 2005;15 (3): p 159-177.
31. Harley BAC,Gibson LJ. In vivo and in vitro applications of collagen-GAG scaffolds. Chemical Engineering Journal 2008;137 (1): p 102-121.

32. Rowley JA, Madlambayan G,Mooney DJ. Alginate hydrogels as synthetic extracellular matrix materials. Biomaterials 1999;20 (1): p 45-53.
33. Thomas V, Dean DR, Jose MV, Mathew B, Chowdhury S,Vohra YK. Nanostructured biocomposite scaffolds based on collagen coelectrospun with nanohydroxyapatite. Biomacromolecules 2007;8 (2): p 631-637.
34. Kim SS, *et al.* Survival and function of hepatocytes on a novel three-dimensional synthetic biodegradable polymer scaffold with an intrinsic network of channels. Annals of Surgery 1998;228 (1): p 8-13.
35. Zeltinger J, Sherwood JK, Graham DA, Mueller R,Griffith LG. Effect of pore size and void fraction on cellular adhesion, proliferation, and matrix deposition. Tissue Engineering 2001;7 (5): p 557-572.
36. Stock UA,Vacanti JP. Tissue engineering: Current state and prospects. Annual Review of Medicine 2001;52: p 443-451.
37. Jones JR,Hench LL. Regeneration of trabecular bone using porous ceramics. Current Opinion in Solid State & Materials Science 2003;7 (4-5): p 301-307.
38. Laurencin CT, Attawia MA, Elgendy HE,Herbert KM. Tissue engineered bone-regeneration using degradable polymers: The formation of mineralized matrices. Bone 1996;19 (1): p S93-S99.
39. Thomson RC, Yaszemski MJ, Powers JM,Mikos AG. Hydroxyapatite fiber reinforced poly(alpha-hydroxy ester) foams for bone regeneration. Biomaterials 1998;19 (21): p 1935-1943.
40. Navarro M, Ginebra MP, Planell JA, Zeppetelli S,Ambrosio L. Development and cell response of a new biodegradable composite scaffold for guided bone regeneration. Journal of Materials Science-Materials in Medicine 2004;15 (4): p 419-422.
41. Gross KA,Rodriguez-Lorenzo LM. Biodegradable composite scaffolds with an interconnected spherical network for bone tissue engineering. Biomaterials 2004;25 (20): p 4955-4962.
42. Pal K,Pal S. Development of porous hydroxyapatite scaffolds. Materials and Manufacturing Processes 2006;21 (3): p 325-328.
43. Jung Y, Kim SS, Kim YH, Kim SH, Kim BS, Kim S,Choi CY. A poly(lactic acid)/calcium metaphosphate composite for bone tissue engineering. Biomaterials 2005;26 (32): p 6314-6322.
44. Ma PX, Zhang RY, Xiao GZ,Franceschi R. Engineering new bone tissue in vitro on highly porous poly(alpha-hydroxyl acids)/hydroxyapatite composite scaffolds. Journal of Biomedical Materials Research 2001;54 (2): p 284-293.
45. Zhang RY,Ma PX. Poly(alpha-hydroxyl acids) hydroxyapatite porous composites for bone-tissue engineering. I. Preparation and morphology. Journal of Biomedical Materials Research 1999;44 (4): p 446-455.
46. Xiong Z, Yan YN, Wang SG, Zhang RJ,Zhang C. Fabrication of porous scaffolds for bone tissue engineering via low-temperature deposition. Scripta Materialia 2002;46 (11): p 771-776.
47. Zhou YF, Hutmacher DW, Varawan SL,Lim TM. In vitro bone engineering based on polycaprolactone and polycaprolactone-tricalcium phosphate composites. Polymer International 2007;56 (3): p 333-342.

48. Zou C, *et al.* Preparation and characterization of porous beta-tricalcium phosphate collagen composites with an integrated structure. Biomaterials 2005;26 (26): p 5276-5284.
49. Tampieri A, Celotti G, Landi E, Sandri M, Roveri N,Falini G. Biologically inspired synthesis of bone-like composite: Self-assembled collagen fibers/hydroxyapatite nanocrystals. Journal of Biomedical Materials Research Part A 2003;67A (2): p 618-625.
50. Rucker M, *et al.* Angiogenic and inflammatory response to biodegradable scaffolds in dorsal skinfold chambers of mice. Biomaterials 2006;27 (29): p 5027-5038.
51. Yin YJ, Ye F, Cui JF, Zhang FJ, Li XL,Yao KD. Preparation and characterization of macroporous chitosan-gelatin beta-tricalcium phosphate composite scaffolds for bone tissue engineering. Journal of Biomedical Materials Research Part A 2003;67A (3): p 844-855.
52. Zhao F, *et al.* Preparation and histological evaluation of biomimetic three-dimensional hydroxyapatite/chitosan-gelatin network composite scaffolds. Biomaterials 2002;23 (15): p 3227-3234.
53. Kim HW, Kim HE,Salih V. Stimulation of osteoblast responses to biomimetic nanocomposites of gelatin-hydroxyapatite for tissue engineering scaffolds. Biomaterials 2005;26 (25): p 5221-5230.
54. Zhang SM, Cui FZ, Liao SS, Zhu Y,Han L. Synthesis and biocompatibility of porous nanohydroxyapatite/collagen/alginate composite. Journal of Materials Science-Materials in Medicine 2003;14 (7): p 641-645.
55. Yunoki S, *et al.* Control of pore structure and mechanical property in hydroxyapatite/collagen composite using unidirectional ice growth. Materials Letters 2006;60 (8): p 999-1002.
56. Kikuchi M, Itoh S, Ichinose S, Shinomiya K,Tanaka J. Self-organization mechanism in a bone-like hydroxyapatite/collagen nanocomposite synthesized in vitro and its biological reaction in vivo. Biomaterials 2001;22 (13): p 1705-1711.
57. Yokoyama A, Gelinsky M, Kawasaki T, Kohgo T, Konig U, Pompe W,Watari F. Biomimetic porous scaffolds with high elasticity made from mineralized collagen - An animal study. Journal of Biomedical Materials Research Part B-Applied Biomaterials 2005;75B (2): p 464-472.
58. Liao S, Ngiam M, Chan CK,Ramakrishna S. Fabrication of nano-hydroxyapatite/collagen/osteonectin composites for bone graft applications. Biomedical Materials 2009;4 (2): p
59. Chang MC, Ko CC,Douglas WH. Preparation of hydroxyapatite-gelatin nanocomposite. Biomaterials 2003;24 (17): p 2853-2862.
60. Pan SX, Li Y, Feng HL, Bai W,Gu YY. In vitro aging of mineralized collagen-based composite as guided tissue regeneration membrane. Materials Science & Engineering C-Biomimetic and Supramolecular Systems 2006;26 (4): p 724-729.
61. Yannas IV,Burke JF. Design of an Artificial Skin .1. Basic Design Principles. Journal of Biomedical Materials Research 1980;14 (1): p 65-81.
62. Yannas IV. Synthesis of tissues and organs. Chembiochem 2004;5 (1): p 26-39.

63. Yannas IV. Similarities and differences between induced organ regeneration in adults and early foetal regeneration. Journal of the Royal Society Interface 2005;2 (5): p 403-417.
64. Harley BAC, Kim HD, Zaman MH, Yannas IV, Lauffenburger DA,Gibson LJ. Microarchitecture of three-dimensional scaffolds influences cell migration behavior via junction interactions. Biophysical Journal 2008;95 (8): p 4013-4024.
65. Harley BA, Freyman TM, Wong MQ,Gibsony LJ. A new technique for calculating individual dermal fibroblast contractile forces generated within collagen-GAG scaffolds. Biophysical Journal 2007;93 (8): p 2911-2922.
66. O'Brien FJ, Harley BA, Yannas IV,Gibson LJ. The effect of pore size on cell adhesion in collagen-GAG scaffolds. Biomaterials 2005;26 (4): p 433-441.
67. Yannas IV. Biologically-Active Analogs of the Extracellular-Matrix - Artificial Skin and Nerves. Angewandte Chemie-International Edition in English 1990;29 (1): p 20-35.
68. O'Brien FJ, Harley BA, Yannas IV,Gibson L. Influence of freezing rate on pore structure in freeze-dried collagen-GAG scaffolds. Biomaterials 2004;25 (6): p 1077-1086.
69. Lynn AK. Design and development of an osteochondral scaffold. PhD Thesis; Department of Materials Science and Metallurgy; University of Cambridge 2005: p. 165.
70. Lynn AK,Bonfield W. A Novel Method for the Simultaneous, Titrant-Free Control of pH and Calcium Phosphate Mass Yield. Acc. Chem. Res. 2005;38 (3): p 202-207.
71. Lynn AK. A Novel Design Approach for the Production of Calcium Phosphate-Collagen Biocomposites. Key Engineering Materials 2004;254-256: p 593-596.
72. Lynn AK, Cameron RE, Best SM, Brooks RA, Rushton N,Bonfield W. Phase mapping: A novel design approach for the production of calcium phosphate-collagen biocomposites *in Bioceramics 16*. Key Engineering Materials 2004;254-2: p. 593-596.
73. Lynn AK, *et al.* Composition-controlled nanocomposites of apatite and collagen incorporating silicon as an osseopromotive agent. Journal of Biomedical Materials Research Part A 2005;74A (3): p 447-453.
74. Harley BA, Lynn AK, Wissner-Gross Z, Bonfield W, Yannas IV,Gibson LJ. Design of a Multiphase Osteochondral Scaffold II: Fabrication of a Mineralized Collagen-GAG Scaffold. Journal of Biomedical Materials Research (Part A) 2009;In press: p
75. Lynn AK, Best SM, Cameron RE, Harley BA, Yannas IV, Gibson LJ,Bonfield W. Design of a Multiphase Osteochondral Scaffold I: Control of Chemical Composition. Journal of Biomedical Materials Research (Part A) 2009;In Press: p
76. Harley BA, Lynn AK, Wissner-Gross Z, Bonfield W, Yannas IV,Gibson LJ. Design of a MultiphaseOsteochondral Scaffold III: Fabrication of Layered Scaffolds with Continuous Interfaces. Journal of Biomedical Materials Research (Part A) 2009;In press: p
77. Steadman JR, Rodkey WG,Rodrigo JJ. Microfracture: Surgical technique and rehabilitation to treat chondral defects. Clinical Orthopaedics and Related Research 2001; (391): p S362-S369.

78. Knutsen G, *et al.* Autologous chondrocyte implantation compared with microfracture in the knee - A randomized trial. Journal of Bone and Joint Surgery-American Volume 2004;86A (3): p 455-464.
79. Feczko P, *et al.* Experimental results of donor site filling for autologous osteochondral mosaicplasty. Arthroscopy-the Journal of Arthroscopic and Related Surgery 2003;19 (7): p 755-761.
80. Huntley JS, Bush PG, McBirnie JM, Simpson AH,Hall AC. Chondrocyte death associated with human femoral osteochondral harvest as performed for mosaicplasty. Journal of Bone and Joint Surgery-American Volume 2005;87A (2): p 351-360.
81. Whiteside RA, Jakob RP, Wyss UP,Mainil-Varlet P. Impact loading of articular cartilage during transplantation of osteochondral autograft. Journal of Bone and Joint Surgery-British Volume 2005;87B (9): p 1285-1291.
82. Lane JG, *et al.* A morphologic, biochemical, and biomechanical assessment of short-term effects of osteochondral autograft plug transfer in an animal model. Arthroscopy-the Journal of Arthroscopic and Related Surgery 2001;17 (8): p 856-863.
83. Harman BD, Weeden SH, Lichota DK,Brindley GW. Osteochondral autograft transplantation in the porcine knee. American Journal of Sports Medicine 2006;34 (6): p 913-918.
84. Kim SS, Ahn KM, Park MS, Lee JH, Choi CY,Kim BS. A poly(lactide-co-glycolide)/hydroxyapatite composite scaffold with enhanced osteoconductivity. Journal of Biomedical Materials Research Part A 2007;80A (1): p 206-215.
85. Kim SS, Park MS, Jeon O, Choi CY,Kim BS. Poly(lactide-co-glycolide)/hydroxyapatite composite scaffolds for bone tissue engineering. Biomaterials 2006;27 (8): p 1399-1409.
86. Kothapalli CR, Shaw MT,Wei M. Biodegradable HA-PLA 3-D porous scaffolds: Effect of nano-sized filler content on scaffold properties. Acta Biomaterialia 2005;1 (6): p 653-662.
87. Park YS, Kim KN, Kim KM, Choi SH, Kim CK, Legeros RZ,Lee YK. Feasibility of three-dimensional macroporous scaffold using calcium phosphate glass and polyurethane sponge. Journal of Materials Science 2006;41 (13): p 4357-4364.
88. Wahl DA, Sachlos E, Liu CZ,Czernuszka JT. Controlling the processing of collagen-hydroxyapatite scaffolds for bone tissue engineering. Journal of Materials Science-Materials in Medicine 2007;18 (2): p 201-209.
89. Kim HW, Knowles JC,Kim HE. Hydroxyapatite and gelatin composite foams processed via novel freeze-drying and crosslinking for use as temporary hard tissue scaffolds. Journal of Biomedical Materials Research Part A 2005;72A (2): p 136-145.
90. Zhang Y,Zhang MQ. Synthesis and characterization of macroporous chitosan/calcium phosphate composite scaffolds for tissue engineering. Journal of Biomedical Materials Research 2001;55 (3): p 304-312.
91. Hosseinkhani H, Hosseinkhani M, Tian F, Kobayashi H,Tabata Y. Ectopic bone formation in collagen sponge self-assembled peptide-amphiphile nanofibers hybrid scaffold in a perfusion culture bioreactor. Biomaterials 2006;27 (29): p 5089-5098.

92. Xu HHK, Takagi S, Quinn JB,Chow LC. Fast-setting calcium phosphate scaffolds with tailored macropore formation rates for bone regeneration. Journal of Biomedical Materials Research Part A 2004;68A (4): p 725-734.
93. Woodard JR, *et al.* The mechanical properties and osteoconductivity of hydroxyapatite bone scaffolds with multi-scale porosity. Biomaterials 2007;28 (1): p 45-54.
94. Currey JD. Bones: Structure and Mechanics 2002; Princeton University Press, p. 456.
95. Gibson LJ,Ashby MF. Cellular Solids: Structure and Properties. 2nd ed 1997; Cambridge University Press, p. 510.
96. Martin RB, Burr DB,Sharkey NA. Skeletal Tissue Mechanics 1998; Springer, p. 392.
97. Lichtwark GA,Wilson AM. In vivo mechanical properties of the human Achilles tendon during one-legged hopping. Journal of Experimental Biology 2005;208 (24): p 4715-4725.
98. Stabile KJ, Pfaeffle J, Weiss JA, Fischer K,Tomaino MM. Bi-directional mechanical properties of the human forearm interosseous ligament. Journal of Orthopaedic Research 2004;22 (3): p 607-612.
99. Spilker MH, Asano K, Yannas IV,Spector M. Contraction of Collagen-Glycosaminoglycan Matrices by Peripheral Nerve Cells In Vitro. Biomaterials 2001;22: p 1085-1093.
100. Brekke JH,Toth JM. Principles of tissue engineering applied to programmable osteogenesis. Journal of Biomedical Materials Research 1998;43 (4): p 380-398.
101. Gibson LJ. Biomechanics of cellular solids. Journal of Biomechanics 2005;38 (3): p 377-399.
102. Harley BA,Flemings MC. Coarsening-Mediated Solidification is Responsible for Defining the Pore Microstructure of Collagen-Glycosaminoglycan Scaffolds: Experimental and Thermal Modeling Results. Acta Materialia 2007;In Revision: p
103. Kanungo BP, Silva ECCM, Van Vliet K,Gibson LJ. Characterization of mineralized collagen–glycosaminoglycan scaffolds for bone regeneration. Acta Biomaterialia 2008;4: p 490-503.
104. Kanungo BP,Gibson LJ. Density-Property Relationships in Collagen-Glycosaminoglycan Scaffolds. Acta Biomaterialia 2009;Submitted: p
105. Ashman RB, Cowin SC, Vanbuskirk WC,Rice JC. A Continuous Wave Technique for the Measurement of the Elastic Properties of Cortical Bone. Journal of Biomechanics 1984;17 (5): p 349-361.
106. Kellomaki M, Niiranen H, Puumanen K, Ashammakhi N, Waris T,Tormala P. Bioabsorbable scaffolds for guided bone regeneration and generation. Biomaterials 2000;21 (24): p 2495-2505.
107. Yang CR, Wang YJ, Chen XF,Zhao NR. Biomimetic fabrication of BCP/COL/HCA scaffolds for bone tissue engineering. Materials Letters 2005;59 (28): p 3635-3640.
108. Lu HH, El-Amin SF, Scott KD,Laurencin CT. Three-dimensional, bioactive, biodegradable, polymer-bioactive glass composite scaffolds with improved mechanical properties support collagen synthesis and mineralization of human

osteoblast-like cells in vitro. Journal of Biomedical Materials Research Part A 2003;64A (3): p 465-474.
109. Ott CS. Development of bi-layer mineralized bone and cartilage regeneration template. M.Eng. Thesis; Department of Materials Science and Engineering; Massachusetts Institute of Technology 2005: p. 94.
110. Lynn AK, Brooks RA, Bonfield W,Rushton N. Repair of defects in articular joints: Prospects for material-based solutions in tissue engineering. J Bone Joint Surg Br 2004;86-B (8): p 1093-1099.
111. Dagalakis N, Flink J, Stasikelis P, Burke JF,Yannas IV. Design of an Artificial Skin .3. Control of Pore Structure. Journal of Biomedical Materials Research 1980;14 (4): p 511-528.
112. Tadic D, Beckmann F, Schwarz K,Epple M. A novel method to produce hydroxyapatite objects with interconnecting porosity that avoids sintering. Biomaterials 2004;25 (16): p 3335-3340.
113. Salgado AJ, Figueiredo JE, Coutinho OP,Reis RL. Biological response to pre-mineralized starch based scaffolds for bone tissue engineering. Journal of Materials Science-Materials in Medicine 2005;16 (3): p 267-275.
114. Wang FM, Qiu K, Hu T, Wan CX, Zhou XD,Gutmann JL. Biodegradable porous calcium polyphosphate scaffolds for the three-dimensional culture of dental pulp cells. International Endodontic Journal 2006;39 (6): p 477-483.
115. Munar ML, Udoh K, Ishikawa K, Matsuya S,Nakagawa M. Effects of sintering temperature over 1,300 degrees C on the physical and compositional properties of porous hydroxyapatite foam. Dental Materials Journal 2006;25 (1): p 51-58.
116. Yannas IV,Tobolsky AV. Cross-linking of gelatine by dehydration. Nature 1967;215 (5100): p
117. Beevers CA. The crystal structure of dicalcium phosphate dihydrate, $CaHPO_4$. $2H_2O$. Acta Crystallogr 1957;11: p 273-277.
118. MacLeenan G,Beevers CA. The crystal structure of dicalcium phosphate, CaHPO4. Acta Crystallogr 1955;8: p 579-583.
119. Klug HP,Alexander LE. X-ray diffraction procedures: for polycrystalline and amorphous materials. 2nd ed 1974; John Wiley & Sons;, p. 966.
120. Jenkins R,Snyder RL. Introduction to X-ray powder diffractometry 1996403.
121. Silva E,Van Vliet KJ. Robust approach to maximize the range and accuracy of force application in atomic force microscopes with nonlinear position-sensitive detectors. Nanotechnology 2006;17 (21): p 5525-5530.
122. Silva E, Tong LM, Yip S,Van Vliet KJ. Size effects on the stiffness of silica nanowires. Small 2006;2 (2): p 239-243.
123. Chiang CY, Mello CM, Gu JJ, Silva E, Van Vliet KJ,Belcher AM. Weaving genetically engineered functionality into mechanically robust virus fibers. Advanced Materials 2007;19 (6): p 826-832.
124. Oliver WC,Pharr GM. Measurement of hardness and elastic modulus by instrumented indentation: Advances in understanding and refinements to methodology. Journal of Materials Research 2004;19 (1): p 3-20.
125. VanLandingham MR. Review of instrumented indentation. Journal of Research of the National Institute of Standards and Technology 2003;108 (4): p 249-265.

126. Schuh CA. Nanoindentation studies of materials. Materials Today 2006;9 (5): p 32-40.
127. Ho ST,Hutmacher DW. A comparison of micro CT with other techniques used in the characterization of scaffolds. Biomaterials 2006;27 (8): p 1362-1376.
128. Babis GC,Soucacos PN. Bone scaffolds: The role of mechanical stability and instrumentation. Injury-International Journal of the Care of the Injured 2005;36: p S38-S44.
129. Karageorgiou V,Kaplan D. Porosity of 3D biornaterial scaffolds and osteogenesis. Biomaterials 2005;26 (27): p 5474-5491.
130. Reis RL, Cunha AM, Fernandes MH,Correia RN. Treatments to induce the nucleation and growth of apatite-like layers on polymeric surfaces and foams. Journal of Materials Science-Materials in Medicine 1997;8 (12): p 897-905.
131. Tanahashi M, Yao T, Kokubo T, Minoda M, Miyamoto T, Nakamura T,Yamamuro T. Apatite Coating on Organic Polymers by a Biomimetic Process. Journal of the American Ceramic Society 1994;77 (11): p 2805-2808.
132. Oliveira AL, Malafaya PB,Reis RL. Sodium silicate gel as a precursor for the in vitro nucleation and growth of a bone-like apatite coating in compact and porous polymeric structures. Biomaterials 2003;24 (15): p 2575-2584.
133. Brown WE, Smith JP, Lehr JR,Frazier AW. Octacalcium phosphate and hydroxyapatite: crystallographic and chemical relations between octacalcium phosphate and hydroxyapatite. Nature 1962;196 (1048-1055): p
134. Heughebaert JC, Lebugle A, Vu F,Phan-Tan-Luu R. Central composite design and optimization by multiresponse analysis of octacalcium phosphate synthesis. Analusis 2000;28 (7): p 571-574.
135. Raatikainen P, Silvennoinen R, Ketolainen J, Ketolainen P,Paronen P. Evaluation of pharmaceutical beam bending tests using double-exposure holographic interferometry. European Journal of Pharmaceutics and Biopharmaceutics 1997;44 (3): p 261-267.
136. Vajjhala S, Kraynik AM,Gibson LJ. A cellular solid model for modulus reduction due to resorption of trabeculae in bone. Journal of Biomechanical Engineering-Transactions of the ASME 2000;122 (5): p 511-515.
137. Guo XE,Kim CH. Effects of age-related bone loss: a 3D microstructural simulation. Proceedings of ASME Bioengineering conference 1999;42: p 327-328.
138. Silva MJ,Gibson LJ. The effects of non-periodic microstructure and defects on the compressive strength of two-dimensional cellular solids. International Journal of Mechanical Sciences 1997;39 (5): p 549-563.
139. Silva MJ, Hayes WC,Gibson LJ. The Effects of Nonperiodic Microstructure on the Elastic Properties of 2-Dimensional Cellular Solids. International Journal of Mechanical Sciences 1995;37 (11): p 1161-1177.
140. Yannas IV, Burke JF, Warpehoski M, Stasikelis P, Skrabut EM, Orgill D,Giard DJ. Prompt, Long-Term Functional Replacement of Skin. Transactions American Society for Artificial Internal Organs 1981;27: p 19-23.
141. Yannas IV. Facts and theories of induced organ regeneration *in Regenerative Medicine I: Theories, Models and Methods*. Advances in Biochemical Engineering / Biotechnology 2005;93: p. 1-38.

142. Madaghiele M, Sannino A, Yannas IV,Spector M. Collagen-based matrices with axially oriented pores. Journal of Biomedical Materials Research Part A 2008;85A (3): p 757-767.
143. Harley BA, Spilker MH, Wu JW, Asano K, Hsu HP, Spector M,Yannas IV. Optimal degradation rate for collagen chambers used for regeneration of peripheral nerves over long gaps. Cells Tissues Organs 2004;176 (1-3): p 153-165.
144. Chamberlain LJ, Yannas IV, Hsu HP, Strichartz GR,Spector M. Near-terminus axonal structure and function following rat sciatic nerve regeneration through a collagen-GAG matrix in a ten-millimeter gap. Journal of Neuroscience Research 2000;60 (5): p 666-677.
145. Chamberlain LJ, Yannas IV, Hsu HP, Strichartz G,Spector M. Collagen-GAG substrate enhances the quality of nerve regeneration through collagen tubes up to level of autograft. Experimental Neurology 1998;154 (2): p 315-329.
146. Chamberlain LJ, Yannas IV, Hsu HP,Spector M. Connective tissue response to tubular implants for peripheral nerve regeneration: The role of myofibroblasts. Journal of Comparative Neurology 2000;417 (4): p 415-430.
147. Chamberlain LJ, Yannas IV, Arrizabalaga A, Hsu HP, Norregaard TV,Spector M. Early peripheral nerve healing in collagen and silicone tube implants: Myofibroblasts and the cellular response. Biomaterials 1998;19 (15): p 1393-1403.
148. Evans FG,Lebow M. Regional differences in some of the physical properties of the human femur. Journal of applied physiology 1951;3: p 563-572.
149. Evans FG. Facotrs affecting the mechanical properties of bone. Bulletin of the new york academy of medicine 1973;49 (9): p 751-764.
150. Dempster WT,Liddicoat R. Compact bone as a non-isotropic material. American journal of anatomy 1952;91 (3): p 331-362.
151. Hollister SJ, Maddox RD,Taboas JM. Optimal design and fabrication of scaffolds to mimic tissue properties and satisfy biological constraints. Biomaterials 2002;23 (20): p 4095-4103.
152. Kanungo BP,Gibson LJ. Density-Property Relationships in Mineralized Collagen-Glycosaminoglycan Scaffolds for Bone Regeneration. Acta Biomaterialia 2009;5: p 1006-1018.
153. Danielsson PE. Euclidean Distance Mapping. Computer Graphics and Image Processing 1980;14 (3): p 227-248.
154. Kikuchi M, *et al.* Porous body preparation of hydroxyapatite/collagen nanocomposites for bone tissue regeneration *in Bioceramics 16*. Key Engineering Materials 2004;254-2: p. 561-564.
155. Chang MC, Ikoma T, Kikuchi M,Tanaka J. Preparation of a porous hydroxyapatite/collagen nanocomposite using glutaraldehyde as a crosslinkage agent. Journal of Materials Science Letters 2001;20 (13): p 1199-1201.
156. Turner CH, Rho J, Takano Y, Tsui TY,Pharr GM. The elastic properties of trabecular and cortical bone tissues are similar: results from two microscopic measurement techniques. Journal of Biomechanics 1999;32 (4): p 437-441.

157. Roy ME, Rho JY, Tsui TY, Evans ND,Pharr GM. Mechanical and morphological variation of the human lumbar vertebral cortical and trabecular bone. Journal of Biomedical Materials Research 1999;44 (2): p 191-197.
158. Rho JY, Tsui TY,Pharr GM. Elastic properties of human cortical and trabecular lamellar bone measured by nanoindentation. Biomaterials 1997;18 (20): p 1325-1330.
159. Rho JY, Roy ME, Tsui TY,Pharr GM. Elastic properties of microstructural components of human bone tissue as measured by nanoindentation. Journal of Biomedical Materials Research 1999;45 (1): p 48-54.
160. Chevalier Y, Pahr D, Allmer H, Charlebois M,Zysset P. Validation of a voxel-based FE method for prediction of the uniaxial apparent modulus of human trabecular bone using macroscopic mechanical tests and nanoindentation. Journal of Biomechanics 2007;40 (15): p 3333-3340.
161. Guo XE,Gibson LJ. Behavior of intact and damaged honeycombs: a finite element study. International Journal of Mechanical Sciences 1999;41 (1): p 85-105.
162. Turner RT, Backup P, Sherman PJ, Hill E, Evans GL,Spelsberg TC. Mechanism of Action of Estrogen on Intramembranous Bone-Formation - Regulation of Osteoblast Differentiation and Activity. Endocrinology 1992;131 (2): p 883-889.
163. Tierney CM, Haugh MG, Liedl J, Mulcahy F, Hayes B,O'Brien FJ. The effects of collagen concentration and crosslink density on the biological, structural and mechanical properties of collagen-GAG scaffolds for bone tissue engineering. Journal of the mechanical behavior of the biomedical materials 2008;In press: p
164. Tierney CM, Jaasma MJ,O'Brien FJ. Osteoblast activity is affected by collagen and GAG concentrations and crosslinking temperature. Tissue Engineering 2007;13 (7): p 316.
165. Peyton SR,Putnam AJ. Extracellular matrix rigidity governs smooth muscle cell motility in a biphasic fashion. Journal of Cellular Physiology 2005;204 (1): p 198-209.
166. Grinnell F, Ho CH, Lin YC,Skuta G. Differences in the regulation of fibroblast contraction of floating versus stressed collagen matrices. Journal of Biological Chemistry 1999;274 (2): p 918-923.
167. Freyman TM, Yannas IV, Yokoo R,Gibson LJ. Fibroblast contraction of a collagen-GAG matrix. Biomaterials 2001;22 (21): p 2883-2891.
168. Yeung T, *et al.* Effects of substrate stiffness on cell morphology, cytoskeletal structure, and adhesion. Cell Motility and the Cytoskeleton 2005;60 (1): p 24-34.
169. Menard C, Mitchell S,Spector M. Contractile behavior of smooth muscle actin-containing osteoblasts in collagen-GAG matrices in vitro: implant-related cell contractions. Biomaterials 2000;21 (18): p 1867-1877.
170. Young RG, Butler DL, Weber W, Caplan AI, Gordon SL,Fink DJ. Use of mesenchymal stem cells in a collagen matrix for Achilles tendon repair. Journal of Orthopaedic Research 1998;16 (4): p 406-413.
171. Bellincampi LD, Closkey RF, Prasad R, Zawadsky JP,Dunn MG. Viability of fibroblast-seeded ligament analogs after autogenous implantation. Journal of Orthopaedic Research 1998;16 (4): p 414-420.

172. Dunn MG, Liesch JB, Tiku ML,Zawadsky JP. Development of Fibroblast-Seeded Ligament Analogs for Acl Reconstruction. Journal of Biomedical Materials Research 1995;29 (11): p 1363-1371.
173. Dunn MG, Maxian SH,Zawadsky JP. Intraosseous Incorporation of Composite Collagen Prostheses Designed for Ligament Reconstruction. Journal of Orthopaedic Research 1994;12 (1): p 128-137.
174. Dunn MG, Tria AJ, Kato YP, Bechler JR, Ochner RS, Zawadsky JP,Silver FH. Anterior Cruciate Ligament Reconstruction Using a Composite Collagenous Prosthesis - a Biomechanical and Histologic-Study in Rabbits. American Journal of Sports Medicine 1992;20 (5): p 507-575.
175. Jackson DW, Simon TM, Lowery W,Gendler E. Biologic remodeling after anterior cruciate ligament reconstruction using a collagen matrix derived from demineralized bone - An experimental study in the goat model. American Journal of Sports Medicine 1996;24 (4): p 405-414.
176. Kato YP, Dunn MG, Zawadsky JP, Tria AJ,Silver FH. Regeneration of Achilles-Tendon with a Collagen Tendon Prosthesis - Results of a One-Year Implantation Study. Journal of Bone and Joint Surgery-American Volume 1991;73A (4): p 561-574.
177. Woo SLY, Debski RE, Zeminski J, Abramowitch SD, Saw SSC,Fenwick JA. Injury and repair of ligaments and tendons. Annual Review of Biomedical Engineering 2000;2: p 83-118.
178. Chen JM, Xu JK, Wang AL,Zheng MH. Scaffolds for tendon and ligament repair: review of the efficacy of commercial products. Expert Review of Medical Devices 2009;6 (1): p 61-73.
179. Brodsky JW, Baum BS, Polio FE,Shabat S. Surgical reconstruction of posterior tibial tendon tear in adolescents: Report of two cases and review of the literature. Foot & Ankle International 2005;26 (3): p 218-223.
180. Ge ZG, Yang F, Goh JCH, Ramakrishna S,Lee EH. Biomaterials and scaffolds for ligament tissue engineering. Journal of Biomedical Materials Research Part A 2006;77A (3): p 639-652.
181. Laurencin CT, Ambrosio AMA, Borden MD,Cooper JA. Tissue engineering: Orthopedic applications. Annual Review of Biomedical Engineering 1999;1: p 19-46.
182. Koski JA, Ibarra C,Rodeo SA. Tissue-engineered ligament - Cells, matrix, and growth factors. Orthopedic Clinics of North America 2000;31 (3): p 437-+.
183. Viinikainen A, Goransson H,Ryhanen J. Primary Flexor Tendon Repair Techniques. Scandinavian Journal of Surgery 2008;97 (4): p 333-340.
184. Berlet GC, Johnson JA, Milne AD, Patterson SD,King GJW. Distal biceps brachii tendon repair - An in vitro biomechanical study of tendon reattachment. American Journal of Sports Medicine 1998;26 (3): p 428-432.
185. Birch HL, Wilson AM,Goodship AE. Physical activity: does long-term, high-intensity exercise in horses result in tendon degeneration? Journal of Applied Physiology 2008;105 (6): p 1927-1933.
186. Yamaji T, Levine RE, Woo SLY, Niyibizi C, Kavalkovich KW,WeaverGreen CM. Medial collateral ligament healing one year after a concurrent medial

collateral ligament and anterior cruciate ligament injury: An interdisciplinary study in rabbits. Journal of Orthopaedic Research 1996;14 (2): p 223-227.
187. Torres DS, Freyman TM, Yannas IV,Spector M. Tendon cell contraction of collagen-GAG matrices in vitro: effect of cross-linking. Biomaterials 2000;21 (15): p 1607-1619.
188. Freyman TM, Yannas IV, Pek YS, Yokoo R,Gibson LJ. Micromechanics of fibroblast contraction of a collagen-GAG matrix. Experimental Cell Research 2001;269 (1): p 140-153.
189. Pieper JS, Oosterhof A, Dijkstra PJ, Veerkamp JH,van Kuppevelt TH. Preparation and characterization of porous crosslinked collagenous matrices containing bioavailable chondroitin sulphate. Biomaterials 1999;20 (9): p 847-858.
190. Lambe TW,Whitman. Soil mechanics 1979; John Wiley & Sons, p. 553.
191. Vickers SM, Squitieri LS,Spector M. Effects of cross-linking type II collagen-GAG scaffolds on chondrogenesis in vitro: Dynamic pore reduction promotes cartilage formation. Tissue Engineering 2006;12 (5): p 1345-1355.
192. Lee CR, Grodzinsky AJ,Spector M. The effects of cross-linking of collagen-glycosaminoglycan scaffolds on compressive stiffness, chondrocyte-mediated contraction, proliferation and biosynthesis. Biomaterials 2001;22 (23): p 3145-3154.
193. Damink L, Dijkstra PJ, vanLuyn MJA, vanWachem PB, Nieuwenhuis P,Feijen J. Cross-linking of dermal sheep collagen using a water-soluble carbodiimide. Biomaterials 1996;17 (8): p 765-773.